



SOURCE CHARACTERIZATION MODEL (SCM)

A PREDICTIVE CAPABILITY FOR THE SOURCE TERMS OF RESIDUAL ENERGETIC MATERIALS FROM BURNING AND/OR DETONATION ACTIVITIES

SERDP PROJECT CP-1159 FINAL REPORT

Prepared for:

Robert Holst, Ph.D.
SERDP/ESTCP Program Manager Compliance/Conservation

Prepared by:

Robert C. Brown, Charles E. Kolb, John A. Conant, John Zhang^{*}, and David M. Dussault
Center for Aero Thermodynamics
Aerodyne Research, Inc.
Billerica, MA 01821-3976

and

Tamera L. Rush, Brooke E. Conway, and James W. Morris
U.S. Army Environmental Center
Aberdeen Proving Ground, MD 21010-5401

And

Joe Touma
Environmental Protection Agency
Research Triangle, NC

April 2004

^{*} Currently at Delta Search, Cambridge, MA.

Report Documentation Page				Form Approved OMB No. 0704-0188	
Public reporting burden for the collection of information is estimated to average 1 hour per response, including the time for reviewing instructions, searching existing data sources, gathering and maintaining the data needed, and completing and reviewing the collection of information. Send comments regarding this burden estimate or any other aspect of this collection of information, including suggestions for reducing this burden, to Washington Headquarters Services, Directorate for Information Operations and Reports, 1215 Jefferson Davis Highway, Suite 1204, Arlington VA 22202-4302. Respondents should be aware that notwithstanding any other provision of law, no person shall be subject to a penalty for failing to comply with a collection of information if it does not display a currently valid OMB control number.					
1. REPORT DATE APR 2004		2. REPORT TYPE Final		3. DATES COVERED -	
4. TITLE AND SUBTITLE Source Characterization Model (SCM): A Predictive Capability for the Source Terms of Residual Energetic Materials from Burning and/or Detonation Activities				5a. CONTRACT NUMBER	
				5b. GRANT NUMBER	
				5c. PROGRAM ELEMENT NUMBER	
6. AUTHOR(S) 1. Robert C. Brown, Charles E. Kolb, John A. Conant, John Zhang, and David M. Dussault 2. Tamera L. Rush, Brooke E. Conway, and James W. Morris 3. Joe Touma				5d. PROJECT NUMBER CP-1159	
				5e. TASK NUMBER	
				5f. WORK UNIT NUMBER	
7. PERFORMING ORGANIZATION NAME(S) AND ADDRESS(ES) 1. Center for Aero Thermodynamics Aerodyne Research, Inc. Billerica, MA 01821-3976 2. U.S. Army Environmental Center Aberdeen Proving Ground, MD 21010-5401 3. Environmental Protection Agency Research Triangle, NC				8. PERFORMING ORGANIZATION REPORT NUMBER	
9. SPONSORING/MONITORING AGENCY NAME(S) AND ADDRESS(ES) Strategic Environmental Research & Development Program 901 N Stuart Street, Suite 303 Arlington, VA 22203				10. SPONSOR/MONITOR'S ACRONYM(S) SERDP	
				11. SPONSOR/MONITOR'S REPORT NUMBER(S)	
12. DISTRIBUTION/AVAILABILITY STATEMENT Approved for public release, distribution unlimited					
13. SUPPLEMENTARY NOTES The original document contains color images.					
14. ABSTRACT					
15. SUBJECT TERMS					
16. SECURITY CLASSIFICATION OF:			17. LIMITATION OF ABSTRACT UU	18. NUMBER OF PAGES 90	19a. NAME OF RESPONSIBLE PERSON
a. REPORT unclassified	b. ABSTRACT unclassified	c. THIS PAGE unclassified			

EXECUTIVE SUMMARY

This is the final report for the Source Characterization Model (SCM) developed by Aerodyne Research, Inc. (ARI) in collaboration with the U.S. Army Environmental Center (USAEC). It describes work performed under contract DACA72-00-C-0001 from the Strategic Environmental Research and Development Program (SERDP) for the project CP-1159 entitled "A Predictive Capability for the Source Terms of Residual Energetic Materials from Burning and/or Detonation Activities". A portion of this report was previously released as a supplement to the 2002 Annual Report for that SERDP project.

Detonation of energetic materials produces a wide range of air and surface pollutants, including carbon monoxide, nitrogen oxides, volatile organic compounds, acid gases, and particulate matter. These emissions, including undecomposed or partially decomposed energetic materials, may lead to atmospheric pollution or ground water contamination. The speciation and amounts of these emitted pollutants depend on the identity and amount of energetic material detonated, the detonation order, the detonation mode (air burst, surface detonation, buried detonation), and the munitions type (shell, mine, detonation charge, etc.). In order to determine whether U.S. military training or munitions disposal activities produce emissions that threaten air or ground water quality, reliable estimates of emission factors must be available for a representative fraction of the thousands of munitions types in the inventory. A variety of recent detonation experiments, including detonation chamber tests, and open-air field detonations have yielded increasingly rich data sets of measured gaseous and particulate emissions factors from a range of energetic materials deployed as both unconfined charges and standard munitions. These data have been used under CP-1159 to guide the development of a detonation source characterization model (SCM) to be used to predict emissions across munitions classes and detonation modes. The SCM predicts the chemical and physical distribution of detonation products in the initial detonation fireball, calculates the amount, chemical influence, and deposition distribution of dirt entrained into the fireball, and the effects of afterburning as oxygen rich air is entrained into the hot rising plume on both gas phase and particulate emissions, and estimates the amount of shock ablated energetic material that escaped the fireball. SCM predictions have been validated against measured emissions factors for a variety of munitions. The validated SCM can be used to extend emission factor predictions to unmeasured munitions types and to compute input data for traditional atmospheric dispersion/reaction models and soil/water transport/transformation models. The SCM was developed at Aerodyne Research, Inc. utilizing munitions composition and measured detonation products databases developed by collaborators at the U.S. Army Environmental Center.

SCM Model Summary

As documented in this report, the SCM includes the following sub-models for the critical processes governing the post-detonation plume and chemical evolution of detonation emission products.

Detonation Thermochemistry: predicts thermodynamic properties and chemical speciation of the high temperature and pressure Chapman-Jouquet (C-J) detonation state and the adiabat for the rapid isentropic expansion of detonation gas towards atmospheric pressures.

Crater Dynamics: predicts crater size and the mass and particle size distribution for ejected soil partitioning into the buoyant cloud.

Buoyant Puff Rise: predicts the chemical speciation, thermodynamic properties, height, and volume of the buoyant detonation puff when it has equilibrated with the ambient atmosphere.

Buoyant Puff Structure: treats the vortex structure of the detonation puff including the effect on particle deposition.

Particle Deposition: treats particle deposition due to gravitational settling and the impact of particle fall-off on buoyant puff rise.

Meteorology: enables the treatment of buoyant puff rise in a one-dimensional stratified atmosphere.

Chemical Kinetics: treats the afterburning chemistry in the post-detonation plume with air entrainment.

Collectively, the sub-models listed above enable the SCM to support environmental impact assessments at DoD test and training sites in two specific ways:

- SCM predictions for detonation plume properties and chemical speciation are important to near term (to the range fence) air quality issues and provide the necessary inputs to longer time atmospheric dispersion models to assess air quality issues over distances beyond the specific DoD site.
- SCM predictions for particle depositions are important to near term ground/ground water pollution issues and provide necessary inputs to fate and transport models for environmental assessments.

Project Highlights

SERDP has sponsored the development of a computer model that predicts potential air and ground water pollutants produced by exploding munitions and demolition charges. Developed at Aerodyne Research, Inc., the computer model, termed a detonation source characterization model (SCM), draws on new databases compiling munitions compositions and detonation products developed by collaborating scientists at the Army Environmental Center.

The detonation source characterization model (SCM) is composed of a number of coordinated sub-models. These sub-models predict the chemical content of the detonation fireball, compute the mass of fireball entrained soil particles, estimate the amount of shock ablated energetic material that escapes beyond the fireball, model the entrainment of atmospheric oxygen mixed into the fireball and the subsequent afterburning effects on the chemical content of the detonation plume, predict the chemical interactions among both gas phase pollutants and soot and dirt particles in the plume, calculate the deposition pattern of larger plume entrained particles back to the surface, and predict the buoyant rise of the plume gases and entrained fine particles.

The detonation SCM has been validated with pollutant emission factor data obtained for a range of munitions and demolition charges obtained in an on-going series of detonation tests managed by the Army Environmental Center. After validation against a sufficient range of diverse munitions and explosives, the SCM can be used to predict emissions factors for as yet unmeasured types of munitions.

SCM predicted emissions factors can be used as inputs for traditional atmospheric dispersion or soil and ground water transport models that may be used by environmental scientists and engineers to predict the impact of military training, weapons testing, or munitions disposal activities on military facilities and surrounding regions.

Under an additional task, ARI deployed an innovative aerosol mass spectrometer (AMS) instrument to support the SERDP project CP-1197, consisting of field measurements by Battelle, Columbus, OH and managed by USAEC, by measuring the non-refractory chemical composition of fine particles from firing point muzzle exhaust plumes. Muzzle exhaust plumes contained in the Aberdeen Test Center's (ATC) point-of-discharge test chamber were sampled for about 20 minutes after the firing of the each munition. The non-refractory chemical composition of the evolving muzzle exhaust plume fine particles size distribution was characterized during these measurements. A summary of these results and a citation for the task report we presented is given in Appendix A.

TABLE OF CONTENTS

Executive Summary	ii
List of Tables	vi
List of Figures	vii
List of Figures	vii
List of Acronyms	viii
1.0 Introduction	1
1.1 Background	1
1.1.1 Environmental and Public Safety Impact of Munitions Emissions	1
1.1.2 Emissions Characterization Test Programs	1
1.1.3 Energetic Residue from Munition Detonation	1
1.1.4 OB/OD and Detonation Emissions Modeling	1
1.2 Source Characterization Model	2
1.2.1 Features and Capabilities	2
1.3 Report Outline	3
2.0 SCM Model Phenomenology	4
2.1 Model Overview	4
2.1.1 Stage 1: Detonation Energetics and Chemistry	4
2.1.2 Stage 2: Buoyant Puff Rise	5
2.1.3 Stage 3: Atmospheric Dispersion	5
2.2 Computational Processing Flow	6
3.0 SCM Model Description	8
3.1 Detonation Thermochemistry and Emission Factors	8
3.1.1 Phenomenology	8
3.1.2 Chemical Equilibrium	9
3.1.3 Initial Cloud Radius	11
3.2 Crater Dynamics	13
3.2.1 Crater Volume	13
3.2.2 Dust Cloud Mass	17
3.2.3 Dust Cloud Particle Distribution	18
3.3 Puff Fluid Dynamics	22
3.3.1 Analytical Results	22
3.3.2 Governing Equations	25
3.4 Buoyant Puff Flow Structure	28
3.4.1 Vortex Method Modeling	28
3.4.2 Extending Hill's Vortex Modeling	31
3.5 Particle Deposition	34
3.5.1 Deposition	34
3.5.2 Particle Motion in Buoyant Puff	35
3.5.3 Effect of Particle Fall-off on Buoyant Puff Rise	41
3.6 Meteorology	43
3.6.1 Atmospheric Stratification	43
3.6.2 Atmospheric Stability	44
3.6.3 Sensible Heat Flux	45

3.6.4	Friction Velocity and Monin-Obukhov Length	46
3.7	Chemical Kinetics	46
3.7.1	Phenomenology	46
3.7.2	Chemical Kinetic Mechanisms	47
3.7.3	Numerical Model	48
3.7.4	RDX Half-life	48
3.8	Heterogeneous Update Kinetics	50
3.8.1	Overview	50
3.8.2	Soil Particle Uptake Kinetics	50
3.8.3	Soot Uptake Kinetics	52
3.8.4	Summary	53
3.9	Energetic Material Model	53
4.0	<i>Army Range and Munitions Environmental Data (ARMED)</i>	55
4.1	Phase I Business Practice	56
4.2	User Characteristics	57
4.3	Data Collection	58
4.4	Data Searching and Viewing	58
4.5	Conclusion	58
5.0	<i>Model Validation</i>	59
5.1	Overview of Measurement Data	59
5.1.1	Nevada Test Site Emissions Characterization	59
5.1.2	Aberdeen Test Center	59
5.1.3	Dugway Proving Ground	60
5.2	Aberdeen Test Center Exploding Ordnance Emissions Study (EOES)- Series I, Phase II	60
5.2.1	EOES Test Data	60
5.2.2	Mass Balance	62
5.2.3	Detonation Product Emissions: Kinetic Results	63
5.3	Dugway Proving Ground Ordnance Emissions Characterization – Phase IV	65
5.4	Field Program to Identify TRI Chemicals	68
6.0	<i>Summary</i>	69
7.0	<i>Acknowledgements</i>	69
8.0	<i>References</i>	70
9.0	<i>Appendix A - Aerosol Mass Spectrometric Point-of-Fire Measurements</i>	75
10.0	<i>Appendix B: Chemical Kinetic Mechanism</i>	77

LIST OF TABLES

<i>Table 1: C-J State Properties and Major Detonation Products</i>	10
<i>Table 2. Description of Soil Categories</i>	14
<i>Table 3. Coefficients for Scaled Crater Radius</i>	14
<i>Table 4. Coefficients for Scaled Crater Depth</i>	14
<i>Table 5. Crater Volume Depletion Efficiencies.</i>	18
<i>Table 6. Particle Size Distribution Parameters Measured by Pinnick et al. [1983].</i>	19
<i>Table 7. Total Particle Number and Mass Reported by Pinnick [1983].</i>	22
<i>Table 8. Pasquill Atmospheric Stability Classes</i>	45
<i>Table 9: Summary of USAEC/ATC Exploding Ordnance Emission Studies - Series I Test Items</i>	61
<i>Table 10: Average Adjusted Emission Factor from Exploding Ordnance Emission Study, Phase II</i>	62
<i>Table 11. Carbon and Oxygen Mass Balance for the Exploding Ordnance Emission Study, Phase II.</i>	63
<i>Table 12. Ratio of SCM Predicted to Measured Mixing Ratios for Selected Detonation Products</i>	65
<i>Table 13: Summary Items Tested at DPG</i>	66
<i>Table 14: Representative Emission Factors for DPG Tests from Carson et al., 2003.</i>	67
<i>Table 15: Ratio of SCM Predicted to Measured Mixing Ratios for Selected Detonation Products</i>	68
<i>Table 16: Munitions tested under CP-1197 [C. Spicer, private communication, 2003]</i>	69
<i>Table 17: SCM Predicted to Measured Emission Factors for CP-1197 Field Test Munitions.</i>	69

LIST OF FIGURES

Figure 1. Schematic of the Source Characterization (SCM) model showing the key microphysical processes governing the release, dispersion, and deposition of gaseous and particulate emissions from HE detonations. _____	4
Figure 2. Important physical and chemical processes of pollutants emission and the soil scavenging effects. _____	5
Figure 3. Schematic of the Source Characterization Model (SCM) system architecture showing the general processing flow and relationship between the key processes governing HE detonation emissions. _	6
Figure 4. Model parameters for the quantification of chemical pollutants emitted during an explosive detonation in military test and training ranges. _____	7
Figure 5. Overview of the thermochemical detonation model showing: (top) the evolution from the initial explosive, to the initial fireball following detonation, and then to the initial puff following isentropic expansion to near ambient conditions; (left bottom) an example of detonation emission factors for selective species and their variation with the density of the initial explosive charge; and (right bottom) profiles for detonation puff temperature and mass density as a function of pressure along the adiabat. _____	9
Figure 6: Species mixing ratios for expansion along the C-J adiabat using the (a) nonideal equilibrium code CHEETAH and (b) the ideal gas equilibrium code CEA. _____	11
Figure 7. Schematic of the model for the crater formed as a the result of HE detonation. _____	13
Figure 8. Scaled crater radius vs scaled burst depth. _____	15
Figure 9. Scaled crater depth versus scaled burst depth _____	16
Figure 10. Volume reduction due to vegetation cover. $V_{c,0}$ is crater volume without vegetation effect. _	17
Figure 11. Particle number distribution using parameters from Table 6. _____	20
Figure 12. Particle mass distribution using parameters from Table 6. _____	21
Figure 13. A conceptualized view of the model for buoyant puff rise. _____	22
Figure 14. A schematic diagram of puff rise in the absence of ambient wind. _____	23
Figure 15. A schematic diagram of puff rise in the presence of ambient wind. _____	24
Figure 16. Observed and calculated fireball height and radius for a composition B mixture. _____	27
Figure 17. Sensitivity of detonation puff height and radius to explosive mass _____	27
Figure 18. The evolution of the cross-section of a puff shown at different downwind locations. _____	28
Figure 19. (a) The buoyancy-induced velocity field and the puff outer surface, and (b) positions and velocities of the puff outer surface. _____	29
Figure 20. A schematic diagram showing the mechanism of (a) large-eddy generation and (b) small-eddy generation. _____	29
Figure 21. Puff cross-sections shown for different buoyant Reynolds numbers. _____	30
Figure 22. Streamlines of Hill's spherical vortex. _____	31
Figure 23. Velocity field of a Hill's spherical vortex. _____	32
Figure 24. Buoyant puff rise and particle-laden stem formation. _____	35
Figure 25. The rise and fall of particles with diameter 100 μm . _____	37
Figure 26. The rise and fall of particles of various diameters in a buoyant puff: red-20 μm , green-40 μm , blue-60 μm , cyan-80 μm , yellow-100 μm , and purple-120 μm . _____	39
Figure 27. Number of particles in the buoyant puff at different times: (a) for duration up to 100 seconds, (b) for the first 10 seconds. _____	40
Figure 28. A schematic diagram on the buoyant puff rise and particles fall off. _____	42
Figure 29. Overview of SCM chemical kinetic reaction sets. _____	48
Figure 30. RDX decomposition and oxidation in post-detonation gases _____	49
Figure 31. RDX half-life and C-J adiabat pressure as a function of puff temperature. _____	49

LIST OF ACRONYMS

ADORA	Atmospheric Dispersion of Reacting Agents
AMS	Aerosol Mass Spectrometer
ARI	Aerodyne Research, Incorporated
ARMED	Army Range and Munitions Environmental Data
ATC	Aberdeen Test Center
BKW	Becker-Kistiakowsky-Wilson
CAAA	Clean Air Act Amendments
CEA	Chemical Equilibrium with Applications
CERCLA	Comprehensive Environmental Response, Compensation, and Liability Act
C-J	Chapman-Jouquet
CRREL	Cold Regions Research and Engineering Laboratory
DoD	Department of Defense
DODIC	Department of Defense Identification Code
DPG	Dugway Proving Ground
DREV	Defense Research and Development Branch of Canada's Department of National Defense
EM	Energetic Material
EOES	Exploding Ordnance Emission Study, Phase II
EPA	Environmental Protection Agency
EPCRA	The Emergency Planning and Community Right-to-Know Act
HE	High Energy
HMX	cyclotetramethylene tetranitramine
MMR	Massachusetts Military Reservation
NEW	Net Explosive Weight
NTS	Nevada Test Site
OB/OD	Open Burn and Open Detonation
OBODM	Open Burn and Open Detonation Model
PM2.5	Particulate matter smaller than 2.5 microns
PM10	Particulate matter smaller than 10 microns
RDX	Cyclotrimethylenetrinitramine
SERDP	Strategic Environmental Research and Development Program
SVOC	Semivolatile organic compound
USAEC	U.S. Army Environmental Center
VOC	Volatile organic compound

1.0 Introduction

A Source Characterization Model (SCM) has been developed under SERDP funding (Project CP-1159) to provide a predictive numerical tool for gaseous and particulate emissions that result from HE impact and 'blow-in-place' detonations at DoD test and training sites. Following a brief review of the background for this work and a brief summary of the SCM features and capabilities, this report presents (1) phenomenology and documentation for processes treated by the SCM, (2) a description of the USAEC Army Range and Munitions Emissions Environmental Data (ARMED), and (3) results of model testing and validation studies..

1.1 Background

1.1.1 Environmental and Public Safety Impact of Munitions Emissions

U.S. Army operations at test and training sites involve the detonation of High Energy (HE) ordnances. The chemical emissions from exploding ordnances pose a potentially dangerous environmental and health hazard. The identification of high levels of residual energetic material at the Massachusetts Military Reservation (MMR) significantly heightened public concern about the long-term consequences of test and training operations at U.S. Army sites in general. As a consequence, the U.S. Army has identified the need to: (1) quantify the ordnance detonation emissions and (2) assess the potential health and environmental impact of these emissions as critical to responding to regulatory requirements and public concerns, as well as in support of defining and possibly modifying test and training practices.

1.1.2 Emissions Characterization Test Programs

Several major emissions testing programs have been undertaken over the past decade. These emission measurement programs were largely driven by concern over the emissions during open burn and open detonation (OB/OD) operations and were designed to assist in meeting regulatory compliance requirements of the CAAA, EPCRA and RCRA. Examples are the testing programs undertaken at the Nevada Test Site (NTS) [Johnson, 1992] and Dugway Proving Ground (DPG) [Black, 1998]. The Environmental Protection Agency (EPA) published data from DPG testing [Mitchell and Suggs, 1998] that documented the identities and amounts of OB/OD products from the common bulk explosives. The resulting database greatly expanded the scarce test data available and provided a proven protocol for further testing and modeling.

More recently, emission factors for a large number of gaseous and particle emissions have been measured by researchers at the Aberdeen Test Center (ATC) through the Exploding Ordnance Emission Study, Phase II (EOES) funded by the U.S. Army Environmental Center. USAEC has also sponsored emission characterization tests at Dugway Proving Ground (DPG) [Carson, et al., 2003] and a Firing Point Emission Study at the ATC.

1.1.3 Energetic Residue from Munition Detonation

Analyses of the residues following munition detonations have confirmed explosive residues that can result in contamination of the soil and underlying ground water [Yinon and Zitrin, 1993; Jenkins et al., 2001; Thiboutot et al., 1998, Pennington et al., 2001, 2002, USACHPPM, 2000, and Hewitt et al., 2003].

1.1.4 OB/OD and Detonation Emissions Modeling

A number of models have been developed for predicting emissions from OB/OD. Examples include ADORA, PCAD, POLU, OBODM and Merlin. These models' predictive ability is limited by the uncertainties in the measured test data that have been used to tune the models and by the assumption that a mass balance focused on the major emissions would adequately represent detonation. For four representative scenarios, the predictions of some of these models compared poorly with available DPG/NTS test data [Eck et al., 1998]. The available databases and models still need to be improved to

meet the public and regulatory requirements [Banta et al., 1998]. None of the current models predict the particle size, density, and composition of condensed particles in the plume. The dry deposition patterns into the various surrounding environments are not differentiated in a single run. The process of wet deposition, for example, is not included in any of the models. Existing models fail to address the following problems:

- (1) Quantification of afterburning (after detonation) effects;
- (2) Emission factors for VOCs or semi-VOCs which are typically emitted in the parts per million range;
- (3) Predictive quantification of mass loadings and size distributions for emitted particles (smoke);
- (4) Prediction of dry and wet deposition patterns for emitted particles and acid gases on various ground surfaces or in waters;
- (5) Potential interactions of emitted pollutants with entrained soil.

Because of these problems, regulators are reluctant to accept model outputs as representative. Testing and sampling continues to be an expensive and difficult process, and it is unlikely that the DOD will ever sample emissions from all of the munitions in its inventory. Regulatory interest in the impacts from munitions detonation is high (for example, see Hunt and Huntington, 1998) and the DOD needs to cost-effectively report emissions and impacts under the Emergency Planning and Community Right-to-Know Act, the Safe Drinking Water Act, CERCLA, and RCRA. Thus, a predictive public domain model that has the capability of addressing all of these major concerns is necessary.

1.2 Source Characterization Model

1.2.1 Features and Capabilities

The SCM addresses a number of the technical issues that are important in estimating munition emission levels and particulate deposition arising from DoD test and training operation. A few of the most important features of the SCM are the following:

- A source module for characterizing the energy release and chemical speciation with munition detonation.
- Crater formation and soil particle entrainment at ground level due to detonation.
- Buoyant puff rise and the flow structure.
- Explosive residue or soil particles depletion and deposition from the puff. In this module, the spatial and temporal distribution of the amount and size of soil particles is obtained, which can be used to calculate the soil depletion terms.
- The effect of particle depletion and deposition (the fall-out of particulate matter) on the puff dynamics has been formulated. Modifications to the laws of mass conservation, momentum conservation, and energy conservation are obtained to quantify mass transfer and heat transfer for the puff due to particle fall-out.
- A chemical kinetics module for finite-rate afterburning chemistry and a particle microphysics module for characterizing the dynamics of particulate emissions and gas-to-particle conversion.
- A data-driven model for energetic material residue emissions.

Each of these features is discussed in more detail in the subsequent sections of this report.

1.3 Report Outline

The remainder of this report is organized as follows. Section 2 presents a broad overview of the SCM from a phenomenology perspective including a discussion of the specific physiochemical processes that are treated, the computational processing flow, and model inputs. The SCM is described in detail in Section 3. This includes a discussion of the modules for: (1) detonation thermochemistry, (2) crater dynamics, (3) buoyant puff rise, (4) detonation plume vortex structure, (5) particle deposition, (6) ambient meteorology, and (7) afterburning chemical kinetics, (8) heterogeneous update kinetics, and (9) energetic material emissions. Section 4 describes the USAEC ARMED database for munition emissions. Section 5 discusses the initial data analysis and model validation studies that have been performed. A summary is presented in Section 6. Technical references are presented in Section 7.

2.0 SCM Model Phenomenology

2.1 Model Overview

Figure 1 presents a pictorial representation of the phenomenology that is the basis for the SCM and the key processes governing the release, dispersion, and deposition of emissions from the detonation of HE explosives. As shown in Figure 1, three distinct stages can be identified that are differentiated by the physiochemical processes governing the important emissions, as well as the characteristic time scales.

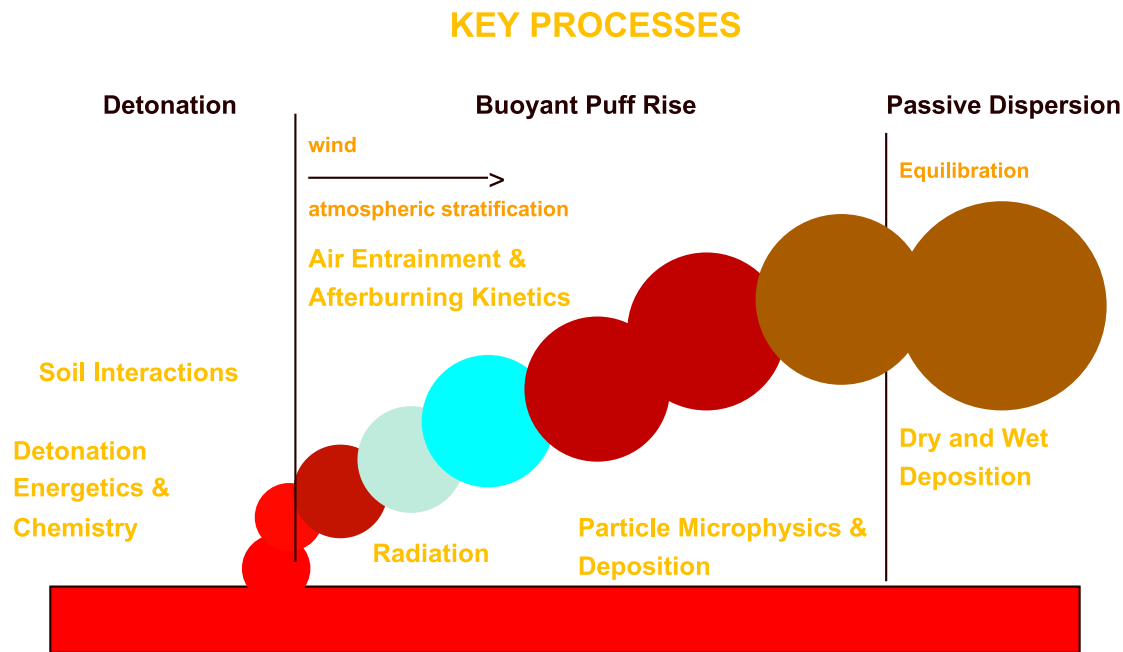


Figure 1. Schematic of the Source Characterization (SCM) model showing the key microphysical processes governing the release, dispersion, and deposition of gaseous and particulate emissions from HE detonations.

2.1.1 Stage 1: Detonation Energetics and Chemistry

Stage 1 is taken to encompass the initial detonation, a very rapid isentropic expansion of the detonation plume to near ambient conditions, formation of a detonation crater, and the initial entrainment of any soil particles. In addition, energetic material is ejected due to ablation and/or ablation with some pyrolysis. The physiochemical processes associated with Stage 1 are highly complex and collectively involve characteristic time scales ranging from a few picoseconds to a few microseconds. Consequently, a rigorous treatment of Stage 1 would be exceedingly difficult to implement, time consuming to execute, and subject to a great deal of uncertainty due to the lack of experimental data and limited knowledge of critical physical and chemical parameters. Consequently, the SCM treats Stage 1 using non-ideal gas chemical equilibrium in combination with empirical data for NO_x emission and post-blast energetic residues to provide a data-driven treatment of the Stage 1 processes.

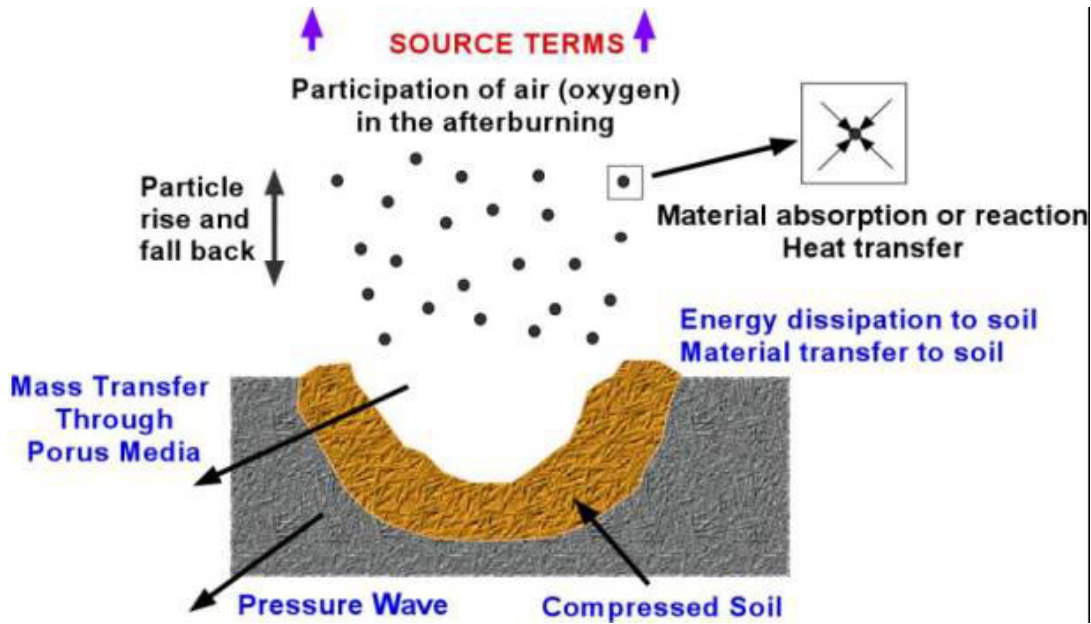


Figure 2. Important physical and chemical processes of pollutants emission and the soil scavenging effects.

Despite their complexity, Stage 1 processes play a fundamental role in determining the HE detonation emissions. Figure 2 shows a diagram on the important processes in obtaining the pollutant source terms coming out of a detonation crater. Most of the explosive energy is converted to thermal energy that drives the fireball as it moves upwards. A considerable amount of the energy is used to compress the soil and lift the soil particles to form a crater. Some energy is dissipated through sound waves propagated away in the air as well as in the ground. Immediately after the detonation, some small fraction of detonation products and thermal energy in the fireball is transferred to the ground. When the soil particles rise and fall through the hot fireball, they scavenge the pollutants as well as the thermal energy. The eventual emitted pollutants will experience further chemical reaction as more humid air is entrained into the hot fireball (Stage 2).

2.1.2 Stage 2: Buoyant Puff Rise

Stage 2 is taken to include rise of the detonation plume in a stratified atmosphere due to buoyant forces as well as downstream dispersion due to advection. Initial conditions for Stage 2 processes are based on the energy release, chemical transformations, and soil interactions that comprise Stage 1. The processes governing the buoyant puff's thermodynamic properties and chemical composition include the finite rate chemical kinetics associated with afterburning processes in the hot plume as oxygen is entrained with ambient air, as well as the loss of heavier particles, including any gas phase species adsorbed on those particles, due to deposition processes. Stage 2 is taken to continue until the detonation puff has equilibrated with the ambient atmosphere where upon the subsequent dispersion is governed by passive atmospheric dispersion (Stage 3).

2.1.3 Stage 3: Atmospheric Dispersion

Stage 3 refers to the atmospheric dispersion of released gas phase and smaller particulate emissions over longer time scales and spatial dimensions. Stage 3 is not explicitly treated by the SCM. Rather, the SCM provides initial conditions for existing state-of-the-art atmospheric codes that currently exist. The results of the SCM include: (1) the altitude, downstream distance, and volume of the detonation plume, (2) thermodynamic properties of the detonation plume, (3) the chemical composition of the detonation plume in the form of source emission factors, and (4) the near term particle fall-out pattern due to deposition.

2.2 Computational Processing Flow

Figure 3 outlines the basic system architecture for the SCM in terms of the phenomenological description that is shown in Figure 1. This provides a more detailed description of the processing flow adopted in the SCM, as well as a broad overview of the component sub-models that collectively are the basis for the SCM.

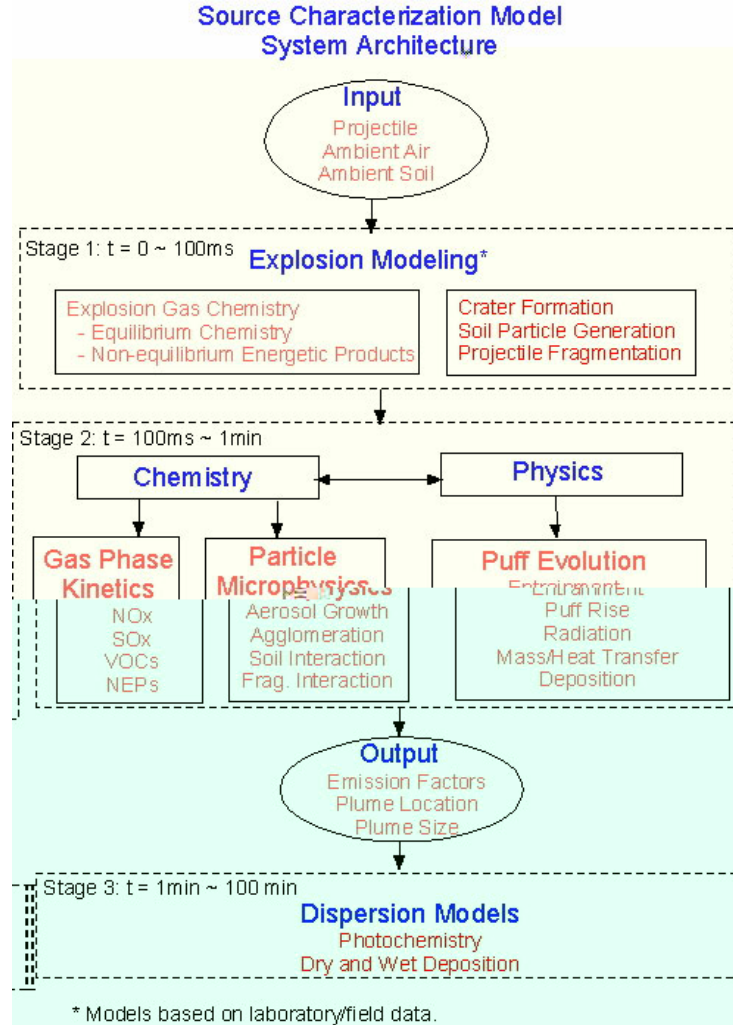


Figure 3. Schematic of the Source Characterization Model (SCM) system architecture showing the general processing flow and relationship between the key processes governing HE detonation emissions.

As indicated in Figure 3, the basic inputs to the SCM fall into three broad groups corresponding to the key parameters and properties for the projectile or explosive charge, ambient air, and soil. Figure 4 shows a schematic diagram of model parameters. They include the following:

Group 1: projectile/charge parameters: shell mass, shell volume, and explosive type and charge.

Group 2: ambient parameters: wind speed, temperature, stratification, ambient turbulence, and humidity.

Group 3: Soil parameters: soil density, compressibility, soil strength, temperature, particle size, and water content.

Model Parameters

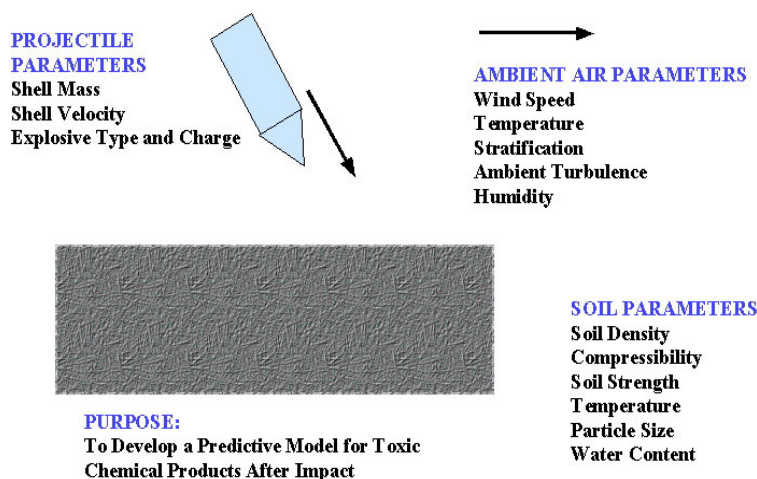


Figure 4. Model parameters for the quantification of chemical pollutants emitted during an explosive detonation in military test and training ranges.

As an example, for a bare charge, such as a simple TNT demolition charge, the input would include the chemical composition and total charge mass. For a projectile, the inputs would also include the composition of the shell casing. In addition, it is necessary to know the chemical composition and mass of any secondary, supplemental, or detonating charges for blow-in-place detonations as part of field measurement programs or the chemical contribution from the projectile propellant for impact detonations. These inputs provide the necessary data for an analysis of the explosive gas phase chemistry that forms the first part of Stage 1 in Figure 3. That analysis provides estimates for both the energy release and detonation species emission factors.

The analysis of crater formation that forms the second part of the Stage 1 modeling requires the energy release in the detonation coupled with additional inputs in order to specify soil properties and detonation depth. The result of that analysis is an estimate for crater properties and, more importantly, the mass of soil entrained in the detonation plume within the first few milliseconds after detonation.

The net result of the Stage 1 model is: (1) the energy release to the plume which, in turn, determines its initial temperature and size, (2) the initial chemical composition of the detonation plume, and (3) the mass and size distribution of entrained soil particles. Collectively, these data provide the initial conditions for the treatment of buoyant plume rise, afterburning chemical kinetics, and particle deposition in Stage 2.

With respect to modeling the Stage 2 processes, Figure 2 shows that while, at one level, it is possible to distinguish between physical processes governing the plume buoyant rise and chemical processes governing gas phase afterburning kinetics and gas phase species interactions with small entrained soil particles or release particulates from projectile casings, there is a coupling between these physical and chemical processes. Enthalpy changes due to afterburning kinetics, for example, impact the plume temperature and, consequently, the mechanisms influencing the puff's rise and downstream dispersion.

The basic outputs from Stage 2 modeling and, in essence, the SCM model as a whole, are the chemical composition, altitude, downstream distance, and size of the plume once it has equilibrated with the atmosphere. These outputs provide both a basis for analysis of the local (fence line) environmental impact of detonation emissions as well as inputs to further processing by long time atmospheric dispersion (air quality issues) or fate/transport models (ground/water pollution impact issues).

3.0 SCM Model Description

3.1 Detonation Thermochemistry and Emission Factors

3.1.1 Phenomenology

The treatment of explosive detonation focuses on predicting the energy release and other thermodynamic properties of the explosive state and the chemical composition of the mixture of detonation products. The thermodynamic properties of the detonation state play a fundamental role in determining the temperature and size of the detonation plume while the chemical composition or emission factors for detonation products provides the first best estimate for pollutants released in the blast. Empirical evidence indicates that the detonation energy is expended in a volume determined by the equivalent mass of TNT and that this initial fireball quickly expands isentropically to near the ambient pressure [Boughton and DeLaurentis, 1987]. Consequently, the initial detonation plume temperature and volume can be estimated thermochemically given the chemical composition of the explosive charge. This general process is illustrated schematically in the top panel of Figure 5.

However, if the chemical speciation is also estimated thermochemically, there are significant differences with experimental data. Bomb calorimetric data and analyses reported by Ornellas [1982] suggest that the chemistry is frozen during the isentropic expansion resulting in a detonation plume whose chemical composition is not in thermochemical equilibrium at the temperature and pressure of the isentropically expanded detonation plume. The study by Ornellas [1982] suggests that the chemistry freezes at temperatures around 2000 K which for an isentropic expansion corresponds to pressures on the order of 10,000 atm. Consequently, the SCM model estimates the initial chemical composition of the detonation plume from the high detonation pressure mixture by assuming that the expansion is significantly more rapid than the time to reach chemical equilibrium and that chemical speciation freezes out at temperatures in the range reported by Ornellas [1982]. The panel in the right bottom of Figure 5 illustrates this for an explosive charge consisting of Composition B.

Thermochemical Model for Detonation

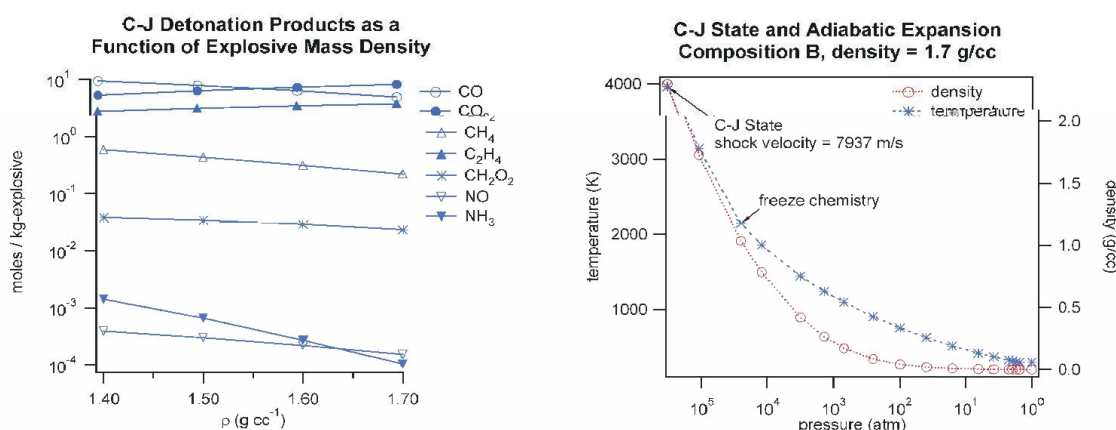


Figure 5. Overview of the thermochemical detonation model showing: (top) the evolution from the initial explosive, to the initial fireball following detonation, and then to the initial puff following isentropic expansion to near ambient conditions; (left bottom) an example of detonation emission factors for selective species and their variation with the density of the initial explosive charge; and (right bottom) profiles for detonation puff temperature and mass density as a function of pressure along the adiabat.

3.1.2 Chemical Equilibrium

Detonation pressures are on the order of several tens of thousands of atmospheres and, as noted, finite rate chemical kinetics in the expanding detonation puff freezes at pressure of approximately 10,000 atm. Consequently, non-ideal gas effects may play an important role in determining the initial speciation of a HE detonation. As part of the research in developing the SCM, both ideal gas and non-ideal gas equilibrium codes have been used to estimate chemical speciation. Specifically, the Chemical Equilibrium with Applications (CEA) code written by McBride and Gordon [1996] was used as a prototypical ideal gas equilibrium code. CHEETAH developed by Fried [1996] and based on the earlier TIGER equilibrium code [Cowperthwaite and Zwisler, 1973] was selected as the non-ideal gas equilibrium code for this analysis. Although CHEETAH comes bundled with four product libraries, the remainder of this discussion is based on the BKW library which is a computer-optimized parameterization of the BKW equation of state which was noted by Fried [1996] to give good results for explosives containing C, H, O, N, F, and Cl. The CEA codes was integrated into the SCM while CHEETAH functions as a stand-alone application whose outputs are read into SCM.

These codes were used to explore the various options for a thermochemical equilibrium treatment of both the C-J state properties and adiabatic expansion. Three features were examined: (1) initial explosive density, (2) C-J state detonation products, and (3) chemical species evolution along the adiabat. The results of that study are discussed below. However, in the discussion that follows it should be noted that energy losses to crater formation, soil entrainment, and shell fragmentation are ignored.

3.1.2.1 Initial Explosive Mass Density

Within the context of a non-ideal gas thermodynamic equilibrium treatment the detonation products depend on the initial density of the explosive. The left bottom panel in Figure 5 illustrates this dependence through the results of simulations for Composition B by showing the emission level of selected species in units of mole/kg-explosive as a function of the density for the initial explosive.

3.1.2.2 C-J State Properties

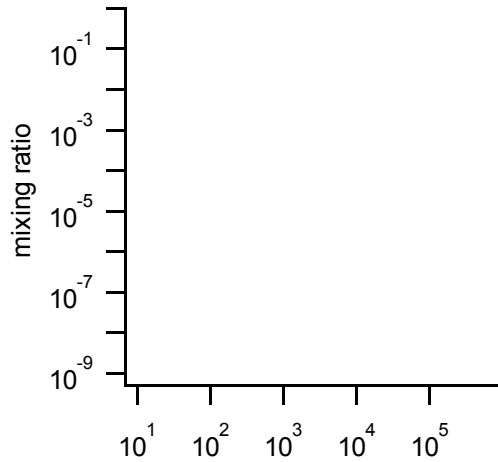
Table 1 lists C-J state properties and mixing ratios for the major detonation products. The first four columns of data illustrate the variation in properties and composition with explosive by showing data for RDX, TNT, HMX, and Comp B (60% RDX / 39% TNT / 1% wax). This data was generated using the CHEETAH nonideal gas equilibrium code [Fried, 1996]. The last column shows data for Comp B generated using the CEA ideal gas equilibrium code [McBride and Gordon, 1999]. Part of the differences in chemical composition for the last (ideal gas equation of state) set of data is due to the lack of a solid carbon phase (C^{*}). The resulting increased level of carbon in the CEA gas phase species increases the levels of CO, CH₄, and other species with carbon in a lower oxidation state and decreases the level of CO₂.

Table 1: C-J State Properties and Major Detonation Products

C-J State Properties and Composition					
	CHEETAH Nonideal Thermochemical Equilibrium				CEA Ideal Equilibrium
	RDX	TNT	HMX	Comp B	Comp B
Density (g/cc)	1.8	1.654	1.9	1.74581	na
Po (atm)	1	1	1	1	1
Vo (cc/g)	0.55369	0.60449	0.52491	0.57198	na
Eo (cal/g)	66.21027	-78.4265	60.52725	14.14103	14.16
Pressure (atm)	341763.7	191869	388620.4	282121.4	290188.4
Specific Volume (cc/g)	0.4206	0.454	0.3995	0.4301	0.04256
Temperature (K)	4191.9	3685	4113.6	4035.6	3834.9
N ₂	0.3332	0.1365	0.3332	0.2542	0.2588
H ₂ O	0.3331	0.2266	0.3332	0.2903	0.1468
CO ₂	0.1525	0.1303	0.1584	0.1444	0.0738
CO	0.0280	0.05797	0.0162	0.0382	0.3579
NO	2.09E-04	4.35E-05	1.77E-04	1.32E-04	1.76E-04
CH ₄	1.65E-05	1.35E-04	4.35E-06	6.03E-05	1.460E-02
C ₂ H ₄	1.24E-05	5.75E-05	3.02E-06	2.58E-05	9.01E-04
H ₂	5.46E-06	5.89E-05	1.14E-06	1.29E-05	8.17E-02
CH ₂ OH	3.76E-06	1.51E-05	1.16E-06	7.11E-05	2.15E-04
O ₂	3.98E-05	3.28E-06	4.79E-05	1.76E-05	1.79E-06
NH ₃	1.57E-06	1.13E-05	3.99E-07	3.62E-07	1.55E-02
CH ₂ O	7.61E-08	1.2E-06	1.27E-08	2.26E-10	< 10-15
C [*]	0.1527	0.4480	0.1586	0.2723	< 10-15

3.1.2.3 Equilibrium Speciation Along C-J Adiabatic

Figure 6 shows species mixing ratios for expansion along the C-J adiabat. In Figure 6b, the equilibrium mixture composition was obtained using the ideal gas code CEA. Notable for the nonideal gas equilibrium case is the peak level for organics, methane, ethene, and formaldehyde, at a pressure of about 10,000 atm. This pressure corresponds to temperatures between 1800 K and 2200 K depending on the particular explosive. Ornellas [1982] reports that chemical kinetics freeze during expansion at temperatures between 1800 K and 2000 K. Consequently, the estimated levels of organics based on chemical equilibrium with a pre-specified pressure or temperature for which the equilibrium products are kinetically frozen is sensitive to the point at which the equilibrium products are frozen. Additionally, this can further impact other oxidation products from afterburning as ambient air is entrained in the explosive gas. A higher level of methane for example increases fuel content of the post-detonation gas resulting in a higher afterburning temperature.



We define the detonation puff as the initial condition when this fast adiabatic expansion finishes and before ambient air and soil is entrained into the fireball. The kinetic energy of the projectile is negligible. The fragmented shell parts are ejected away far from the fireball. Thus, the mass inside the fireball is the same as the amount of explosives. (Note, subsequent treatment of the dust cloud resulting from crater formation in Section 3.2 modifies the treatment below by incorporating the mass of entrained soil.)

$$M_o = \rho_o V_o \quad (3.1.1)$$

where ρ_o and V_o are the density and volume of the initial cloud, respectively. We further assume that all the heat released from the detonation is used in increasing the fireball enthalpy:

$$H_R = M_o c_p T_o \quad (3.1.2)$$

where c_p and T_o are specific heat at constant pressure and initial cloud temperature, respectively. For simplicity, we assume the gases in the fireball follow the perfect gas law, which is:

$$p = \rho RT \quad (3.1.3)$$

where p , T , ρ , and R are pressure, temperature, density and the gas constant, respectively. Using Equations (3.1.1) - (3.1.3) and relation, $c_p = \frac{\gamma}{\gamma - 1} R$, where γ is the ratio of specific heats, the initial fireball volume is

$$V_o = \left(\frac{\gamma - 1}{\gamma} \right) \frac{H_R}{p_a} \quad (3.1.4)$$

The initial radius of the fireball (assumed spherical) can be readily obtained as:

$$r_o = \left[\frac{3}{4\pi} \left(\frac{\gamma - 1}{\gamma} \right) \frac{H_R}{p_a} \right]^{1/3} \quad (3.1.5)$$

If we use $p_a = \rho_a R T_a$, which should hold for ambient air, we have:

$$r_o = C_L \left[\frac{3}{4\pi} \frac{H_R}{\rho_a c_p T_a} \right]^{1/3} \quad (3.1.6)$$

C_L is a coefficient (smaller than 1) that represents all the neglected energy losses. The value of C_L should be obtained by field test measurements for puff size.

As an example, consider the 81-mm mortar and 60-mm mortar with explosive formulations given by:

81-mm mortar

0.95 kg of Composition B, 60% RDX and 39% TNT

0.57 kg of C4 charge, 91% RDX

60-mm mortar

0.43 kg of Composition B, 60% RDX and 39% TNT

In this calculation, only the major charges are included. The minor charges in the primer, ignition cartridge, propellant charge, booster, and fuse, and the effect of wax and plasticizers are not taken into account. Energy loss to detonation, crater formation, soil entrainment, and shell fragmentation is ignored. We assume, for simplicity, that all the heat released from the detonation goes into the fireball. The heat generation due to the afterburning is also neglected.

The heat release for the 80-mm and 60-mm rounds is 7711 kJ and 2232 kJ, respectively. Letting the ambient air density, air temperature and heat capacity be 1.2 kg/m^3 , $270 \text{ }^\circ\text{K}$, and 1.15 kJ/kg/K , respectively, then based on the approach presented above, the initial cloud radii for the 81-mm round and 60-mm round are respectively, 1.6 m and 1.1 m. The initial temperatures of the two rounds are obtained as $4411 \text{ }^\circ\text{K}$ and $4513 \text{ }^\circ\text{K}$ respectively. The initial densities of the fireballs are: 0.089 kg/m^3 and 0.077 kg/m^3 , respectively.

3.2 Crater Dynamics

In order to have an understanding of the amount of soil particles eventually entrained into the puff, we need to take account the bomb crater dynamics and the soil characteristics. The crater model is a module of the Source Characterization Model (SCM) that predicts the (1) crater mass, (2) dust cloud mass, and (3) dust cloud particle size distribution resulting from an explosion. The crater module, in conjunction with the detonation thermochemistry module discussed in Section 3.1, is used to establish initial conditions for the detonation puff. Figure 7 depicts the parameters used in the discussion that follows to describe the basic modeling approach adopted in SCM to describe crater formation and the associated dust cloud.

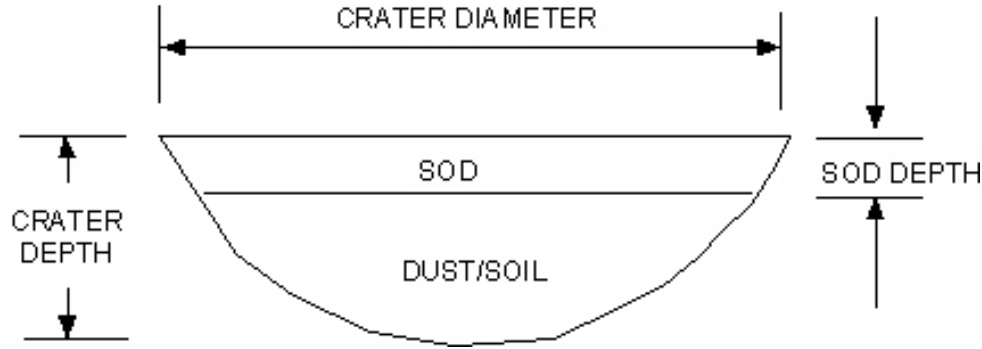


Figure 7. Schematic of the model for the crater formed as a the result of HE detonation.

3.2.1 Crater Volume

The physics of a ground level explosion includes the chemistry of the explosive and physical interactions with the soil and atmosphere. The governing differential equations are well understood [Roddy et al., 1977] and have been solved numerically to give reasonable agreement with experimental data [Knowles and Brode, 1977]. A less detailed approach has been developed, based partially on dimensional analysis, in which empirical correlations were developed using experimental data [U.S. Army Engineering, 1961]. The key mathematical relations are presented below.

The crater radius r_c (units in m) and crater depth d_c (units in m) are given by the following relations:

$$\bar{r}_c = a_0 + a_1 \lambda_c + a_2 \lambda_c^2 + a_3 \lambda_c^3 \quad (3.2.1)$$

$$\bar{d}_c = b_0 + b_1 \lambda_c + b_2 \lambda_c^2 + b_3 \lambda_c^3 + b_4 \lambda_c^4 \quad (3.2.2)$$

where \bar{r}_c , \bar{d}_c , and λ_c are the scaled crater radius, scaled crater depth, and scaled explosion depth respectively given by:

$$\bar{r}_c = \frac{r_c}{W^{\frac{1}{3}}} \quad (3.2.3)$$

$$\bar{d}_c = \frac{d_c}{W^{0.3}} \quad (3.2.4)$$

$$\lambda_c = \frac{d_b}{W^{\frac{1}{3}}} \quad (3.2.5)$$

Here W is the energy release of the explosive charge (units in equivalent *kg of TNT*) and d_b is the distance above ground of the charge (units in *m*) (d_b is negative for charge below ground). The coefficients a_i and b_i , where i denotes vector elements, are uniquely determined for a given soil type. Soil was categorized into the seven different types listed in Table 2. The corresponding coefficient parameters a_i and b_i are given in Tables 3 and 4, respectively.

Table 2. Description of Soil Categories

Category	Description
I	Rock
II	Dry cohesive soils (lightly cemented)
III	Dry sandy soils
IV	Dry to moist sand and frozen ground
V	Soft rock
VI	Wet sand, moist cohesive soils, and ice
VII	Wet cohesive soils (not saturated) and snow

Table 3. Coefficients for Scaled Crater Radius

Soil	a_0	a_1	a_2	a_3
I	0.271	-0.684	0.390	0.886
II	0.271	-0.684	0.390	0.886
III	0.386	-0.849	0.367	0.993
IV	0.503	-0.954	0.450	1.190
V	0.629	-1.080	0.264	1.120
VI	0.629	-1.080	0.264	1.120
VII	0.806	-1.280	-0.178	0.852

Table 4. Coefficients for Scaled Crater Depth

Soil	b_0	b_1	b_2	b_3	b_4
I	0.113	-0.477	0.270	1.84	1.05
II	0.134	-0.571	0.343	2.24	1.31
III	0.189	-0.840	0.447	3.30	2.10
IV	0.251	-1.17	0.494	4.72	3.34
V	0.189	-0.840	0.447	3.30	2.10
VI	0.331	-1.49	0.579	4.92	3.13
VII	0.449	-1.82	0.322	4.11	2.02

Scaled crater radius and scaled crater depth are plotted in Figures 8 and 9, respectively. All curves follow similar patterns. For the range of λ_c shown, the curves lie approximately within an order of magnitude, and they increase with decreasing scaled burst depth up to a critical scaled burst depth where scaled crater radius and depth reach a maximum and decrease thereafter. For a given scaled burst depth the scaled crater radius and depth increase with increasing soil category number. Recall from Table 2 that the soil category numbers increase with decreasing soil “hardness.” Thus, for given energy release and charge depth, the crater formed will be larger for a “softer” soil.

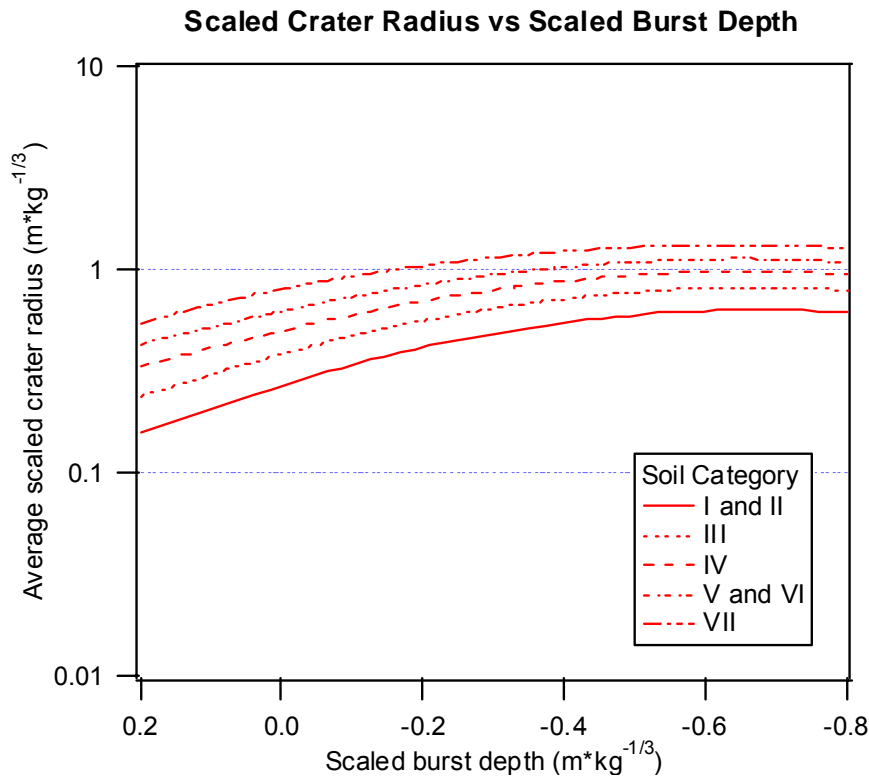


Figure 8. Scaled crater radius vs scaled burst depth.

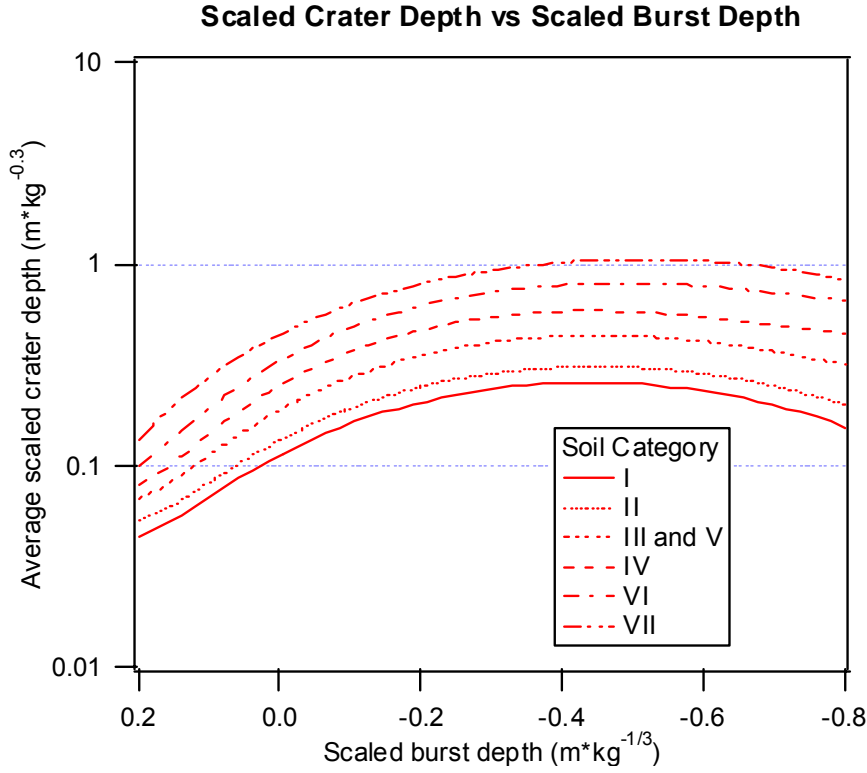


Figure 9. Scaled crater depth versus scaled burst depth

The crater formed is assumed to be ellipsoidal in shape. One soil characteristic not included up to this point is vegetation cover. It was determined in a previous report [Ebersole et al., 1980] that the crater volume is reduced by the presence of vegetation cover. The crater volume, including the effect of vegetation cover, is given by:

$$V_c = \frac{2}{3} \pi r_c^2 d_c \left\{ 1 - \frac{3 d_s}{2 d_c} \left[1 - \frac{1}{3} \left(\frac{d_s}{d_c} \right)^2 \right] \right\} \quad (3.2.6)$$

where V_c is the crater volume, which contains soil only (no sod), r_c and d_c are the crater radius and depth mentioned earlier, and d_s is the sod depth. Equation (3.2.6) is plotted in Figure 10. In the figure, the equation has been normalized such that:

$$V_{c,0} = \frac{2}{3} \pi r_c^2 d_c \quad (3.2.7)$$

The curve is parabolic in shape with a minimum at $d_s/d_c = 1$.

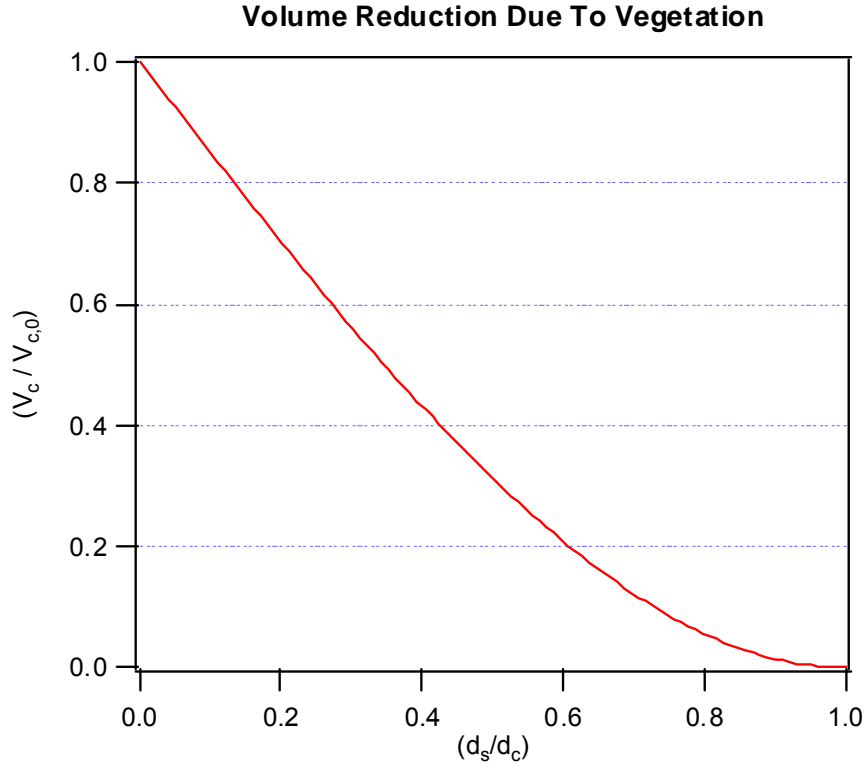


Figure 10. Volume reduction due to vegetation cover. $V_{c,0}$ is crater volume without vegetation effect.

3.2.2 Dust Cloud Mass

The primary system of interest for the SCM model is the dust cloud produced by the explosion. Of the mass associated with the crater volume only a fraction ends up in the initial hot air mass (or puff) resulting from the explosion. In this section, relations for predicting the total mass of soil particles in the puff, which were developed in a previous report [Pinnick et al., 1983], are presented.

The mass of soil particles in the puff M_{dust} is given by:

$$M_{dust} = \rho_{soil} V_c \eta_{case} \eta_{sod} \eta_{silt} \eta_{soil} \eta_{partition} \quad (3.2.8)$$

where:

$$\eta_{soil} = \eta_{compaction} \eta_{lip} \eta_{agglomeration} \quad (3.2.9)$$

where the η 's are efficiency factors which effectively deplete the crater volume mass. These efficiencies are presented in Table 5. As stated in the report by Pinnick et al. [1983], "Values indicated with a question mark show uncertainties due to insufficient experimental data."

Table 5. Crater Volume Depletion Efficiencies.

Symbol	Description	Value Given*	Value Used
η_{casing}	Effect of artillery shell fragment kinetic energy on available explosive energy	0.6 for projectile 1 for bare charge	0.6 for projectile 1 for bare charge
η_{sod}	Dust depletion due to sod cover	1	1
η_{silt}	Fraction of small (< 75mm) soil particles subject to aerodynamic arrest	0.25-0.35	0.3
$\eta_{\text{compaction}}$	Dust depletion due to compaction of crater soil	0.6 (?)	0.6
η_{lip}	Dust depletion due to crater ejecta deposition on crater lip	0.4 (?)	0.4
$\eta_{\text{agglomeration}}$	Dust depletion due to agglomeration of ejecta under dynamic (explosive) loading	0.1 – 0.5 (?)	0.3
$\eta_{\text{partition}}$	Fraction of initial dust deposited in buoyant cloud	0.2 – 0.8 (?)	0.5
$1-\eta_{\text{partition}}$	Fraction of dust deposited in non-buoyant dust skirt	0.8 – 0.2 (?)	0.5

* Question marks show uncertainty due to insufficient data.

Consider a sample calculation of bare charge. The mass of soil particles in the buoyant cloud is calculated by:

$$\left(\frac{M_{\text{dust}}}{M_{\text{crater}}} \right) = \eta_{\text{casing}} \eta_{\text{sod}} \eta_{\text{silt}} \eta_{\text{compaction}} \eta_{\text{lip}} \eta_{\text{agglomeration}} \eta_{\text{partition}} \quad (3.2.10)$$

$$\Rightarrow \left(\frac{M_{\text{dust}}}{M_{\text{crater}}} \right) = 1.08\%$$

Thus, for this case only approximately 1% of the crater soil particles end up in the buoyant cloud.

3.2.3 Dust Cloud Particle Distribution

In order to quantify the particle size distribution experimental measurements are needed. We have found only one instance where a size distribution was measured directly on an explosion-produced dust cloud, reported by Pinnick *et al.* [1983]. The results from this study, which are presented below, are used to quantify the soil particle distribution entrained in the cloud.

This group set off explosions on four occasions, in three different types of soils and with varying charge type and size. They measured the soil distribution approximately 30m downwind of the blast (as the cloud passed over). The three soil types were “clay”, “sandy clay”, and “sand to silty sand”. Their instrumentation was sensitive to soil sample particles in the range of 2 to 100 μm , and to airborne dust particles in the range of 0.2 to 100 μm . Their tests showed variations in the soil distributions from location to location, but the cloud distributions were amazingly similar at each site. All measured cloud size distributions could be roughly fit by a single bimodal lognormal distribution.

The single lognormal number distribution is given by, [following Seinfeld and Pandis, 1998]:

$$n_N(D_p) = \frac{dN}{dD_p} = \frac{N}{\sqrt{2\pi} D_p \ln(\sigma_g)} \exp\left(-\frac{[\ln(D_p) - \ln(\bar{D}_{pgN})]^2}{2 \ln^2(\sigma_g)}\right) \quad (3.2.11)$$

where N is the total number of particles per unit volume, D_p is particle diameter, \bar{D}_{pgN} is the geometric mean or median of the particle number distribution, and σ_g is the geometric standard deviation. Pinnick's results are summarized in Table 6.

Table 6. Particle Size Distribution Parameters Measured by Pinnick *et al.* [1983].

	Small mode	Large Mode
N (particles/ cm^3)	200	0.07
\bar{D}_{pgN} (microns)	1.0	45.0
σ_g	2.6	1.87

A bimodal lognormal distribution is simply the sum of two lognormal distributions.:

$$n_N(D_p) = n_{N,small}(D_p) + n_{N,large}(D_p) \quad (3.2.12)$$

The number distribution, using the parameters in Table 6, is plotted in Figure 11. It is evident that the small mode dominates the particle number distribution. This result can be somewhat misleading. The particle number distribution is useful when dealing with the kinetics of the system. However when dealing with the mechanics of the system, the mass distribution is the primary distribution of interest.

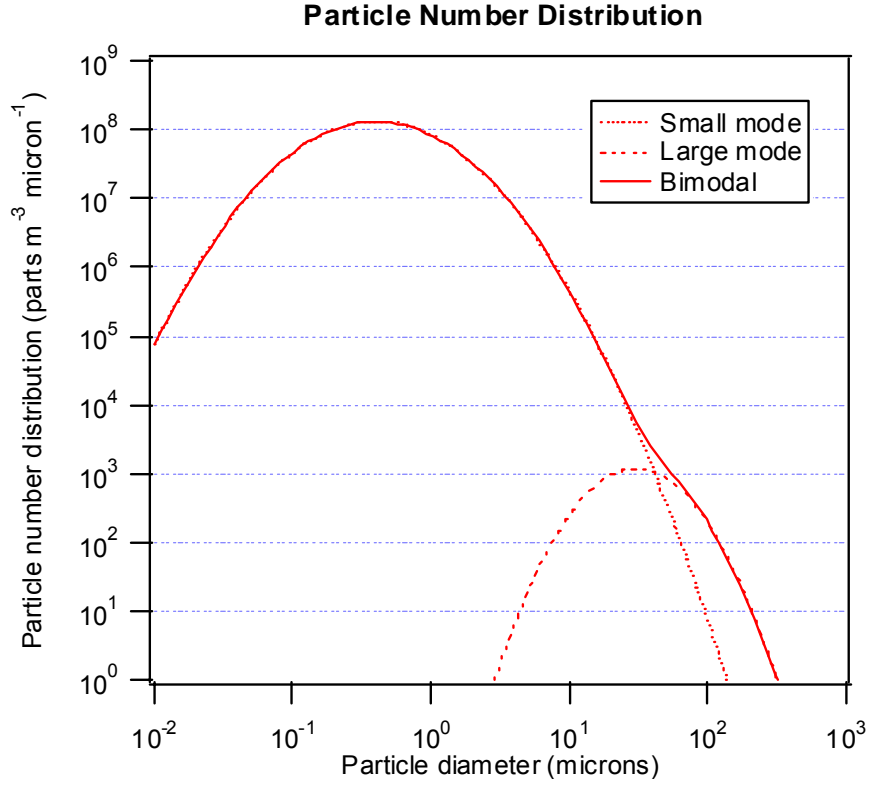


Figure 11. Particle number distribution using parameters from Table 6.

The particle mass distribution is related to the particle number distribution by:

$$dM = \rho \frac{\pi}{6} D_p^3 dN \Rightarrow n_M(D_p) = \rho \frac{\pi}{6} D_p^3 n_N(D_p) \quad (3.2.13)$$

Combining equations (3.2.13) and (3.2.11) gives:

$$n_M(D_p) = \frac{dM}{dD_p} = \frac{\pi D_p^3 N}{6\sqrt{2\pi} D_p \ln(\sigma_g)} \exp\left(\frac{-[\ln(D_p) - \ln(\bar{D}_{pgN})]^2}{2\ln^2(\sigma_g)}\right) \quad (3.2.14)$$

As it stands the above equation is not in the usual lognormal form. Rearranging gives:

$$n_M(D_p) = \frac{M}{\sqrt{2\pi} D_p \ln(\sigma_g)} \exp\left(\frac{-[\ln(D_p) - \ln(\bar{D}_{pgM})]^2}{2\ln^2(\sigma_g)}\right) \quad (3.2.15)$$

where M is the total mass of particles per unit volume, and \bar{D}_{pgM} is the median particle diameter for the mass distribution. The mass distribution has the same geometric standard deviation as the number distribution. M is given by:

$$M = \rho N \frac{\pi}{6} \overline{D}_{pgM}^3 \exp\left[\frac{9}{2} \ln^2(\sigma_g)\right] \quad (3.2.16)$$

and \overline{D}_{pgM} is given by:

$$\overline{D}_{pgM} = \overline{D}_{pgN} \exp\left[3 \ln^2(\sigma_g)\right] \quad (3.2.17)$$

Similar to the number distribution, the bimodal lognormal mass distribution is the sum the lognormal mass distributions.

$$n_M(D_p) = n_{M,small}(D_p) + n_{M,large}(D_p) \quad (3.2.18)$$

The mass distribution, using the parameters in Table 6, is plotted in Figure 12. The bimodal mass distribution is more evenly distributed between the small diameter mode and the large diameter mode than was seen in the number distribution.

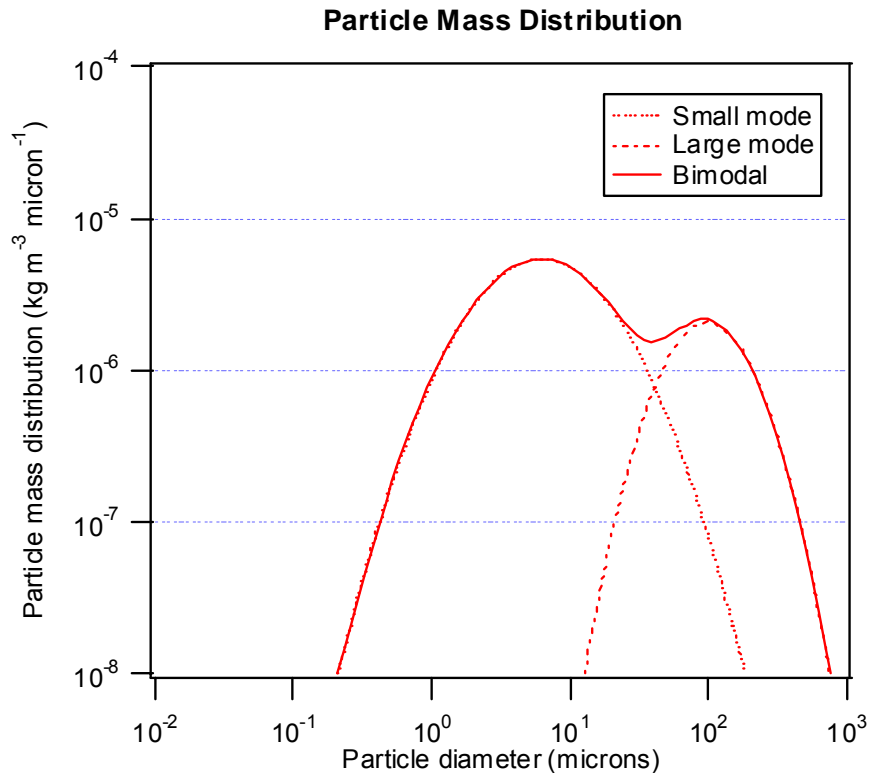


Figure 12. Particle mass distribution using parameters from Table 6.

Pinnick also presented values of total particle mass. Here the results are reproduced in an effort to provide a self-consistency check. A soil density of $\rho = 2.5 \text{ g cm}^{-3}$ was assumed. Using Equation (3.2.16) gives $M = 1.59\text{E-}5 \text{ kg m}^{-3}$ for the small mode and $M = 4.89\text{E-}5 \text{ kg m}^{-3}$ for the large mode. These values are the same as those reported by Pinnick. The total number and mass of the particle distributions are summarized in Table 7. The table shows that $N_{small} \gg N_{large}$ while $M_{large} > M_{small}$. This result reflects on the relatively large difference in median diameters for the two modes.

Table 7. Total Particle Number and Mass Reported by Pinnick [1983].

	Small mode	Large mode
N (particles m ⁻³)	2.00E ⁺⁶	0.07E ⁺⁶
M (kg m ⁻³)	1.59E ⁻⁵	4.89E ⁻⁵

3.3 Puff Fluid Dynamics

A phenomenological description of the puff rise model is shown in Figure 2. In this relatively simple model, the puff is treated as a spatially homogeneous sphere of mass M in a stratified atmosphere. The ambient properties are uniform in a horizontal plane for a given altitude, z , with the wind direction dictating a unique horizontal, x , direction. The puff then rises due to buoyancy relative to the atmosphere and moves horizontally due to advection. In addition, the total mass of the puff changes as ambient air is entrained. Lastly, the enthalpy of the evolving puff is changing due to a number of factors including radiative cooling, air entrainment, gas phase chemical reactions, and gas-particle phase changes.

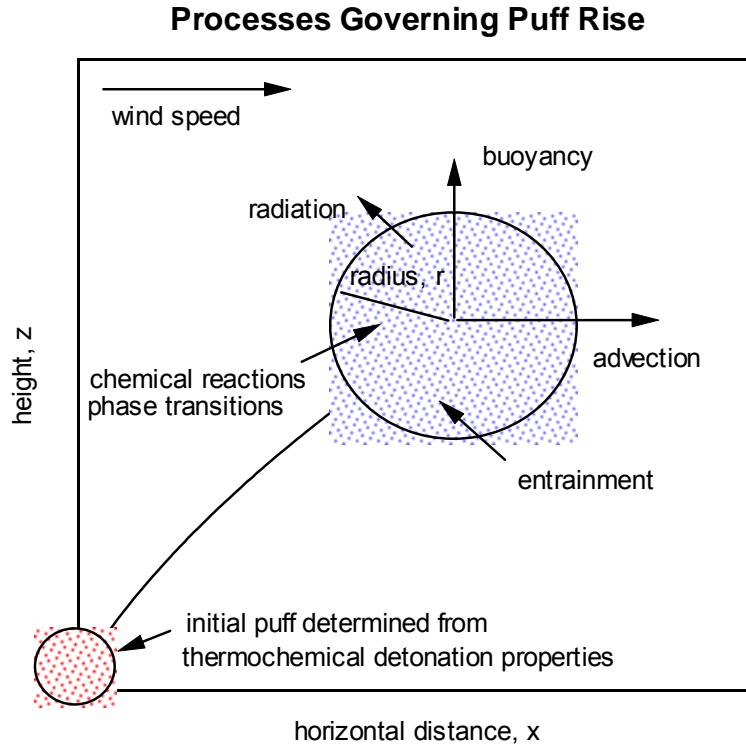


Figure 13. A conceptualized view of the model for buoyant puff rise.

3.3.1 Analytical Results

A buoyant puff rise model for an instantaneous release of hot materials in a stable atmosphere with cross wind has been developed [Zhang et al, 1996]. The major results are summarized below. The model applies the conservation laws of mass, momentum, and energy to calculate the puff motion. The entrained air into the puff is assumed to be proportional to the puff's outer surface area and the velocity difference between

the puff and the surrounding air. Simple analytical formulas for the puff trajectory and final equilibrium height in a crosswind and stratified atmosphere are obtained. In the case where the ambient wind is absent, the model results are fully validated in terms of entrainment relation, puff rise trajectory, and final puff rise.

When a positively buoyant puff is released into the atmosphere, it rises due to its buoyancy and its size increases due to entrainment. In a stably stratified atmosphere, the puff eventually equilibrates at a certain height.

(a) No Ambient Wind

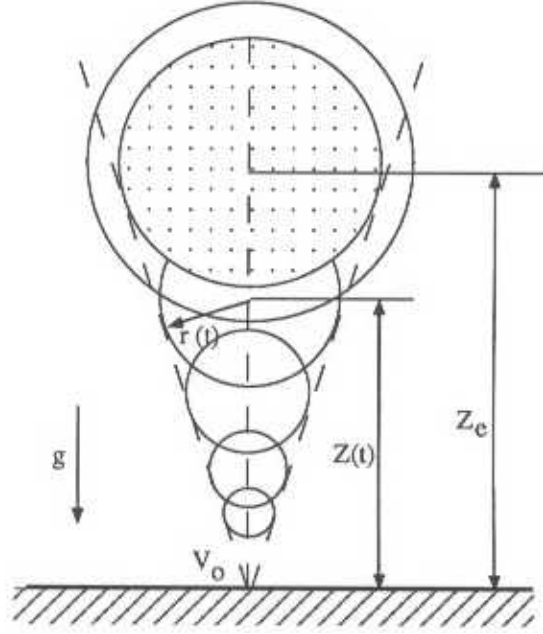


Figure 14. A schematic diagram of puff rise in the absence of ambient wind.

In the absence of an ambient wind the puff rises vertically as shown in Figure 14. We assume that the puff is of spherical shape with radius $r(t)$ and height $z(t)$ at time t . The puff final rise is:

$$z_f = \left[\frac{3V_0 g'}{\pi \alpha^3 N^2} \right]^{1/4} \quad (3.3.1)$$

where α is the entrainment coefficient; V_0 is the initially released pollutant volume; $g' = g \frac{\rho_a - \rho_0}{\rho_a}$ is the reduced gravity; g is the gravitational acceleration; ρ_a and ρ_0 are the ambient air density and the puff density at its releasing time, respectively. $N = \sqrt{-\frac{g}{\rho_a} \frac{d\rho_a}{dz}}$ is the so-called Brunt-Vaisaila frequency characterizing the strength of the ambient stratification. Its value can be calculated by using :

$$-\frac{g}{\rho_a} \frac{d\rho_a}{dz} = \frac{g}{T_a} \left(\frac{dT_a}{dz} + \frac{g}{c_p} \right), \text{ where } \frac{g}{c_p} = 9.76 \times 10^{-3} \text{ deg K / m.} \quad (3.3.2)$$

In the initial stage, $Nt \ll 1$, the puff radius and rise trajectory are:

$$r = \left[\frac{3\alpha V_o g'}{2\pi} \right]^{\frac{1}{4}} t^{\frac{1}{2}} \quad (3.3.3)$$

$$z = \left[\frac{3V_o g'}{2\pi \alpha^3} \right]^{\frac{1}{4}} t^{\frac{1}{2}} \quad (3.3.4)$$

When t is small, $Nt \ll 1$, the trajectory for a puff in stratified atmosphere, Equation (3.3.4), does not involve the stratification parameter. This is because the stratification effect on the puff rise is small initially.

The entrainment relation between puff radius and puff rise is simply:

$$r = \alpha z \quad (3.3.5)$$

It is found that the entrainment coefficient α has a small range of variation from 0.26-0.30 (Zhang et al, 1998).

(b) Large Ambient Wind, $P = u_a N / g' \gg 1$

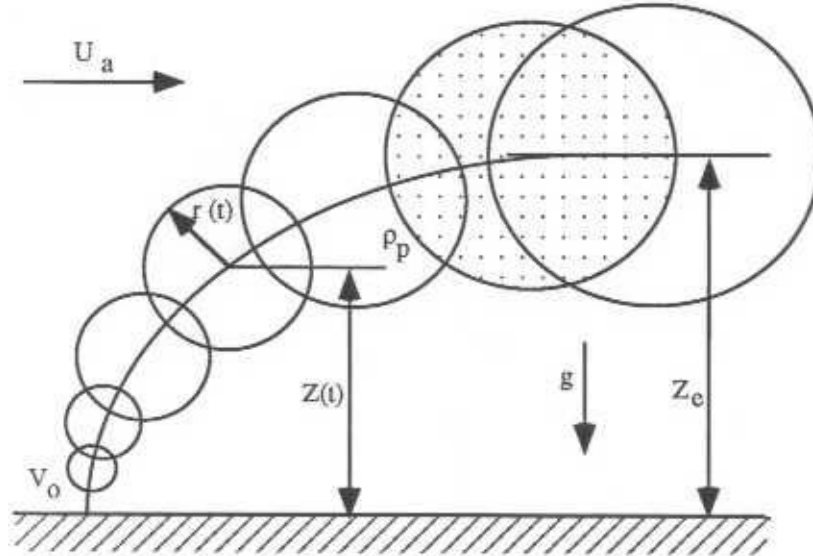


Figure 15. A schematic diagram of puff rise in the presence of ambient wind.

This case occurs when the ambient wind is higher or the stratification is strong and the puff buoyancy is weak. We first examine the puff expansion and trajectory when $Nt \ll \pi/2$ and the dimensionless parameter $P = u_a N / g' \gg 1$, where u_a is the horizontal ambient wind velocity.

$$r = \left[\frac{3\alpha V_o u_a}{\pi} \right]^{\frac{1}{4}} t^{\frac{1}{4}} \quad (3.5.6)$$

$$z = \frac{1}{5} \left[\frac{3V_o g'^4}{\pi \alpha^3 u_a^3} \right]^{\frac{1}{4}} t^{\frac{5}{4}} \quad (3.5.7)$$

The maximum puff rise in the presence of large wind, $P = u_a N / g' \gg 1$, can be obtained as:

$$z_e = \frac{g'}{5} \left[\frac{3V_o \pi^4}{32\alpha^3 u_a^3 N^5} \right]^{\frac{1}{4}} \quad (3.5.8)$$

Using the dimensionless parameter $P = u_a N / g'$ and denoting the maximum puff rise, see Equation (3.3.1), in the absence of wind as z_f , we can rewrite Equation (3.3.8) as simply:

$$\frac{z_e}{z_f} = 0.3 P^{-3/4} \quad (3.3.9)$$

The relation between puff radius and downwind distance x is:

$$r = \left[\frac{3\alpha V_o}{\pi} \right]^{\frac{1}{4}} x^{\frac{1}{4}} \quad \text{for} \quad \frac{N x}{u_a} \leq \frac{\pi}{2} \quad (3.3.10)$$

The puff rise trajectory formula expressed as a function of downwind distance x is:

$$z = \frac{1}{5} \left[\frac{3V_o}{\pi \alpha^3} \right]^{\frac{1}{4}} \frac{g'}{u_a^2} x^{\frac{5}{4}} \quad \text{for} \quad \frac{N x}{u_a} \leq \frac{\pi}{2} \quad (3.3.11)$$

This relation can be used in designing the proper allocation of measurement devices in performing field experiments.

(c) Wind Effect

The ratio of puff rise with and without wind is:

$$\eta = \frac{z_e}{z_f} = \begin{cases} 0.3 P^{-3/4} & P \geq 1 \\ e^{-1.2\sqrt{P}} & P \leq 1 \end{cases} \quad (3.3.12)$$

3.3.2 Governing Equations

Boughton and DeLaurentis [1987] developed an integral model of puff rise from HE detonations. This model is based on an integration of the partial differential conservation equations across the puff cross section assuming a fully axisymmetric, spherical puff. It includes atmospheric stratification and cross flow, as well as moisture thermodynamics assuming an equilibrium mixture of dry air and water. Quantitative analysis of model results based on the predicted top cloud height found that model predictions were within 25% of measurements for high explosive tests using TNT and Cyclotol that were performed at the Tonopah Test Range.

The SCM puff rise model was developed starting with the treatment given by Boughton and Delaurentis [1987]. The model was then extended by including enthalpy terms for gas phase chemistry (Section 3.7) and changes in total mass through particle deposition (Section 3.5). The resulting system of ODEs are then given by:

$$\frac{dM}{dt} = E \rho_{ambient} \quad (3.3.13a)$$

$$\frac{dp_z}{dt} = \frac{dM}{dt} v_x \quad (3.3.13b)$$

$$\frac{dp_z}{dt} = \left(\frac{4\pi}{3} r^3 \right) [\rho_{ambient} - \rho_{puff}] g \quad (3.3.13c)$$

$$\frac{dx}{dt} = \frac{p_x}{M} \quad (3.3.13d)$$

$$\frac{dz}{dt} = \frac{p_z}{M} \quad (3.3.13e)$$

$$\begin{aligned} \frac{dH}{dt} = & \left[\frac{dH}{dt} \right]_{radiation} + \left[\frac{dH}{dt} \right]_{entrainment} \\ & + \left[\frac{dH}{dt} \right]_{chemistry} + \left[\frac{dH}{dt} \right]_{condensation / evaporation} \end{aligned} \quad (3.3.13f)$$

In the above equations, t is time, M is the puff mass, r is the puff radius, g is the gravitational constant, (x, z) are the horizontal and vertical positions relative to the source, (p_x, p_z) are horizontal and vertical momenta, and $\rho_{ambient}$ and ρ_{puff} are the densities of the ambient atmosphere and puff, respectively. The change in momentum in the horizontal direction depends on the wind speed (v_x), while the change in momentum in the vertical direction depends on the difference in density between the puff and ambient environment. The change in mass depends on the entrainment rate, E , and ambient density, $\rho_{ambient}$. In equation (3.3.13f) pressure changes are not explicitly shown since they are negligible relative to the other terms.

The entrainment rate is given by:

$$E = 4\pi r^2 \alpha |V_r| \quad (3.3.14)$$

where r is the puff radius and $|V_r|$ is the relative velocity, $|V - V_{amb}|$. The entrainment coefficient, α , is a semi-empirical factor that is determined by model calibration with field data.

The set of ODEs for puff rise depend on the puff temperature and, as indicated in the above equations, the enthalpy of the puff is changing in response to a number of factors, including adiabatic cooling, radiative heat losses, and enthalpy changes induced by chemical reactions.

To solve the ODEs, an interface was developed and specifically applied to the Livermore Solver for Ordinary Differential Equations (Isode), which can be used to solve initial-value problems for stiff, and non-stiff systems for first order ODEs.

The SCM puff rise module has been used to compute the puff height and radius as a function of time for an above ground detonation of a Composition B mixture. A comparison between model predictions and available observations is shown in Figure 16. In general, the model predictions were found to agree well with the reported data.

To better evaluate the results shown in Figure 16, the sensitivity of model predictions for the detonation puff height and radius to the mass of the explosive charge is shown in Figure 17. Model predictions for puff height were found to be more sensitive than puff radius.

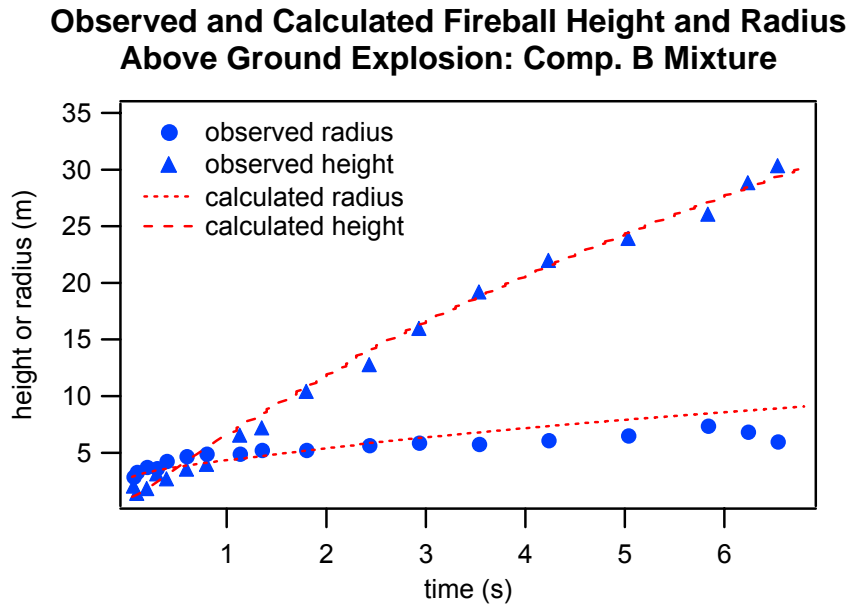


Figure 16. Observed and calculated fireball height and radius for a composition B mixture.

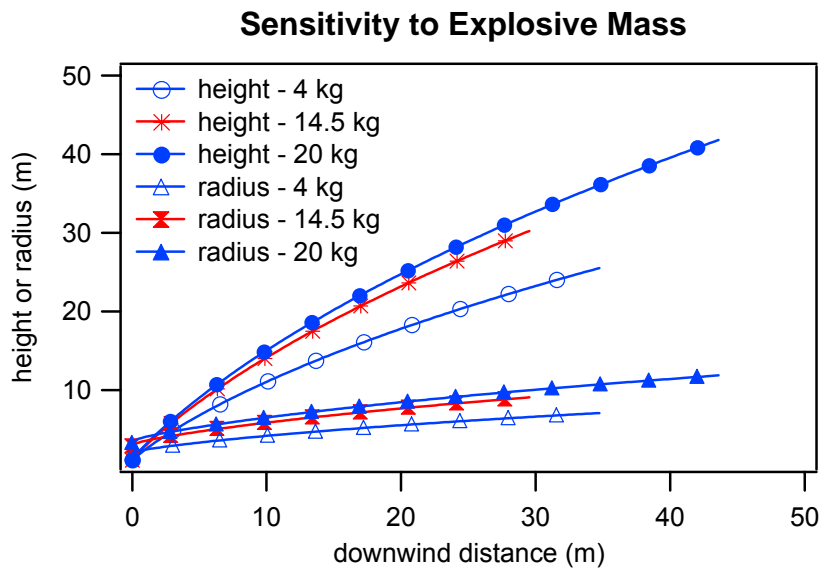


Figure 17. Sensitivity of detonation puff height and radius to explosive mass

3.4 Buoyant Puff Flow Structure

3.4.1 Vortex Method Modeling

To understand the particle deposition process from a buoyant puff (Section 3.5), it is important to know the flow structure inside and outside of the buoyant puff, since the uprising puff exerts an upward drag force on falling particles. Since not much field experimental work is available in providing the information, we will rely on numerical results obtained by solving Navier-Stokes fluid dynamics equations.

In the following, we will show some numerical results to illustrate the turbulent flow structure in a buoyant puff. For details regarding the modeling techniques, readers are referred to Zhang and Ghoniem (1993) for planar two-dimensional calculations and Issam (2000) for axisymmetric two-dimensional calculations. Most of the figures in this section are from the planar 2-d case.

Zhang and Ghoniem (1993) developed a computational model for the rise and dispersion of a wind-blown, buoyancy-driven puff in a stratified atmosphere. Lagrangian numerical techniques, based on the extension of the vortex method to variable density flows, are used to solve governing equations. The puff rise trajectory and the dispersion of its materials in the crosswind plane are obtained. It is found that the computed trajectory agrees well with the two-thirds power law of a buoyancy-dominated puff. The crosswind section of a wind blown buoyant puff is similar to the meridional section of a rising puff in the absence of wind. The puff cross-section exhibits a kidney-shaped pattern, as observed in many laboratory and field experiments. This pattern is due to the formation of two counter-rotating vortices that develop as baroclinically generated vorticity rolls up on the side of the puff. Figure 18 shows the evolution of the cross-section of a puff at different downwind locations (only half of the plane is shown here due to symmetry).

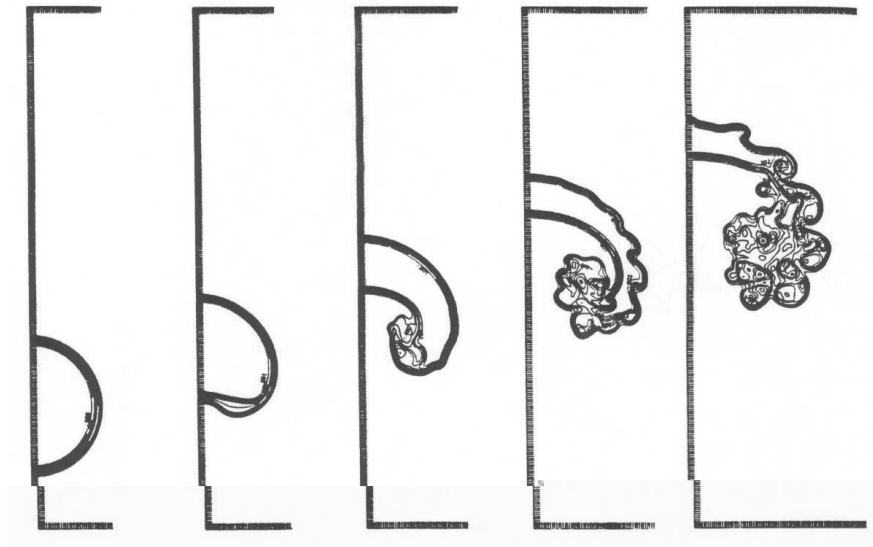


Figure 18. The evolution of the cross-section of a puff shown at different downwind locations.

The flow structure is dominated by a large-scale vortex. Figure 19 shows the flow structure inside and outside of the puff as well as on the puff external surface. Small-scale eddy structures can also be seen.

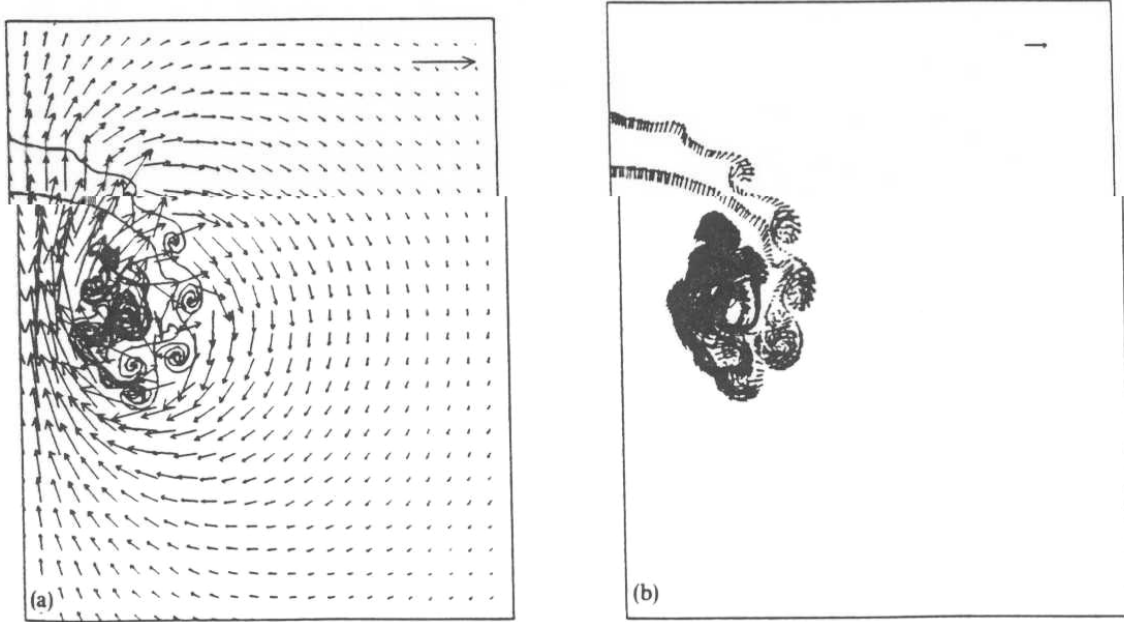


Figure 19. (a) The buoyancy-induced velocity field and the puff outer surface, and (b) positions and velocities of the puff outer surface.

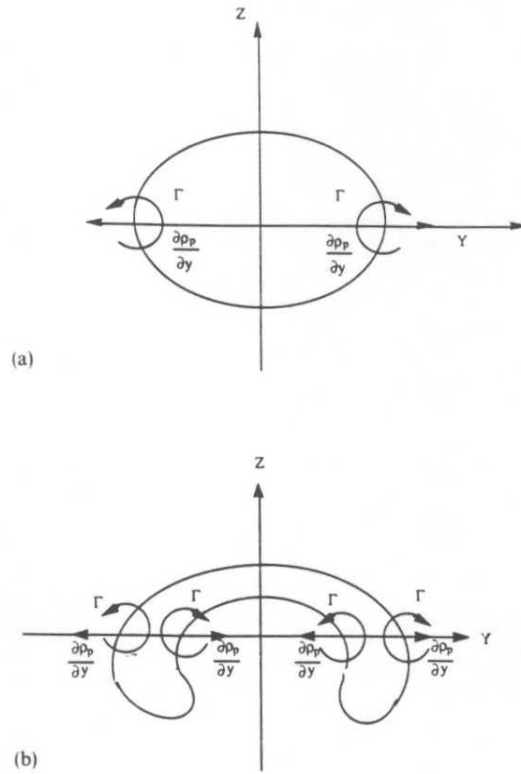


Figure 20. A schematic diagram showing the mechanism of (a) large-eddy generation and (b) small-eddy generation.

The flow field and the vorticity generation pattern is illustrated in Figure 20, which is a schematic diagram showing the baroclinic-vorticity generation. The vorticity generation term is proportional to the horizontal density gradient. For a puff of initially elliptical shape, or circular shape, the large scale, counter-rotating, streamwise vortices are formed due to the opposite horizontal density gradient, leading to a large scale rollup which changes the puff shape significantly from that described by the traditional Gaussian type concentration distribution. The vortex structure induces a velocity field that moves the puff upwards. After this large-scale rollup, the puff external surface is stretched and distorted, secondary vortices, with the same or the opposite sign of vorticity, are generated and the puff motion becomes turbulent as shown in Figure 20 (b). After the large-scale rollup, both positive and negative circulations are generated, but the total circulation remains constant.

Figure 21 shows the effect of Reynolds number on the puff shape. For large puff with strong buoyancy, the puff motion is turbulent; for small puff with weak buoyancy, the motion is laminar. However, the puff sectional shape is always dominated by the large-scale vorticity.

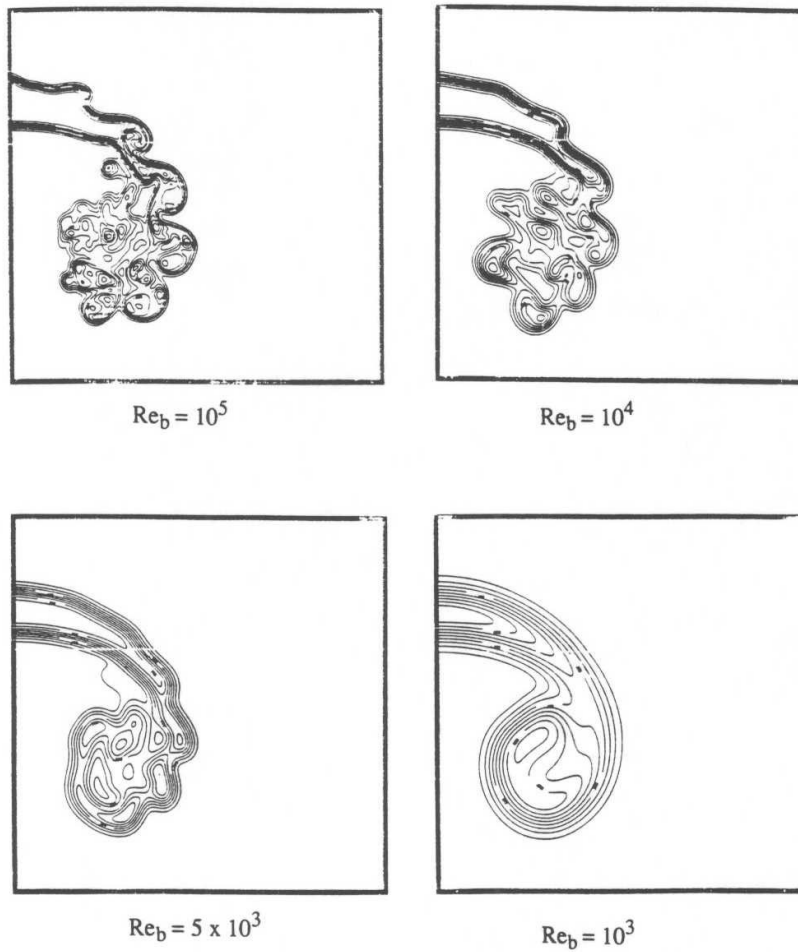


Figure 21. Puff cross-sections shown for different buoyant Reynolds numbers.

In summary, the numerical simulation shows the following characteristics of the puff motion, which will be used in the following sections:

- A large-scale vortex ring dominates the puff motion.
- The circulation of the vortex ring keeps constant as the puff rises.

The value of this circulation is proportional to the horizontal density gradient integrated over the vertical extent of the puff.

3.4.2 Extending Hill's Vortex Modeling

3.4.2.1 Hill's Spherical Vortex

For detailed derivation of Hill's vortex flow structure, the readers are referred to Article 165 of Lamb [1945]. Denoting r, z as the horizontal and vertical distance from the vortex center, the stream function of the flow field of a Hill's vortex can be expressed as:

$$\psi = \frac{1}{2} W r^2 \left[1 - \frac{a^3}{(r^2 + z^2)^{3/2}} \right] \quad \text{for} \quad R > a \quad (3.4.1a)$$

$$\psi = -\frac{3W}{4a^2} r^2 [a^2 - R^2] \quad \text{for} \quad R < a \quad (3.4.1b)$$

where a is the radius of the spherical vortex, $R = \sqrt{r^2 + z^2}$, and W is the upward self-induced vertical velocity.

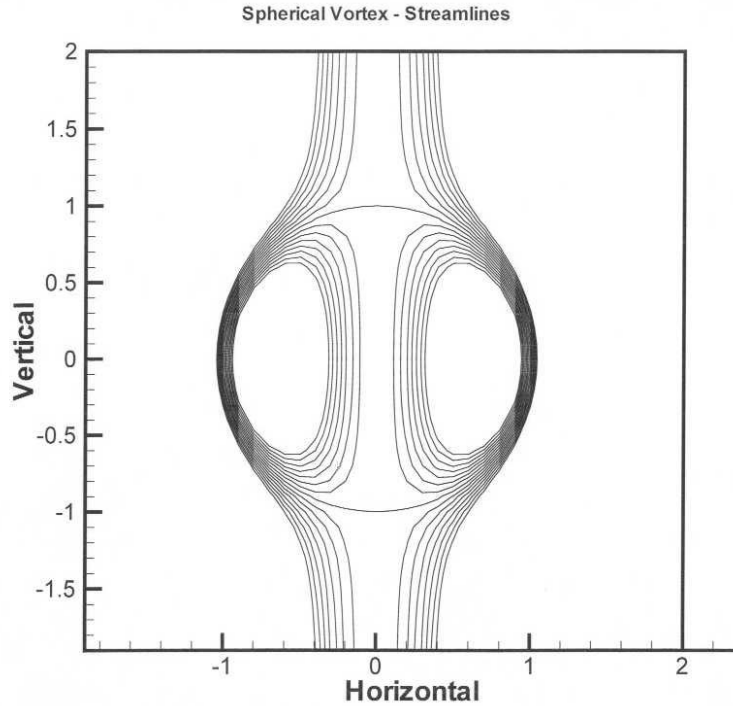


Figure 22. Streamlines of Hill's spherical vortex.

The velocity field induced by this vortex, in terms of vertical component U_z and horizontal component U_r can be described by:

Vertical component:

$$U_z = -W \left[1 + a^3 \frac{1}{2} \frac{r^2 - z^2}{R^5} \right] \quad R > a \quad (3.4.2a)$$

$$U_z = \frac{3W}{2a^2} (a^2 - z^2 - 2r^2) \quad R < a \quad (3.4.2b)$$

Horizontal component:

$$U_r = \frac{3}{2} \frac{W a^3 r z}{R^5} \quad R > a \quad (3.4.3a)$$

$$U_r = \frac{3W r z}{2a^2} \quad R < a \quad (3.4.3b)$$

The velocity field is shown in Figure 23.

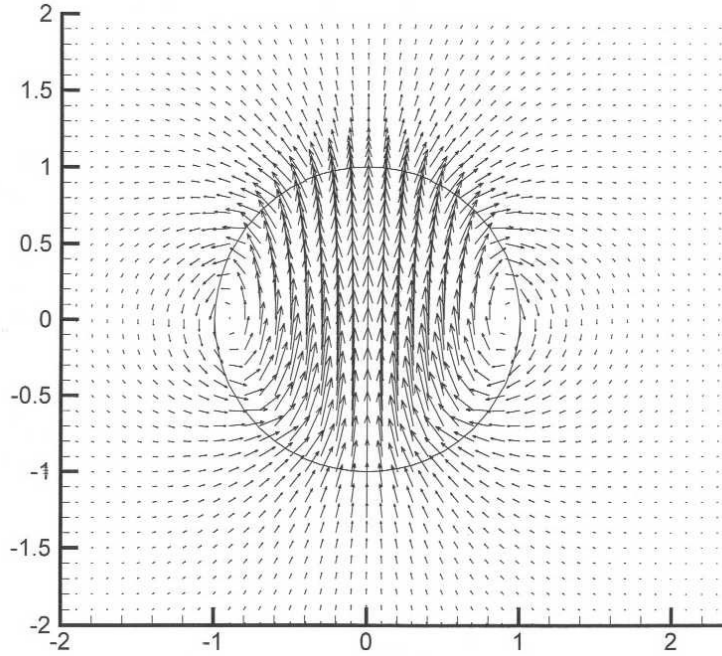


Figure 23. Velocity field of a Hill's spherical vortex.

The strength of the vortex ring is related to vertical velocity of the spherical vortex as:

$$\Gamma = \frac{5}{2} \pi U a \quad (3.4.4)$$

3.4.2.2 Extended Hill's Vortex Model

Comparing Figure 19 and Figure 22, we find that the flow field of a buoyant puff may be simplified by using a Hill's spherical vortex. The buoyant puff generates a vortex ring in the air and its rising motion can be viewed as driven by a vortex ring. The vorticity field in the meridional section is generated due to baroclinic vorticity generation mechanism. Since the gravity is vertical, the chief generation term is the horizontal density difference integrated over the vertical puff extent. Scaling analysis shows that the strength (circulation) of the vortex ring, Γ , follows the relation below:

$$\Gamma \propto \text{Buoyant Velocity} \times \text{Vertical extent} \propto \sqrt{\frac{(\rho_a - \rho_o)}{\rho_a} g} 2R_o \propto \sqrt{2g' V_o} \quad (3.4.5)$$

where: ρ_a and ρ_o are the ambient air density and the initial puff density, respectively, R_o is the initial puff radius, $g' = g \frac{\rho_a - \rho_o}{\rho_a}$ is the reduced gravity, and V_o is the volume of the initial puff. There are many small eddies generated as the puff move upwards, but the motion of the bulk part can be modeled by this large scale vortex ring.

The value of this circulation remains the same even when ambient air is entrained into the puff. Consequently, Hill's spherical vortex is used to model the flow structure inside and outside of the puff by maintaining the circulation. Since the size of a Hill's vortex does not change, in order to incorporate the entrainment process for an expanding buoyant puff, the Hill's vortex concept is extended by assuming the vortex size increases as the puff rises. As an example, a simple but frequently used relation, that the entrainment velocity is linearly proportional to the puff rising velocity, gives:

$$\frac{dR}{dt} = \alpha W \quad (3.4.6)$$

where α is a constant. Denoting R_o and z_o as the initial puff radius and initial puff height, the integration of equation (3.4.6) yields:

$$R = R_o + \alpha(z - z_o) \quad (3.4.7)$$

We assume the size of the extended spherical vortex increases with height as equation (3.4.7) indicates. In this work, we have assumed that the puff is spherical and the initial puff height is the same as the initial puff radius. We assume the relation given by Equation (3.4.7) still holds so that Equation (3.4.6) gives:

$$W = \frac{2 \Gamma}{5\pi [R_o + \alpha(z - z_o)]} \quad (3.4.8)$$

Noticing that the puff radius becomes much larger than the initial puff radius very quickly, equation (3.4.8) simplifies to:

$$W \approx \frac{2 \Gamma}{5\pi \alpha z} \quad (3.4.9)$$

Therefore, as the puff expands, the vortex circulation keeps the same and vertical velocity decreases as the puff rises.

3.4.2.3 The rise of extended Hill's vortex

Very close to the source location, the effect of ambient wind and stratification can be ignored. Then, the height of a buoyant puff is proportional to the square root of the time elapsed.

$$z = \left[\frac{3V_o g'}{2\pi\alpha^3} \right]^{1/4} t^{1/2} = B t^{1/2} \quad (3.4.10)$$

In terms of the puff height, the vertical velocity can be obtained as:

$$W = \frac{dz}{dt} = \frac{1}{2} B t^{-1/2} = \frac{1}{2} \frac{B^2}{z} \quad (3.4.11)$$

Comparing the (3.4.9) and (3.4.10), we have:

$$\Gamma = \frac{5}{4} \sqrt{\frac{3\pi V_o g'}{2\alpha}} \quad (3.4.12)$$

3.5 Particle Deposition

The characterization of particle deposition from a buoyant puff generated from explosive detonations is one of the key elements to successful modeling of the environmental impact of munitions training activities. There are very few field tests that address particle deposition. This is mainly because the initial puff temperature is very high, the time duration is short, the variability is high, and very little understanding of the physical and chemical processes is available. In this work, we will approach this problem via mathematical modeling based on physical understanding as well as available field and laboratory measurements. The quantified results can be used to design future tests and model the emitted pollutants for air quality and ground water quality analysis.

The particulate pollutants emitted from a detonation can be divided into two broad categories based on particle size. The first category includes particles with diameters less than about 50 μm that disperse with gaseous emissions as the buoyant puff evolves in the atmosphere. The second category includes larger particles ($>50\mu\text{m}$) that fall to ground due to gravity. The temporal and spatial deposition pattern of particles is important in estimating how much pollutants in the form of particles are deposited to the ground. Since the particle dropout may change the puff mass loading and the thermal energy content significantly, the deposition process is also important to the estimation of the final puff rise that is a critical parameter in the air quality dispersion modeling,

The larger particles in a buoyant puff are composed of soil particles entrained during detonation, unexploded explosives, and also fragmented shell parts. During the deposition process of these particles, they scavenge pollutants in the puff, absorb heat energy, and may even locally quench the afterburning combustion in the puff. It is important to understand the scavenging effect of the entrained soil. To model these scavenging processes, it is important to know the residence time of a particle inside the hot buoyant puff.

The particle residence time depends on: the particle size and density that determines the gravitational force; the puff buoyancy that determines the uplifting drag force acting on the particles; and the local atmospheric conditions that affect diffusion and also the afterburning chemistry.

3.5.1 Deposition

We will first consider the deposition in the absence of puff buoyancy. A puff produced by the release of detonated materials may consist of a mixture of gases and particles. Larger particles may fall to the ground due to gravitational settling. Smaller particles and gases may deposit on the ground surface due to dry deposition, which is caused by a combination of chemical reaction and physical interception by the ground and vegetation. In the presence of rain, fog, or snow, the pollutant may be removed from the puff and deposited on the ground either by absorption or collection by the water droplets or snowflakes. Sehmel [1984] and Slinn [1984] give thorough reviews of the topics of dry deposition and wet scavenging, respectively. For this project, we considered deposition due solely to gravitational settling.

In the SCM, Stoke's law is used to define the gravitational settling velocity, v_g , as:

$$v_g = \frac{(\rho_s - \rho_a)gD_p^2C}{18\eta} \quad (3.5.1)$$

where, ρ_s is the particle density (g/m^3); ρ_{air} is the air density (g/m^3); g is the gravitational acceleration (9.81 m/s^2); D_p is the particle diameter (m); and η is air viscosity ($1.81 \times 10^{-5} \text{ kg/m/s}$). Since particles entrained in the puff (e.g. soil particles) span a wide size range, Equation 3.5.1 includes the Cunningham correction, C , for small particles given by:

$$C = 1 + \frac{2\lambda}{D_p} \left[a_1 + a_2 \exp \left(-\frac{a_3 D_p}{\lambda} \right) \right] \quad (3.5.2)$$

where λ is the mean free path of air molecules (6.53×10^{-6} cm), and a_1, a_2, a_3 are constants (1.257, 0.40, 0.55, respectively).

3.5.2 Particle Motion in Buoyant Puff

Figure 24 shows a schematic diagram on buoyant puff rise and the particle-laden stem beneath. It is important to know, given particle size and puff buoyancy, when the particles will fall off from the puff.

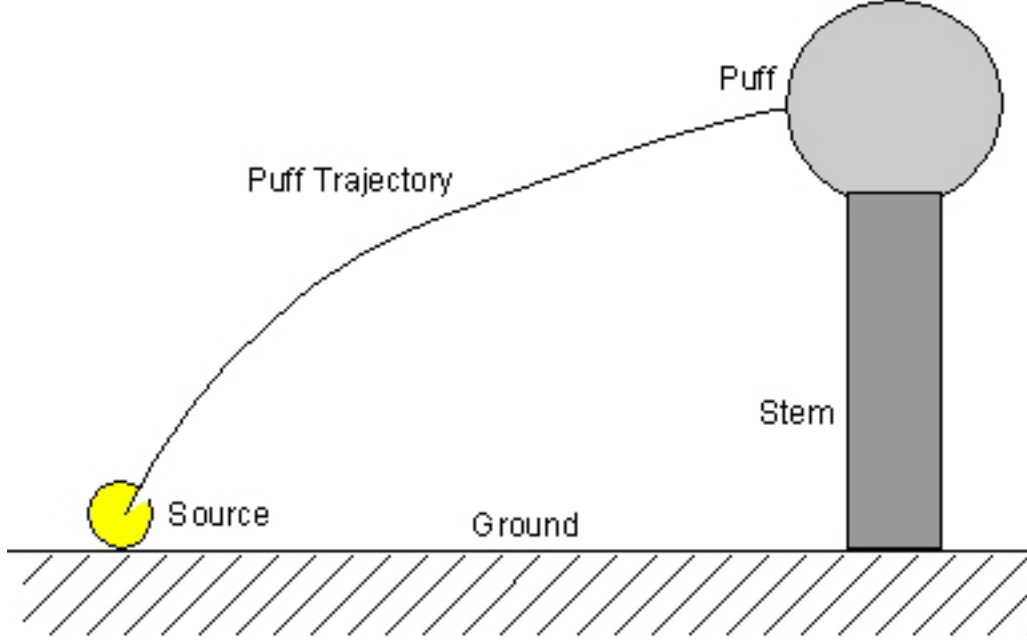


Figure 24. Buoyant puff rise and particle-laden stem formation.

The motion of a particle is governed by its gravity as well as by the drag force due to the ambient air motion. The two components of the governing equations are:

$$\frac{d}{dt}(\rho_s \frac{4\pi}{3} r_p^3 u) = 6\pi\eta r_p (u_f - u) \quad (3.5.3)$$

$$\frac{d}{dt}(\rho_s \frac{4\pi}{3} r_p^3 w) = 6\pi\eta r_p (w_f - w) - \frac{4\pi}{3} r_p^3 (\rho_s - \rho_a) g \quad (3.5.4)$$

where ρ_s is the particle average density, r_p is the radius of the particle, u, w are the horizontal and vertical components of the particle velocity, η is the air viscosity, and u_f and w_f are the horizontal and vertical velocity components of the ambient air flow. Equations (4.2) and (4.3) can be used for u_f and w_f for buoyancy generated large-scale puff motion. These two equations can be simplified to:

$$\frac{du}{dt} = \frac{18\eta}{\rho_s d_p^2} (u_f - u) \quad (3.5.5)$$

$$\frac{dw}{dt} = \frac{18\eta}{\rho_s d_p^2} (w_f - w) - g'' \quad (3.5.6)$$

where d_p is the particle diameter and $g'' = \frac{(\rho_s - \rho_a) g}{\rho_s}$.

As an example, we applied Equations (3.5.5) and (3.5.6) for the deposition of particles from a buoyant puff generated from detonation. The initial puff is released at ground with radius 1 m and density 0.8 kg/m^3 . The ambient air density is 1.2 kg/m^3 with viscosity $1.81 \times 10^{-5} \text{ kg/m/s}$. The density of the soil particles is 2650 kg/m^3 . We assume the entrainment rate has a value of 0.3. The following discussion specifically focuses on larger particles although, as noted above, SCM treats a wide size range including small particles that remain in the puff and are carried downstream without significant fall-out.

Figure 25 shows the rise and fall of particles with diameter $100 \mu\text{m}$ in the buoyant puff. The initial particle cloud has height 2 m and width 10m.

The particle cloud is generated due to the ejection of crater material and to the uplifting of soil particles during the shaking of the ground by the detonation. The whole rise and fall process can be divided into six stages as analyzed below.

Stage 1, around $t = 1$ second, the buoyant puff rises from the dust cloud. Some particles are entrained into the puff moving upward and the rest fall down due to gravity.

Stage 2, around $t = 3$ seconds, the buoyant puff separates from the dust cloud. The number of particles moving up with the puff is more than the number of particles initially inside the puff. This is due to the effect of entrainment. When the puff entrains ambient air, it also entrains the soil particles. At this time, the dust cloud falls to the ground almost completely.

Stage 3, around $t = 10$ seconds, the particle-laden buoyant puff rises. The distribution of particles in the puff is not uniform. Most of the particles are associated with the vortex ring. The kidney shaped puff structure is apparent. This is consistent with the numerical simulation results discussed in Section 3.4.

Stage 4, around $t = 20$ seconds, the particles in the puff start falling. This is when the buoyant puff entrains much ambient air and the flow structure is not strong enough to hold the particles moving with the puff. The long maintained coherent kidney shaped structure starts to change.

Stage 5, around $t = 30$ seconds, a particle-laden stem is formed below the bottom of the buoyant puff and is stretching downwards. At this time, the top part of the stem still rises since it is closer to the vortex flow structure. The lower part falls down due to gravity. We can see that the particles at the vortex ring region at $t=20$ seconds are first stretched forming the lower part of the stem. The particles outside of the vortex ring region at $t=20$ seconds are stretched later forming the top part of the stem.

Stage 6, all the particles have fallen outside of the buoyant puff. The top part of the stem may or may not be attached to the puff. The lower part of the stem is reaching to the ground.

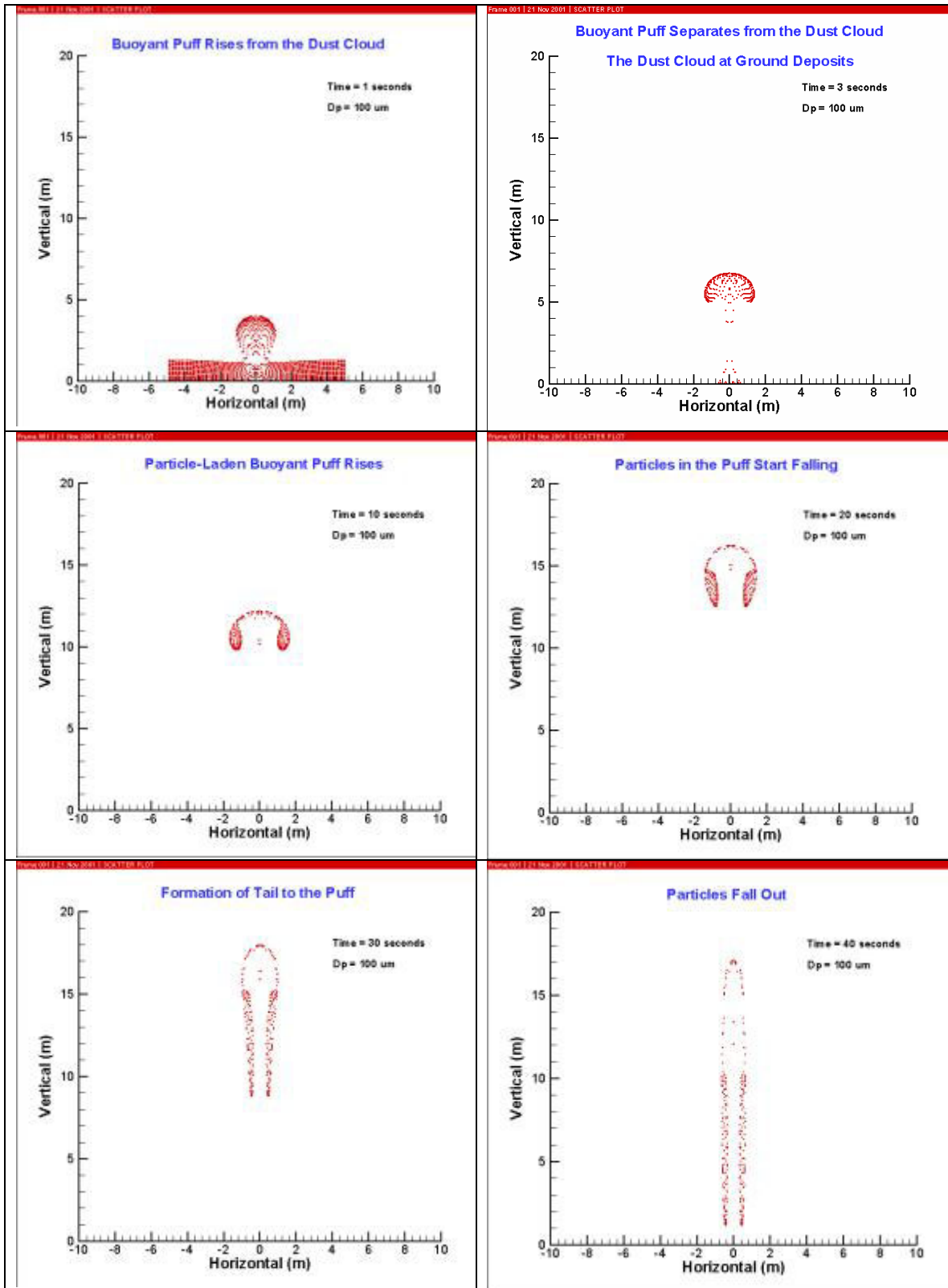


Figure 25. The rise and fall of particles with diameter $100\text{ }\mu\text{m}$.

Figure 26 shows the rise and fall of particles with diameters ranging from $20\mu\text{m}$ to $120\mu\text{m}$. The particles with diameter $20\mu\text{m}$ near the ground are the ones associated with the initial dust cloud. They remain near the ground because of their smaller size and lower gravitational settling velocity as expected from Equation (3.5.1). This has been observed in field observations.

Around $t = 15$ seconds, the main particles in the stem are of size $120\mu\text{m}$. The smaller particles are either in the buoyant puff or near the ground.

Around $t = 30$ seconds, the main particles in the stem are of size $100\mu\text{m}$. The smaller particles are still in the puff and the particles with size $120\mu\text{m}$ have deposited to the ground completely.

Around $t = 45$ seconds, the puff's size keeps increasing because of the entrainment of the ambient air. The particles with size $100\mu\text{m}$ have detached from the buoyant puff. The kidney shaped pattern of particles with size $80\mu\text{m}$ start to deform.

Around $t = 60$ seconds, the particles with size $100\mu\text{m}$ have deposited to the ground completely. The particles with size $80\mu\text{m}$ form the top part of the stem.

Figure 26 indicates that heavier particles fall down quickly and are deposited close to the source location in the absence of wind. The stem is composed of particles with different sizes at different times, heavier particles earlier and lighter particles later.

Figure 27 shows the number of particles in the buoyant puff as a function of time for seven cases with different particle diameter. The number of particles in the initial buoyant puff is about 760 for all cases see Figure 27b. As the buoyant puff rises, it entrains particles into the puff. More light particles are entrained into the puff than heavier particles. The maximum number of $20\mu\text{m}$ particle is about 1000 at about $t = 1.5$ seconds and the maximum number of $140\mu\text{m}$ particles is about 860 at about $t = 0.5$ seconds. See the description of stage 2 on Figure 25. Immediately after the number of particles in the buoyant puff reaches maximum, there is a drop off of the particles from the puff. This is due to the separation of the buoyant puff from the ground based dust cloud.

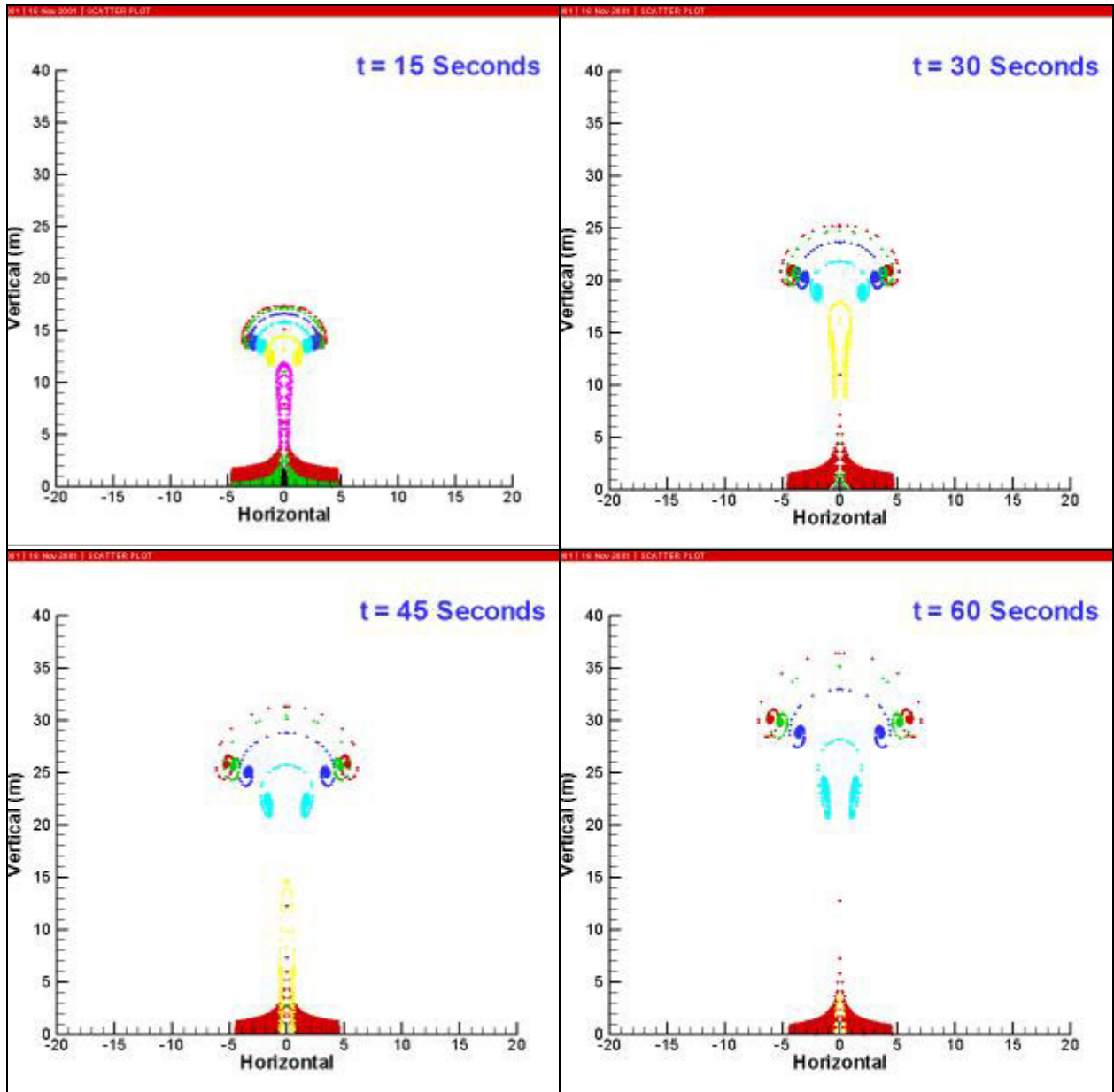


Figure 26. The rise and fall of particles of various diameters in a buoyant puff: red-20μm, green-40μm, blue-60μm, cyan-80 m, yellow-100 m, and purple-120 m.

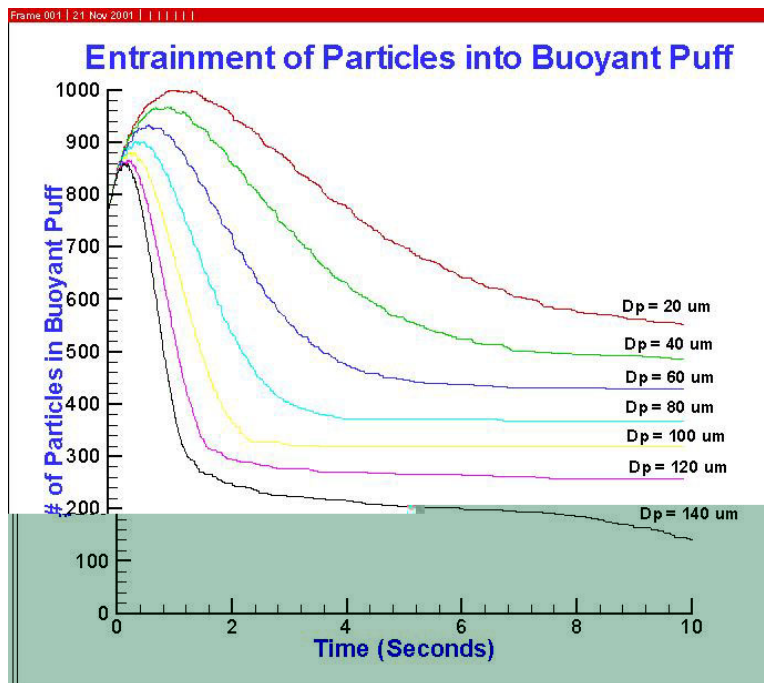
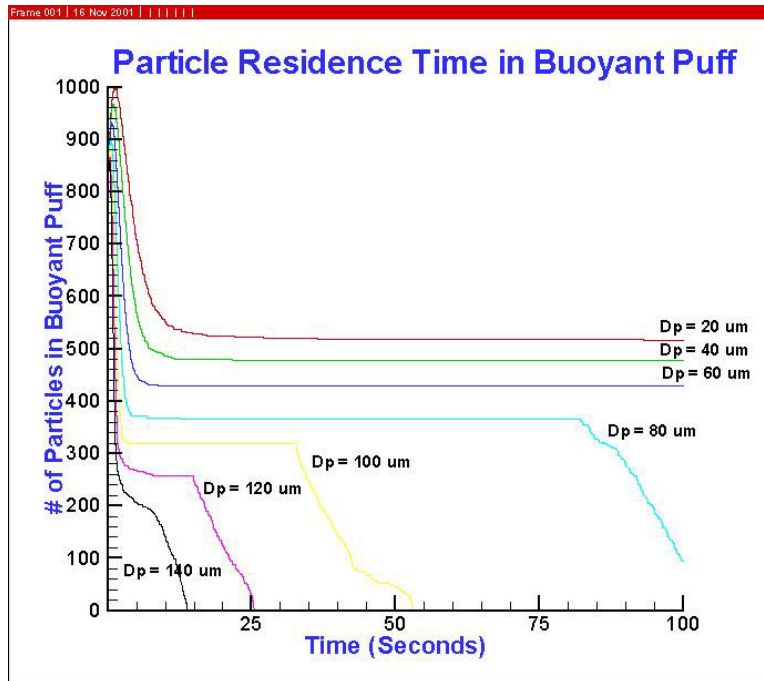


Figure 27. Number of particles in the buoyant puff at different times: (a) for duration up to 100 seconds, (b) for the first 10 seconds.

After the separation, the number of particles in the puff is about 540 for 20 μm particles, 480 for 40 μm particles, and 430 for 60 μm particles, etc. These numbers of particles can be sustained in the puff for a

period of time before they fall off: we call this time the particle residence time. The residence times for smaller particles are longer than 100 seconds. The residence times for 80 μm , 100 μm , and 120 μm particles are about 80 seconds, 32 seconds and 15 seconds, respectively. The 140 μm particles fall off quickly after the separation process. There is not a significant residence time period.

It should be pointed out that the results presented in Figure 25 through 27 are for the example case. The timing of particle fall off depends on the buoyant puff conditions and ambient atmospheric conditions. For the ease of application, we derive the characteristics particle residence time and particle fall off height below. Their applicability awaits the validation by field experimental measurements.

When the buoyant puff rises, the puff material and ambient air exerts an upward drag force to the particle. As the puff rises, it entrains more air and the upward motion slows down. Eventually, the gravitational force on the particle exceeds the drag force and the particle falls down.

At the height that the particle begins to fall, the right hand side of equation (3.5.6) vanishes, and $w = 0$ and $w_f = W$:

$$\frac{18\eta g}{\rho_s d_p^2} = \left(\frac{\rho_s - \rho_a}{\rho_s} \right) g = g'' \quad (3.5.7)$$

Substituting equation (3.4.9) and (3.4.12) into (3.5.7), the particle fallout height is then given by:

$$z_d = \frac{36\eta\Gamma}{5\pi\alpha\rho_s d_p^2 g''} = \frac{9\eta}{\rho_s d_p^2 g''} \sqrt{\frac{3V_o g'}{2\pi\alpha^3}} \quad (3.5.8)$$

and the particle residence time, which characterizes how long a particle stays in the puff, can be obtained from equations (3.4.10) and (3.5.8):

$$t_d = \frac{81\eta^2}{\rho_s^2 d_p^4 g''^2} \sqrt{\frac{3V_o g'}{2\pi\alpha^3}} \quad (3.5.9)$$

Since, in most cases, $\rho_s \gg \rho_a$, $g'' \approx g$, equation (3.5.8) and (3.5.9) can be further simplified to:

$$z_d = \frac{9\eta}{\rho_s d_p^2 g} \sqrt{\frac{3V_o g'}{2\pi\alpha^3}} \quad (3.5.10)$$

$$t_d = \frac{81\eta^2}{\rho_s^2 d_p^4 g^2} \sqrt{\frac{3V_o g'}{2\pi\alpha^3}} \quad (3.5.11)$$

3.5.3 Effect of Particle Fall-off on Buoyant Puff Rise

When heavier particles fall from the buoyant puff (Figure 28), the total mass and heat content of the puff are decreased. These effects may significantly affect the final puff rise. We will formulate a model for the buoyant puff rise with significant particle fall off in this chapter. We assume:

- Atmospheric stratification is not important.
- Ambient wind is not important.
- The buoyant cloud is spherical.
- Soil particles are of same size (to be extended).
- Initial condition: $t=0$, $z=0$, $w=0$

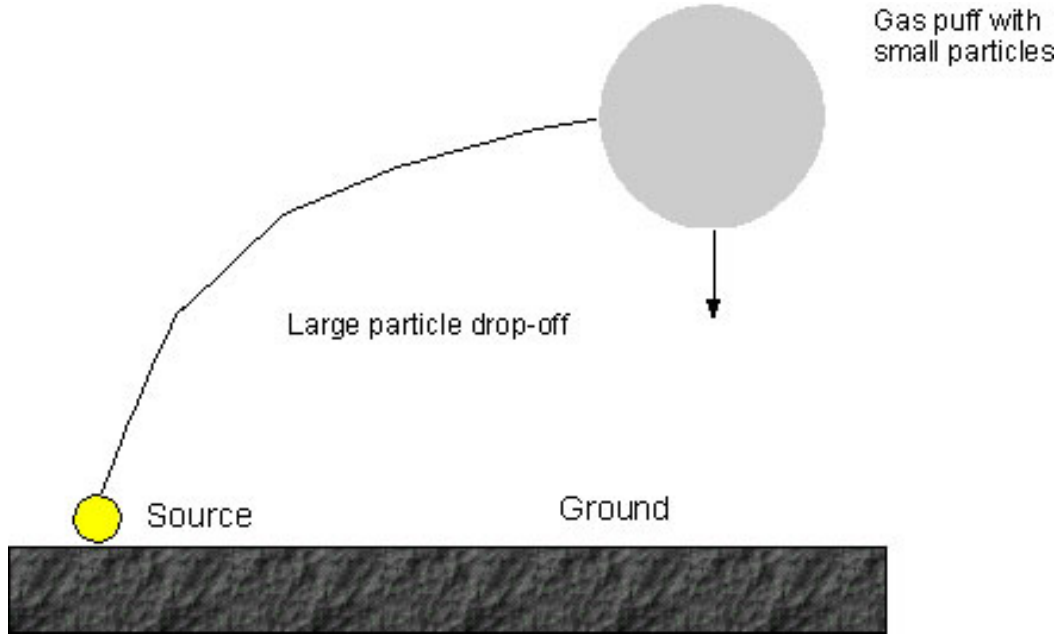


Figure 28. A schematic diagram on the buoyant puff rise and particles fall off.

The mass conservation says that the rate of mass change in the puff is the difference between the rate of air entrained into the air and the rate of particle mass fall out of the puff:

$$\frac{d}{dt}(\rho_p \frac{4\pi}{3} r^3) = 4\pi r^2 \alpha w \rho_a - \rho_d \pi r^2 V_d \quad (3.5.12)$$

where ρ_p is the averaged puff density, r is the puff radius, α is the entrainment rate, w the puff rising velocity, ρ_a is the ambient air density, ρ_d is the mass of particles divided by the puff volume, and V_d is the particle fall off velocity. Assuming there are N_d particles in the puff, denoting ρ_s and r_s as the particle material density and particle radius respectively, by definition, we have:

$$\rho_d \frac{4\pi}{3} r^3 = N_d \rho_s \frac{4\pi}{3} r_s^3 \quad (3.5.13)$$

Newton's second law in the vertical direction states that the rate of change in vertical momentum of the puff is the same as the net force in the vertical direction acting on the puff.

$$\frac{d}{dt}(\rho_p \frac{4\pi}{3} r^3 w) = \frac{4\pi}{3} r^3 g (\rho_a - \rho_p) - \rho_d \pi r^2 (w + V_d) w - 3\pi \eta r_s (w + V_d) N_d / C \quad (3.5.14)$$

On the right hand side of equation (3.5.3), the first term is the buoyant force owing to the fact that the puff density is lower than the ambient air density, the second term is the rate of vertical momentum loss due to the fall out of particles from the puff, the third term is the viscous frictional force acting on the puff due to the downward motion of particles in the puff. C is Cunningham correction factor see equation (3.5.13). Applying Newton's second law to the group of particle, we have:

$$-\frac{d}{dt}(N_d \rho_s \frac{4\pi}{3} r_s^3 V_d) = -N_d \rho_s \frac{4\pi}{3} r_s^3 g + 3\pi \eta r_s (w + V_d) N_d / C \quad (3.5.15)$$

The rate of change in vertical momentum of particles is due to the gravitational force acting on the particles and the frictional drag force. In equations (3.5.3) and (3.5.4), the relative velocity between the upward puff motion and the downward particle motion should be calculated separately for cases particles are inside and outside of the puff as below:

$$w + V_d = \begin{cases} w + V_d, & \text{if } z - z_d < r \\ V_d, & \text{if } z - z_d > r \end{cases} \quad (3.5.16)$$

where z is the height of the buoyant puff center, z_d is the center height of the falling particles, and r is the radius of the buoyant puff. Kinematics relations also hold:

$$\frac{dz}{dt} = w \quad (3.5.17)$$

$$\frac{dz_d}{dt} = -V_d \quad (3.5.18)$$

The last equation is obtained from the law of energy conservation. A similar equation has been derived for the rise and dispersion of reacting puff (Zhang et al, 1997):

$$\frac{d}{dt}(\rho_p \frac{4\pi}{3} r^3 H_p) = H_{\text{Entr}} + H_{\text{React}} + H_{\text{Rad}} + H_{\text{Thermal}} + H_{\text{Ground}} + H_{\text{Depo}} \quad (3.5.19)$$

where:

$$H_p = c_p T_p \quad (3.5.20)$$

is the specific heat of the puff. Equation (3.5.19) states: The rate of enthalpy change in the puff equals to the sum of the following terms:

$$H_{\text{Entr}} = 4\pi r^2 \alpha w c_p T_a \quad (3.5.21)$$

is the entrainment rate of the ambient enthalpy.

H_{React} is the heat generation rate due to chemical reactions. H_{Rad} is the rate of heat loss due to thermal radiation to the surroundings. H_{Thermal} is the rate of heat change due to phase changes. H_{Ground} is the heat transfer from the hot puff to the cold ground when the puff touches the ground.

$$H_{\text{Depo}} = \dot{N}_d \rho_d \frac{4\pi}{3} d^3 c_p T_s \quad (3.5.22)$$

is the gravitational fall out rate of enthalpy associated with particles, where T_s is the mean particle temperature. This temperature can be obtained by considering heat transfer from the hot puff to the cold soil particles.

3.6 Meteorology

Reliable predictions for the puff downwind distance and vertical height as a function of time require solving the ODEs for puff motion in a stratified atmosphere. In the SCM, a meteorology module has been implemented which extracts ambient temperature, pressure, wind speed, wind direction, and relative humidity from user-supplied profiles. The meteorology module also includes algorithms for calculating other measures of atmospheric stability and turbulence including the friction velocity, Monin-Obukhov length, sensible heat flux, and adiabatic lapse rate.

3.6.1 Atmospheric Stratification

The puff rise dynamics depends on the variation of atmospheric properties with altitude. This includes the wind speed, temperature, and relative humidity.

Letting z represent the vertical height in the atmosphere, then the pressure profile is given by::

$$\frac{dp(z)}{dz} = -\rho(z)g \quad (3.6.1)$$

where g is the acceleration due to gravity and the ideal gas density is:

$$\rho(z) = \frac{p(z)M}{RT(z)} \quad (3.6.2)$$

where $p(z)$ is the pressure, $T(z)$ is the temperature, and M is the molecular weight. Assuming the pressure at the ground is known and that the temperature as a function of height is also known for a few points, then the pressure profile can be obtained by combining Equations 3.6.1 and 3.6.2 and integrating:

$$p(z) = p(0)e^{-\frac{Mg}{R} \int_0^z \frac{dz}{T(z)}} \quad (3.6.3)$$

For an air parcel that is expanding adiabatically, the first law of thermodynamics can be used to give:

$$\frac{dT(z)}{dp(z)} = \left[\rho(z) \hat{c}_p \right]^{-1} \quad (3.6.4)$$

where \hat{c}_p is the heat capacity at constant pressure per unit mass. Combining Equations 3.6.1 and 3.6.4 gives the adiabatic lapse rate:

$$\Gamma_{adiabatic} = \left(\frac{dT}{dz} \right)_{adiabatic} = -\frac{g}{\hat{c}_p} \quad (3.6.5)$$

where:

$$\hat{c}_p = \left(1 - \frac{m_{water}}{m_{air}} \right) \hat{c}_{p,air} + \frac{m_{water}}{m_{air}} \hat{c}_{p,water} \quad (3.6.6)$$

and m_{water} and m_{air} are the mass of water vapor and air and $\hat{c}_{p,water}$ and $\hat{c}_{p,air}$ are the constant pressure heat capacities of water and air, respectively. The adiabatic lapse rate is constant for a dry atmosphere and is given by:

$$\Gamma_{dry,adiabatic} = \left(\frac{dT}{dz} \right)_{dry,adiabatic} = -\frac{g}{\hat{c}_{p,air}} = -0.00976 \text{ } ^\circ\text{C}/\text{m} \quad (3.6.7)$$

3.6.2 Atmospheric Stability

The SCM enables the user to specify the atmospheric stability based on the Pasquill stability classes given in Table 8. The approach is useful because the stability classes are a convenient way to define atmospheric stability based on observation. Once specified, the stability parameter then influences the calculation of

other atmospheric properties such as the Friction velocity and Monin-Obukhov parameters discussed in Section 2.4.4.

Table 8. Pasquill Atmospheric Stability Classes

Stability Parameter	Description	Pasquill Stability Class
1	Extremely unstable	A
2	Moderately unstable	B
3	Slightly unstable	C
4	Neutral	D
5	Slightly stable	E
6	Moderately stable	F

3.6.3 Sensible Heat Flux

The sensible heat flux for daytime conditions is given by:

$$H = \left[\frac{1 - \alpha + \gamma/s}{1 + \gamma/s} \right] (Q_{rad} - Q_{ground}) - \beta\gamma \quad (3.6.8)$$

where Q_{rad} and Q_{ground} are the radiative heat flux and ground heat flux, respectively. The parameter α is a surface moisture coefficient. The parameters γ and s are given by:

$$\begin{aligned} \gamma &= C_p \lambda \\ s &= q / T \end{aligned} \quad (3.6.9)$$

where λ is the latent heat of vaporization, C_p is the constant pressure heat capacity, and q is the saturation specific humidity.

$$\gamma/s = 119.56 - 0.7843T + 1.2887 \times 10^{-3} T^2 \quad (3.6.10)$$

The radiation heat flux is given by:

$$Q_{rad} = \frac{(1 - r)R_{sol} + C_1 T^6 - \sigma T^4 + C_2 N_{cloud}}{1 + C_3} \quad (3.6.11)$$

where T is the temperature, r is the surface albedo, σ is the Stefan-Boltzman constant, and R_{sol} is the solar radiation at ground level. The empirical constants C_1 and C_2 are $5.31 \times 10^{-13} \text{ W m}^{-2} \text{ K}^6$ and 60 W m^{-2} , respectively. The constant C_3 is a coefficient for surface and depends on whether the surface is dry or wet. For a dry surface $C_3 = 0.25$ and for a wet surface $C_3 = 0.12$.

The solar radiation at ground level in the absence of cloud cover can be expressed in terms of the solar elevation angle ϕ by:

$$R_{sol} = R_{sol}^\circ = a_2 + a_1 \sin \phi \quad (3.6.12)$$

where the turbidity coefficients a_1 and a_2 are 990 W m^{-2} and -30 W m^{-2} , respectively. When cloud cover is present then the radiation at ground level is reduced from that given in Eq. 2.4.12 and can be expressed as:

$$R_{sol} = R_{sol}^{\circ} [1 - (1 - T_{cloud}) N^{b_2}] \quad (3.6.13)$$

In Equation (3.6.13), T_{cloud} is the cloud transmittance, N_{cloud} is the fraction of cloud cover, and the coefficient $b_2 = 3.4$. T_{cloud} varies by the type of cloud. A simple set of data is $T_{cloud} = 0.61$ for high altitude cirrus type clouds, $T_{cloud} = 0.26$ for medium altitude cumulus type clouds, and $T_{cloud} = 0.17$ for low altitude stratus or nimbostratus clouds.

3.6.4 Friction Velocity and Monin-Obukhov Length

The friction velocity, u^* , and the Monin-Obukhov length, L_{MO} , is related by:

$$L_{MO} = \frac{\rho C_p T u^{*3}}{\kappa g H_{sens}} \quad (3.6.14)$$

where T is the ambient temperature, ρ is the ambient density, C_p is the specific heat, g is the gravitational constant, κ is the von Karman constant, and H is the sensible heat flux. Additionally, the following relations define the friction velocity for neutral, stable, and unstable atmospheric conditions [Seinfeld and Pandis, 1998].

$$\begin{aligned} \frac{\kappa u}{u^*} &= \ln \left(\frac{z}{z_o} \right) \\ \frac{\kappa u}{u^*} &= \ln \left(\frac{z}{z_o} \right) + 5.2\alpha \\ \frac{\kappa u}{u^*} &= 2 \left[\tan^{-1} x - \tan^{-1} x_o \right] + \ln \frac{x-1}{x_o+1} - \ln \frac{x+1}{x_o+1} \\ x &= \left(1 - 15 \frac{z}{L_{MO}} \right)^{1/4} \\ x_o &= \left(1 - 15 \frac{z_o}{L_{MO}} \right)^{1/4} \end{aligned} \quad (3.6.15)$$

where u is the measured wind speed, z is the wind measurement height, z_o is the roughness scale. The parameter α is given by $\alpha = z/L$ when $z < L$ and by $\alpha = 1$ when $z > L$.

3.7 Chemical Kinetics

3.7.1 Phenomenology

Test data indicate that, after detonating or burning energetic materials, chemical reactions continue as the high temperature puff cools with air entrainment. These afterburning reactions influence the eventual chemical composition in the puff and also release heat that enhances the puff buoyancy. The latter increases the final puff rise. The afterburning is a coupled process between chemistry (thermochemical transformation) and physics (turbulent entrainment/mixing) that can be modeled by an operator splitting algorithm.

Semi-volatile organic compounds, polychlorinated dibenzo-p-dioxins and furans, toxic metals, volatile organic compounds, and inorganic gases have been measured in Bang Box tests [Mitchell and Suggs, 1998] and contained detonation and exploding ordnance tests [METDC, 2000; 2001]. Existing models applied thermodynamic equilibrium codes throughout the entrainment process to calculate the emission factors. VOCs were not predicted. The modeling of these products requires the application of a chemical kinetics solver with relevant rate parameter data retrieved from literature, estimated based on available information, or measured in laboratories.

The SCM includes a module to treat gas phase after-burning kinetics and the coupling to the puff flow dynamics by changes in the enthalpy due to chemical reactions. This is a unique aspect of the current model that has been largely lacking in other models for explosive events.

3.7.2 Chemical Kinetic Mechanisms

For HE munitions detonation, the chemical kinetics of particular interest include the gas phase afterburning kinetics of small, unburned hydrocarbons, nitrogen and sulfur oxides and acids, and volatile (VOC) and semi-volatile (SVOC) organic compounds. In addition, the emission of carbonaceous and metal particulates introduces the need to include the heterogeneous uptake kinetics. Lastly, decomposition and oxidation reactions for energetic material such as RDX and HMX have also been included in the database due to the detection of residual energetic material at several DoD sites and the current uncertainty regarding their source.

Chemical kinetic mechanisms were developed by first formulating the reactions needed to describe the chemistry of specific species or sets of specific species and then combining these smaller reaction subsets to formulate the kinetic mechanisms for the more complex systems. The reaction subsets incorporated are shown in Figure 29.

For the evolution of CO, NO_x, and relatively small VOCs rate parameters were adopted based on evaluated kinetic recommendations from the combustion and atmospheric modeling communities [Tsang and Herron, 1991; Baulch et al., 1994; DeMore et al., 1997; Atkinson et al., 1997; Sander et al., 2003] and the electronic NIST chemical kinetic database [Mullard, 1994]. For more complex VOCs, the monographs by Atkinson [1989; 1994], which have compiled key experimental reaction rate constants and mechanisms for the oxidation of a wide range of VOCs and also present methods for estimating key oxidation rate parameters when experimental data are lacking were used. An illustrative example of the kinetic mechanism for CO_x, HO_x, NO_y, NH_x, and small hydrocarbons and is given in Section 7.

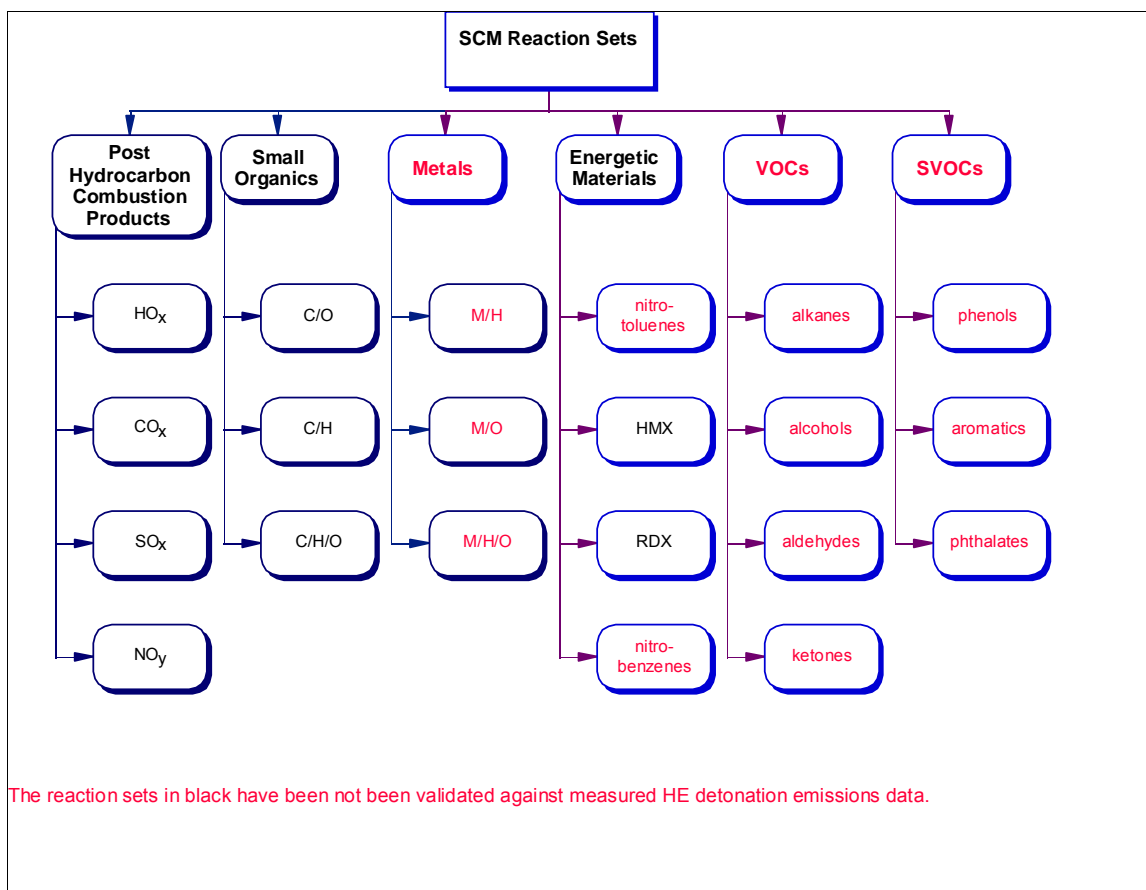


Figure 29. Overview of SCM chemical kinetic reaction sets.

3.7.3 Numerical Model

Through previous and ongoing projects, Aerodyne has developed a chemical kinetics driver, FLOWKIN, based on the CHEMKIN-II [Kee et al., 1989] library for treating finite-rate chemical kinetics in simple flows. This driver is a modified version of SENKIN [Lutz et al., 1991] based kinetic integration routine for gas phase kinetics. FLOWKIN has also been interfaced with ARI computational codes for treating aerosol microphysics [Brown et al, 1996a] enabling a unified treatment of the chemistry for both vapor and condensed phases. The entire chemical package has been integrated with the SCM module for buoyant puff rise. This provides the numerical tools required to treat after burning chemistry in the buoyant puff, as well as include a source term for enthalpy changes due to chemistry that can impact the puff's dynamics.

3.7.4 RDX Half-life

As an example, the SCM chemical kinetic model was used to characterize the half-life of gas phase RDX during the initial puff expansion. The kinetic mechanism is given in Appendix 5. Figure 30 shows selected decomposition and oxidation products. Figure 31 shows the RDX half-life. In general, the half-life is short indicating very little, if any, gas phase RDX is expected to survive the initial adiabatic expansion. These gas phase kinetic calculations, however, do not address the extent to which RDX is released as a component of particulates from low order detonations or quenched out of the fireball by entrained soil particles.

RDX Decomposition and Oxidation in Post-Detonation Gases ($P_o = 100 \text{ atm}$, $T_o = 930.6 \text{ K}$, $V_o = 24.2 \text{ cc g}^{-1}$)

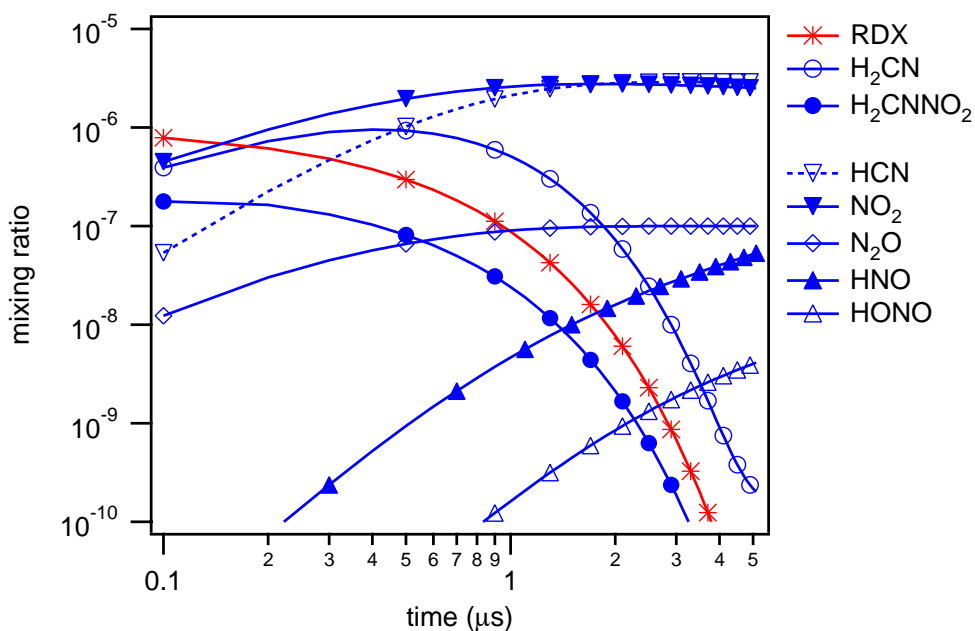


Figure 30. RDX decomposition and oxidation in post-detonation gases

RDX Half-Life in Post-Detonation Gases as a Function of Temperature During Expansion

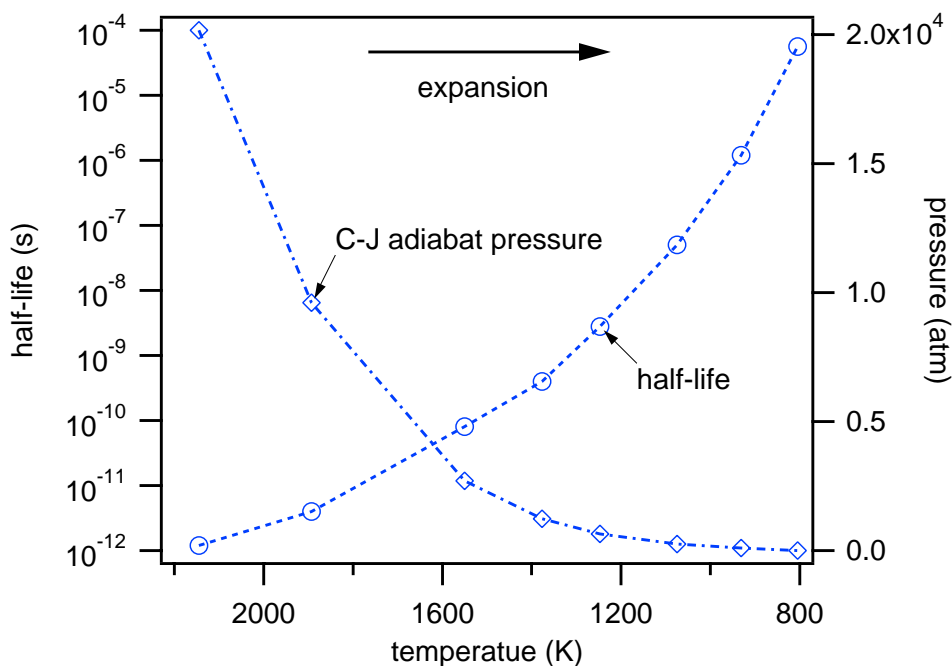


Figure 31. RDX half-life and C-J adiabat pressure as a function of puff temperature.

3.8 Heterogeneous Update Kinetics

3.8.1 Overview

The reacting detonation puff will, in general, contain two types of particles, entrained soil/dust and detonation produced soot, that may interact chemically with the trace gaseous pollutants produced in the detonation of energetic materials and/or in their subsequent afterburning reactions.

Soil and dust particles that are entrained into the detonation fire ball will be processed at very high temperature, with organic soil components largely oxidized or pyrolyzed to soot. The remaining particles will be primarily inorganic oxide, hydroxide and/or carbonate minerals. Typical soil minerals include: SiO_2 , Al_2O_3 , Fe_2O_3 , CaO , CaCO_3 , MgO , TiO_2 and various clays (typically mixtures of Ca, Mg, Al, Fe, Na and K oxides, hydroxides, and/or carbonates.)

Soot is a partially hydrogenated graphitic carbon material with a nominal C/H ratio of ~ 1 . It may also contain minor amounts of oxygen, nitrogen, sulfur, and metallic atoms, depending on the composition of the energetic material (fuel) and the availability of oxidizer (oxygen, nitrogen oxides) during the initial detonation process. Soot may also be coated with a variety of aromatic hydrocarbon compounds, including polycyclic aromatic hydrocarbon (PAH) compounds, especially when it is generated under fuel rich conditions (Sander et al., 2003.)

Gaseous species can be physisorbed or chemisorbed on airborne particles; they can also, in some cases, react directly with the particle's surface material (first order reaction) or an adsorbed species can react with another gaseous species arriving at the particle's surface (second order reaction). The first three processes can be characterized by a simple uptake parameter (γ) that is defined as the probability that a gaseous species striking the particle's surface will either stay adsorbed on the surface or be lost via reaction; with a range of $0 < \gamma \leq 1$ (Sander et al., 2003; Usher et al., 2003a). Under some circumstances even a bimolecular surface process can be characterized by a single uptake coefficient if one reactant is much more abundant than the other, its uptake may be controlled by the γ value for the less abundant species. In general, the heterogeneous uptake processes relevant for the short duration of the reactive detonation puff will be physisorption, chemisorption, or first order reactions, so specification of an uptake coefficient, γ , will be sufficient to describe the heterogeneous kinetics.

3.8.2 Soil Particle Uptake Kinetics

Heterogeneous uptake kinetics on soil dust minerals and mineral compositions has recently been reviewed by Usher et al. (2003). While relatively few laboratory studies aimed at providing mineral aerosol and/or surface uptake parameters have been published, data are available for selected nitrogen oxides, ozone, sulfur dioxide, and selected partially oxygenated organic compounds on a range of individual mineral compounds as well as selected types of soil dust particles. Most studies are based on either Knudsen cell or fast flow reactor techniques. Many studies provide time resolved uptakes that show relatively fast uptake until surface saturation, followed by slower uptake kinetics. Since soil particles entrained through the detonation fireball will tend to be "baked" free of adsorbed surface species, the initial uptake coefficient, γ^0 , provided by the time dependent experiments is deemed to be most representative for detonation puff modeling. Data for individual reactive detonation species is presented below. In general, uptake on very unreactive surfaces like SiO_2 is much less efficient than uptake on more labile surfaces like CaO , CaCO_3 , MgO , or Al_2O_3 . Since the SCM model will, in general, not have a detailed soil chemical analysis to input, a single uptake coefficient, γ^0 , representing a weighted average of available data is recommended for each trace gaseous species. Where data are available for actual soil dust samples the uptake coefficients for those samples have been weighted heavily. Nearly all studies were performed at room temperature (295-298 K), so the results are most appropriate for detonation puff conditions after the initial expanding fireball is cooled and diluted by entrained air. For warmer puffs the room temperature values will likely be too high for physisorption and chemisorption processes, but may underestimate the efficiency of unimolecular surface reactions. Since air entrainment and puff cooling is rapid the recommended γ^0 values should be reasonably accurate for most of the time scale modeled by the SCM.

NO

Mineral surface uptake studies for nitric oxide, NO, have been reported by Hanish and Crowley (2003a) on Saharan dust and Judeikis and Wren (1978) sandy loam, adobe clay and cement. The Hanisch and Crowley study demonstrated that while surface reaction for NO did take place with the co-deposition of significant amounts of ozone, no measurable uptake took place in the absence of ozone. From their data a γ^p of $<1 \times 10^{-5}$ can be estimated. The Judeikis and Wren study measured deposition velocities for NO and NO₂ rather than uptake coefficients, their data are consistent with uptake coefficients on soil for NO in the range of 3 to 8 less than those for NO₂. Based on the $\gamma^p_{\text{NO}_2}$ discussed below, a γ^p_{NO} of 5×10^{-6} is recommended.

NO₂

Relevant nitrogen dioxide uptake kinetics have been reported by Underwood et al. (2001a) and Ullerstam et al. (2003). Knudsen cell studies were performed by Underwood et al. α -Al₂O₃, γ -Al₂O₃, α -Fe₂O₃, γ -Fe₂O₃, TiO₂, MgO, CaO, Saharan sand, and Chinese loess. Lowest γ^p values were recorded for γ -Al₂O₃ (2.2×10^{-8}) and Saharan sand, which is largely SiO₂ (1×10^{-6}). Significantly larger values, in the range of 1.1 to 8.5×10^{-5} were measured for α -Al₂O₃, α -Fe₂O₃, MgO, CaO and Chinese loess, while TiO₂ at 9×10^{-6} and γ -Fe₂O₃ at 4×10^{-6} had intermediate uptake coefficients. Ullerstam et al. measured a small value of 6.3×10^{-7} for Cape Verde dust, which is mostly SiO₂. Based on this wide range of values an estimated weighted mean $\gamma^p_{\text{NO}_2}$ of 2×10^{-5} is recommended, which is about half of the value measured for China loess by Underwood, et al.

HNO₃

Nitric acid vapor uptake studies on mineral surfaces have recently been reported by Underwood et al. (2001a; 2001b) and by Hanisch and Crowley (2001a; 2001b). While their actual laboratory results are in reasonable accord, their data analyses lead to significantly different reported values for $\gamma^p_{\text{HNO}_3}$. The point of controversy is whether the proper surface area accessed by the experiments is the geometrical top surface area of the mineral sample of a much larger surface area estimated with a “pore diffusion” model. This controversy is not new; it has surfaced previously in uptake studies on ice and alkali salt particles (Sander et al., 2003). In general for small molecules with relatively low uptake coefficients, using the top “geometrical” surface area is not correct and corrections for pore diffusion are required. However, HNO₃ vapor tends to have a large uptake coefficient on many surfaces and until the top surface is saturated, very few of its vapor molecules may make it past the top surface.

Based on a pore diffusion analysis, Underwood et al. (2001a) report $\gamma^p_{\text{HNO}_3}$ values that range from 1.1×10^{-3} to 1.6×10^{-2} for on α -Al₂O₃, CaCO₃, MgO, and China loess with the value for basic CaO exceeding the others by roughly an order of magnitude. Underwood et al. (2001b) also report results for several other mineral oxides, Gobi dust and Saharan sand. Values of $\gamma^p_{\text{HNO}_3}$ reported for these samples range from 3.7×10^{-3} to 2.0×10^{-5} . Both Hanisch and Crowley papers analyze their results using geometric surface areas, but demonstrated that $\gamma^p_{\text{HNO}_3}$ values measured on particle of significantly different sizes were consistent using this assumption. They report results for α -Al₂O₃, CaCO₃, Saharan dust, Arizona dust, Chinese dust, and eight clays that range from 0.06 to 0.196. For nitric acid vapor uptake, the analyses of Hanisch and Crowley appear to be more compelling and based on their results a $\gamma^p_{\text{HNO}_3}$ of 0.13 is recommended.

O₃

Ozone uptake coefficients on mineral surfaces have been reported by Hanisch and Crowley (2003b), Michel et al. (2003), and Usher et al. (2003b). Hanisch and Crowley report a mean value of 3.5×10^{-4} for Saharan dust. Michel et al. measured $\gamma^p_{\text{O}_3}$ values for α -Al₂O₃, α -Fe₂O₃, SiO₂, kaolite, China loess, and Saharan sand ranging from 2×10^{-4} to 2.7×10^{-5} ; while Usher et al. of the same lab showed that pre-treating alumina with nitric acid decreased $\gamma^p_{\text{O}_3}$ by 72% while treatment with sulfur dioxide increased $\gamma^p_{\text{O}_3}$ by 33%. They also treated SiO₂ with saturated and unsaturated hydrocarbons, causing its $\gamma^p_{\text{O}_3}$ to decrease 40% and increase 40%, respectively. Based on these data a mean $\gamma^p_{\text{O}_3}$ value of 5×10^{-5} is recommended.

SO₂

Sulfur dioxide uptake on a variety of relevant surfaces have been studied by Ullerstram et al. (2002; 2003), Goodman et al. (2001) and Usher et al. (2002). Ullerstram et al. measured $\gamma_{\text{SO}_2}^p$ values ranging from 4.1×10^{-7} to 4.6×10^{-6} for various Cape Verde dust samples. Usher et al. and Goodman et al. measured $\gamma_{\text{SO}_2}^p$ values for $\alpha\text{-Al}_2\text{O}_3$, CaCO_3 , $\alpha\text{-Fe}_2\text{O}_3$, MgO , TiO_2 , SiO_2 , and China loess ranging from 5.1×10^{-4} (MgO) to $<1 \times 10^{-7}$ (SiO_2). China loess yielded a $\gamma_{\text{SO}_2}^p$ value of $3 (\pm 1) \times 10^{-5}$, matching a recommended mean value of 3×10^{-5} .

VOCs

Li et al. (2001) and Carlos-Cueller et al. (2003) measured uptake coefficients for a variety of partially oxidized volatile organic compounds (VOCs) for a range of representative inorganic mineral oxides. Based on these measurements γ_{VOC}^p values for formaldehyde (8×10^{-5}), acetaldehyde (4×10^{-5}), propionaldehyde (6×10^{-5}), acetone (8×10^{-5}), acetic acid (2×10^{-3}), and methanol (1×10^{-4}) can be recommended. The γ 's for acetic acid and methanol can be used for other light organic acids and alcohols, respectively.

3.8.3 Soot Uptake Kinetics

Heterogeneous uptake kinetics on soot have been recently reviewed by Sander et al. (2003). Uptake on soot usually shows a relatively high initial uptake coefficient followed by a drop off as reactive or absorptive sites saturate. These initial uptake coefficients are most appropriate for fresh detonation soot processed through the fireball.

NO₂

Initial uptake of NO₂ for a variety of fresh soots where measured by Stadler and Rossi (2000) and Alcalá-Jornod et al. (2000) using a novel cylindrical reactor technique operating at room temperature. Initial uptake coefficients on hexane, decane, toluene, and acetylene soot where all measured to be 0.1 or larger. Based on these measurements a $\gamma_{\text{NO}_2}^p$ for soot of 0.1 is recommended.

HNO₃

The uptake of nitric acid vapor was studied by Rogaski et al. (1997) and Choi and Leu (1998) at room temperature. Rogaski et al. measured a $\gamma_{\text{HNO}_3}^p$ of 0.038 for Degussa FW2 soot, while Choi and Leu obtained $\gamma_{\text{HNO}_3}^p$ values of 0.060, 0.023, and 0.067 on kerosene, hexane, and Degussa FW2 soots, respectively. Based on these results a mean $\gamma_{\text{HNO}_3}^p$ of 0.05 is recommended

O₃

The uptake of ozone on soot displays a high initial uptake rate, followed by a rapid drop off to a much lower steady state rate (Longfellow et al., 2000; Sanders et al., 2003). Knudsen cell studies with good time resolution have shown that the initial $\gamma_{\text{O}_3}^p$ can be as large as 1×10^{-3} (Rogaski et al., 1997, Stephens et al., 1986). A $\gamma_{\text{O}_3}^p$ of 1×10^{-3} is recommended.

SO₂

The uptake of sulfur dioxide on soot surfaces has been reported by Rogaski et al. (1997 and Koehler et al. (1999). The former reported a $\gamma_{\text{SO}_2}^p$ of 3×10^{-3} , while the latter report a value of 2×10^{-3} . A value of 2.5×10^{-3} is recommended.

NH₃

Muenter and Koehn
temperature and sa

VOCs

No studies of the u
and related black c
oxidized and arom
organic acids, alde

3.8.4 Summary

The available scien
pollutants with soi
been assessed to de
detonation polluta
updated as addition

3.9 Energetic M

Measurements hav
For high order deto
energetic material
thermal decompos
residual energetic
estimates for the p
required.

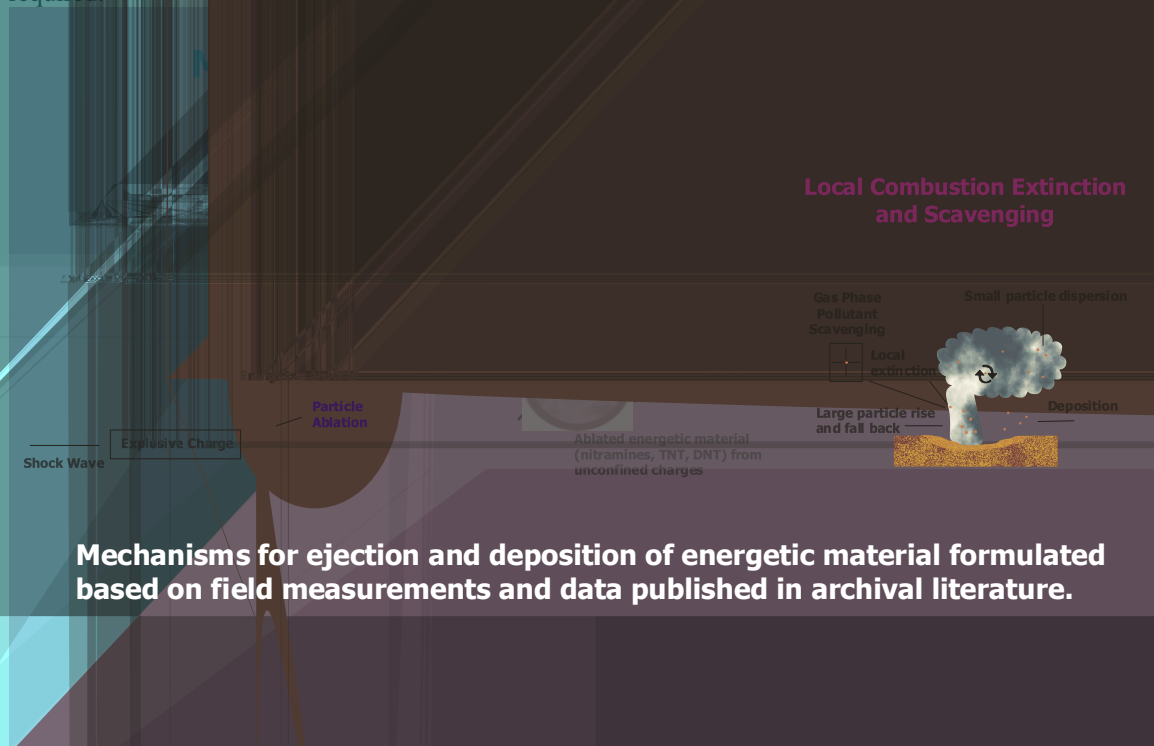


Figure 32. Graphical Representation of Mechanisms for the Ejection and Deposition of Energetic Material in HE Detonations.

There are several potential mechanisms for the release of small amounts of residue emissions including: ablation, ablation and local combustion extinction on casing fragments, and combustion extinction associated with particle scavenging of entrained material. These mechanisms are depicted graphically in Figure 32. Surface ablation of energetic molecules and molecular clusters has been demonstrated in laboratory studies of shock detonation of common energetic materials [Blais et al., 1997; Engelke et al., 2001].

However, modeling these energetic material ejection and/or combustion extinction processes reliably is exceedingly difficult. Consequently, the SCM treats energetic residue emissions using a data-driven model based on the experimental data from recent field measurements [Pennington, 2002; Hewitt, 2003]. Many of these tests utilize the systematic approach developed by Jenkins and co-workers[2000a, 2000b, 2001] which relies on a fresh snow surface as a collection medium. Available field test data are listed in Tables 9 and 10 for live-fire and blow-in-place detonations respectively.

Table 9. Average RDX and TNT mass deposited from live-fire detonations

Munitions	Detonation	Main Charge	Average Mass Deposited (µg)	
			RDX	TNT
60-mm mortar	live-fire	Comp B	74	18
40-mm rifle grenade	live-fire	Comp B	1608	5.2
M67 hand grenade	live-fire	Comp B	25	ND
81-mm mortar	live-fire	Comp B	8500	1100
120-mm mortar	live-fire	Comp B	4200	320
105-mm howitzer	live-fire	Comp B	95	170

Table 10. Average RDX and TNT mass deposited from blow-in-place detonations

Munitions	Detonation	Main Charge	Average Mass Deposited (µg)	
			RDX	TNT
C4 demolition charge	blow-in-place	C4	15	not reported
81-mm mortar/C4	blow-in-place	Comp B	14	0.081
M15 anti-tank/C4	blow-in-place	Comp B	40	0.076
M19 anti-tank/C4	blow-in-place	Comp B	2.7	ND
155-mm howitzer/C4	blow-in-place	TNT	not reported	7889
PMA-1A mine	blow-in-place	TNT	not reported	690
PPM2 mine	blow-in-place	TNT	1.2	276
PPM2 mine w/C4	blow-in-place	TNT	48.5	4500
VS50 mine w/C4	blow-in-place	RDX	135	not reported

As noted, released energetic material from misfired munitions is an important source of range contamination. Table 10 above shows the estimated mean mass of RDX and TNT released with blow-in-place detonations from recent field measurements. These data were generally acquired by attaching a small charge to a test munition and blowing-it-in place and are not from misfires. Further, some of the measured energetic material residues may be due to the detonation charge, and not the test article. Consequently, the results should be taken to as indicative, not completely descriptive, of the energetic material residues created by low order detonations.

To implement the energetic material model, mean mass deposited per mass of explosive for given munitions were collected from reported data for various munitions. The deposited mass is associated by the experiments with given munitions and type of detonation, e.g. impact, blow-in-place, or proximity. Additionally, the average values for different munitions with the same primary explosive charge were adopted to provide one method of estimation for munitions that contain the same primary charge but whose energetic residue emissions have not been explicitly studied.

In practice for high-order detonations, the reported mass deposited is scaled by the tested explosive mass to provide mass deposited/explosive mass. The latter is then multiplied by the explosive mass for the munitions under consideration to estimate the mass of energetic residual material resulting from a detonation. For multiple test items, the explosive mass per item and the total number of items are utilized to estimate the deposited mass of residual energetic material:

$$M_{\text{deposited}} = \sum_i N_{\text{items},i} M_{\text{explosive},i} \left[\frac{M_{\text{reported},i}}{M_{\text{TestExplosive},i}} \right] \quad (3.9.1)$$

The summation in Equation (3.9.1) is over different types of munitions. Recent field studies clearly indicate that high-order detonations do not create enough energetic material residues to explain the degree of contamination found on military firing ranges. Recent studies have further shown that low-order detonations caused by misfired munitions create many orders of magnitude higher energetic material residues.

Even though only a few percent or less of munitions firings will be subject to low order detonations, much higher residues from these munitions will probably dominate the rates of range contamination. Thus, Equation (3.9.1) must be modified to represent both the lower level of contamination per shot from high-order detonations and the higher level of contamination from the smaller number of low order detonations:

$$M_{\text{dep}} = \sum_i N_{\text{items},i} M_{\text{exp},i} \left[(1 - P_{\text{low-order},i}) \left[\frac{M_{\text{high,reported},i}}{M_{\text{TestExplosive},i}} \right] + P_{\text{low-order},i} \left[\frac{M_{\text{low,reported},i}}{M_{\text{TestExplosive},i}} \right] \right] \quad (3.9.2)$$

In order to use Equation (3.9.2) to predict range energetic material contamination for a series of firings, a knowledge of the mean residue levels both of the mean high and low-order detonations for each energetic material in munitions type is required, along with an estimate of the fraction of munitions expected to produce a low-order detonation. The usefulness of Equation (3.9.2) relies on continued efforts to develop data of the sort displayed in Tables 9 and 10 for as wide range of munitions as possible and access to that data through available databases such as the USAEC database discussed below in Section 4.0.

4.0 Army Range and Munitions Environmental Data (ARMED)

ARMED is an Oracle database system developed to support the collection, accessibility, and management of emissions data gathered from the munitions testing. ARMED currently stores emissions data provided from munitions testing conducted at Aberdeen Test Center (ATC), Aberdeen Proving Ground, MD and West Desert Test Center, Dugway Proving Ground (DPG), UT.

The ARMED project consists of two phases. Phase I consists of a Microsoft Access script used to automatically upload data from Microsoft Excel spreadsheets into a central Oracle database. Munitions data is documented on a standardized Microsoft Excel template by ATC and DPG. Personnel at the U.S. Army Environmental Center (USAEC) Acquisition and Technology Division (AT) maintain the template. Once the data goes through an initial quality assurance/quality control (QA/QC) process, it is uploaded into the Oracle Database by way of the Microsoft Access script. Any recognized errors are identified by the automated script and relayed back to the upload administrator. These errors are then fixed and the upload process begins again until all the data is uploaded successfully. The requirements identified for Phase I of ARMED were identified through interviews, requirements gathering use case analysis, and meetings with functional and technical leads. There is no set practice as to how data is input into the template. The test center users have been given the ability to add new information, such as property values, weapon detonators, etc., as needed. This decision was made to expedite the data collection process for the test center so that the user would be able to add information on an as needed basis without first having to

contact a system administrator. It is expected that the systems analyst will make changes that would be needed to accommodate test center user additions for the upload tool to function and succeed.

Phase II will allow ARMED stakeholders to access the data maintained in the system using a web based application.

4.1 Phase I Business Practice

The current ARMED business process for Phase I is illustrated below in workflow/swim lane format.

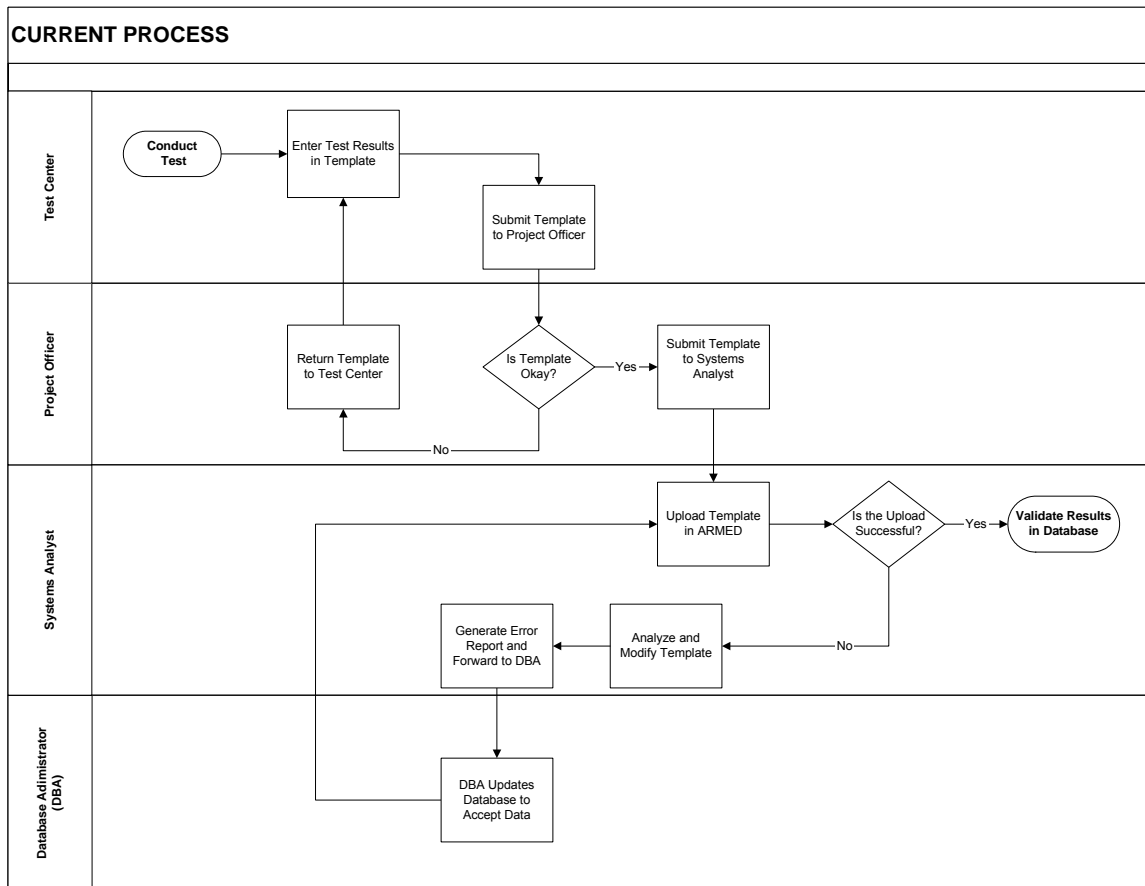


Figure 33. ARMED Phase I Business Process

The ARMED system functionality is illustrated below in context diagram format.

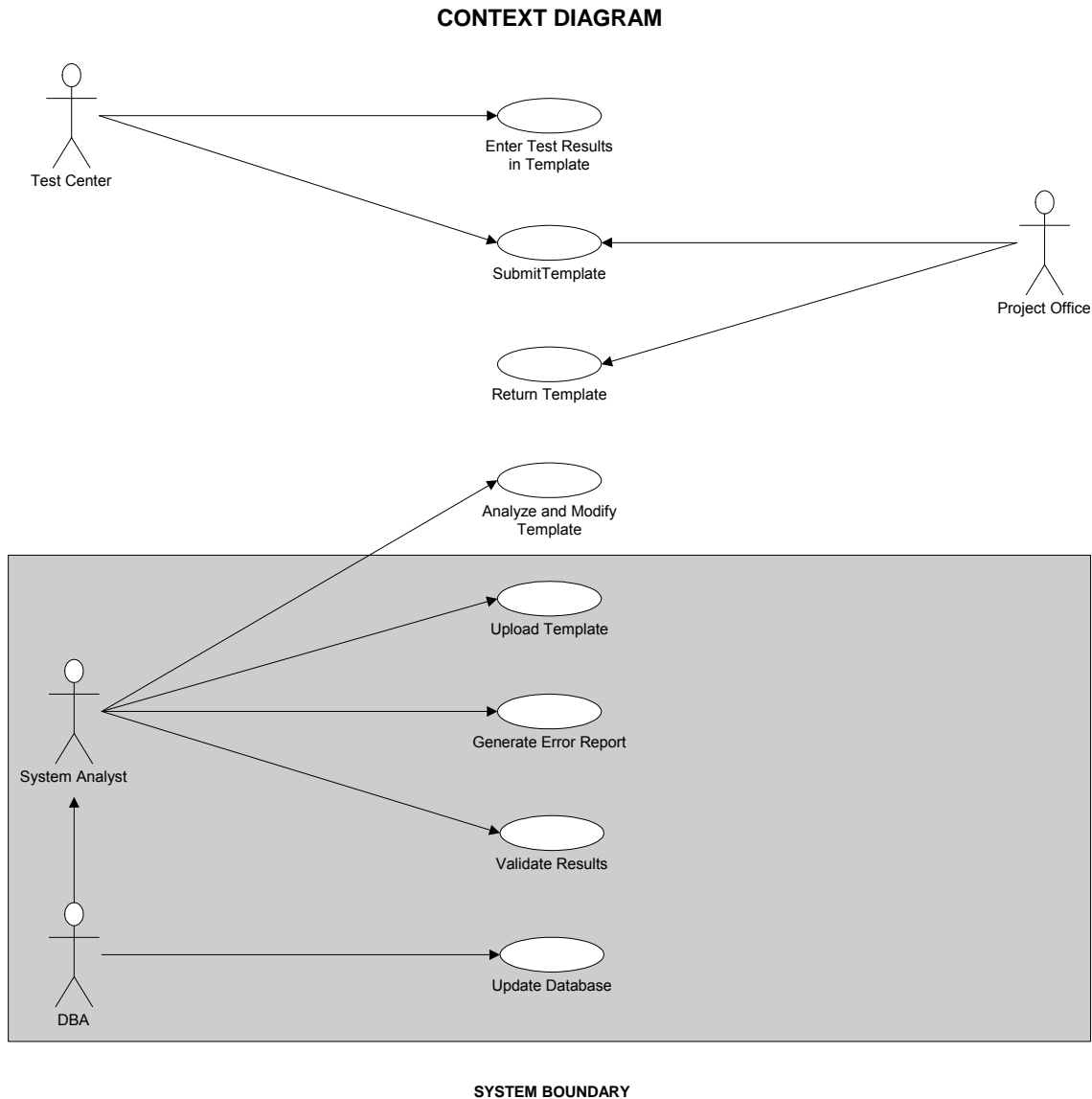


Figure 34. The ARMED system functionality.

4.2 User Characteristics

The user characteristics for this system, as displayed in the above diagram, shall adhere to the following:

- Test Center – Users shall have the ability to read, write, and submit data via a standardized template.
- Project Officer – Users shall have the ability to read and write data in the standardized template.
- Systems Analyst – Users shall have the ability to read and write data in the standardized template as well as make modifications to template elements and drop-down lists.
- System Administrator – Users shall have the ability to read and write data in the standardized template as well as the ability to modify the database tables to accommodate new elements.

In addition to the specific user characteristics listed above, there will be a stakeholder end user. This user will be able to view the data stored in the database and generate pre-defined reports for convenience in analyzing data.

4.3 Data Collection

Phase I is an ongoing process to successfully upload emissions data from over 200 tested munitions. To date, the Army has successfully tested and collected data for over 140 different types of munitions commonly used in training activities. Munition items are tactically fired in a closed facility to capture the airborne emissions generated. The emissions data is collected using state of the art sampling techniques. In order to ensure defensible data for the Army's future use, munition emissions are collected in accordance with U.S. Environmental Protection Agency (EPA) approved Detailed Test Plans. During each test, over 280 chemical species and particulates are monitored to determine if they are present, and in what quantities, when weapons are functioned. All of this information will be accessible to users/stakeholders during Phase II of the project, which is scheduled for testing during the spring of 2004.

4.4 Data Searching and Viewing

Upon logging into ARMED, users will be able to search for emission data using four filters. The user can search for data based on:

- 1) the Department of Defense Identification Code (DoDIC);
- 2) the weapon;
- 3) a specific chemical compound; and/or
- 4) the nomenclature.

Also, the user has the ability to run pre-defined reports and export data to a Microsoft Excel spreadsheet. ARMED currently contains three pre-defined reports, from which the user can apply runtime parameters. These parameters are listed in the footer of the report. The reports are listed below:

- Emissions Factors/Compound Report - This report lists the emission factors for the user-selected compound. The report shows the DODIC, nomenclature and emission factors as the Average Adjusted Emission Factor, lb/item and Average Adjusted Emission Factor, lb/lb Net Explosive Weight (NEW). Information is derived from data stored in the database.
- Sampling and Analysis Methods Report - This report lists the sampling and analysis methods used to obtain emission factor data for the user-selected test. These methods have been submitted to the U.S. Environmental Protection Agency (EPA) prior to each test for approval. A more detailed description for each of these methods is available upon request from USAEC.
- Parameter/Compound List Report - This report lists all of the compounds that each munition has been tested for as potential emission factors to date. The report groups all of the compounds by parameter type.

4.5 Conclusion

The data contained in ARMED has undergone an extensive QA/QC process to ensure complete data integrity. USAEC anticipates going live with Phase II of the database for the summer of 2004, so that the emission factor information will be accessible to users and stakeholders via the web. The munition items that have not been tested at the Test Centers will have relevant data accessible using the Source Characterization Model.

5.0 Model Validation

5.1 Overview of Measurement Data

5.1.1 Nevada Test Site Emissions Characterization

This dataset set include results from four experiments that were performed at the Department of Energy's Nevada Test Site (NTS) [Watkins *et al.* 1998; Velsko *et al.* 1999]. Tests at the NTS were performed for the M107, high explosive (Composition B) 155-mm projectiles. Four detonations were conducted between December 1996 and March 1997. The four tests included the simultaneous detonation of 6, 24, 24, and 60 projectiles. An additional 3 detonations were performed between July and August 1999. Each of these tests was for the detonation of 24 projectiles. Two of these latter tests consisted of the 24 projectile detonations in 1997 to determine experiment reproducibility. The third test changed the orientation of the projectiles from the horizontal to the vertical. Measurements inside the chamber included pressures, temperatures, relative humidity, and gas concentrations. In addition, grab samples were collected for gas, organic, metal and particulate analyses. A general description of the results of these measurements has been presented by Velsko *et al.* [1999] and is summarized below.

- CO₂ and NO showed peaks shortly after detonation and slowly decreased in concentration thereafter while CO changes concentration in the chamber due to detonation but then remains at a constant volume fraction of the chamber gases. The CO₂ concentrations indicated incomplete combustion. For the four detonations in 1997, the overall conversion of the explosive carbon to gas products ranged from 85-94%.
- For volatile organic compounds (VOCs), the emissions of EPA regulated materials were found to be present in trace levels of < 10 ppmv.
- The total suspended particulate (TSP) levels were in the range of hundreds of mg/m³. The size fraction < 10 microns (PM₁₀) was in the range of tens of mg/m³.
- The only energetic material detected in these tests was 41 mg RDX / kg residue for the test in 1997 using 6 projectiles.

5.1.2 Aberdeen Test Center

USAEC funded the U.S. Army Aberdeen Test Center (ATC), Aberdeen Proving Ground (APG) Maryland, to develop the Exploding Ordnance Emission Study, Phase II [METDC, 2000]. The goal of this study is to identify and quantify the emissions resulting from detonation of ordnance currently fielded by the U.S. Army. The Series I tests have been completed and the results have been summarized in a draft report [METDC, 2001]. The test items included (1) a 1/4-pound demolition charge consisting of trinitrotoluene (TNT), (2) a demolition block of military dynamite (M591), (3) a block demolition charge consisting of Composition C4 (M112), (4) a fragmentation hand grenade (M67), and (5) a 66-mm antitank rocket (M72A2). An electric blasting cap (M6) is used to initiate the high explosives although the blasting cap itself is not a test item.

The list of emission measurement target analytes for the test ordnances in Table 1 is extensive. In addition to the gases carbon monoxide (CO), carbon dioxide (CO₂), sulfur dioxide (SO₂), ammonia (NH₃), and nitrogen oxides (NO, NO₂), it includes inorganic acids, hydrocarbons, aldehydes, polyaromatic hydrocarbons (PAHs), volatile organic compounds (VOCs), semivolatile organic compounds (SVOCs), dioxins/furans, energetic materials, and metals. A complete list of the emission measurement targets is given in Table 2.3.3 of the test plan [METDC, 2000].

5.1.3 Dugway Proving Ground

USAEC sponsored a 6 phase series of tests utilizing the BangBox at DPG to quantify the emission products produced when training munitions are used in their tactical configurations [Radian International, 2003]. Phase I characterized airborne emissions for eight simulator and pyrotechnic munitions. Phase II considered 6 additional ordnance items. Phase III studied smoke grenades. Phase IV characterized the airborne emissions of 4 exploding ordnance items.

The analysis of these tests using the SCM treated the munitions studied in Phase IV and included the following:

- M031 Demolition block 1/2lb TNT
- M456 Detonating cord PETN type 1
- ML09 Flexible Linear Shaped Charge 20 g/ft
- ML15 Flexible linear Shaped Charge 225 g/ft

In summary, CO and CO₂ were the primary gas phase compounds emitted. TSP was the primary regulated compound emitted from all items. The highest emissions were from the linear shaped charges. Higher levels of RDX, HCN, NH₃, formaldehyde, and CO indicated less than complete combustion for the linear shaped charges. Airborne metals were also emitted. There was no indication of dioxins/furans for the TNT demolition block or the detonation cord. Low levels of dioxins/furans were reported for some samples from the linear shaped charges. Most of the organic compounds measured were light hydrocarbons (ethylene and acetylene). Most of the organic regulated compounds were VOCs, reported at 1 to 2 orders of magnitude higher than the SVOC.

5.2 Aberdeen Test Center Exploding Ordnance Emissions Study (EOES)- Series I, Phase II

5.2.1 EOES Test Data

Table 9 summarizes the test items. The NTS experiments treated the M107 155-mm rocket with Composition B and included the detonation of 6, 24, 24, and 60 projectiles. The USAEC test items included (1) a 1/4-pound demolition charge consisting of trinitrotoluene (TNT), (2) a demolition block of military dynamite (M591), (3) a block demolition charge consisting of Composition C4 (M112), (4) a fragmentation hand grenade (M67), and (5) a 66-mm antitank rocket (M72A3). An electric blasting cap (M6) was used to initiate the high explosives although the blasting cap itself is not a test item.

Table 9: Summary of USAEC/ATC Exploding Ordnance Emission Studies - Series I Test Items

	USAEC					NTS
Ordnance	M030	M591	M112	M72A2	M67 ^a	M107
Type	Demolition charge	Demolition charge	Demolition charge	66-mm rocket	Grenade	155-mm rocket
PEP	TNT	Dynamite	Composition C4	Octal	Composition B	Composition B
PEP weight (lbs)	0.25	0.37	1.25	0.67	0.41	15.4
Rounds	1	1	1	1	1	6, 24, and 60
PEP composition						
TNT	100.00%	15.00%	0.00%	30.00%	39.00%	36.00%
RDX	0.00%	73.00%	91.00%	0.00%	60.00%	63.00%
HMX	0.00%	0.00%	0.00%	70.00%	0.00%	0.00%
polyisobutylene		0.15%	2.25%			
mineral oil		1.68%	1.31%			
Lubrizol		0.16%	0.13%			
dioctyl sebacate			5.31%			
guar gum		5.00%				
other		0.01%				
Detonation	M6 blasting cap	M6 blasting cap	M6 blasting cap	M6 blasting cap	M213 fuse	RP1

a. Detonator assembly constituents not listed

The test for the M67 grenade and M107 155-mm rocket are of particular interest because Composition B was the explosive in both cases. Consequently, two data sets for Composition B are available for evaluating the results of the Source Characterization Model (SCM).

Table 10 lists a portion of the emission factors determined under the Exploding Ordnance Emission Study, Phase II. It is largely limited to the major emissions listed in Table 1.1-1 of the preliminary data report [METDC, 2001] with a few minor exceptions. The emission factors are reported as the average adjusted emission factor in units of lb of analyte per lb of net explosive weight (NEW). As noted in the summary for the test plan, there were two trials with one detonation per trial for each test item. The emission factors in Table 2 are the average for the two trials and have been adjusted for background levels and losses due to the lack of containment. The water, nitrogen, and hydrogen emissions were not directly measured. In addition, no data was reported for graphitic carbon. Also notable are the reported levels for energetic material including RDX for all test items.

Table 10: Average Adjusted Emission Factor from Exploding Ordnance Emission Study, Phase II

	M030	M591	M112	M67	M72A3
Permanent Gases and Cyanide					
CO ₂	1.390	0.464	0.604	0.517	0.535
CO	2.03E-02	7.96E-03	2.00E-02	4.07E-02	7.41E-02
NO _x	5.83E-03	2.30E-03	4.03E-03	1.57E-03	4.71E-03
HNO ₃	1.46E-04	1.25E-04	1.06E-03	6.12E-05	ND
HCN	5.50E-04	2.18E-04	4.64E-04	1.08E-03	1.38E-04
Particulates					
TSP	6.92E-02	2.33E-02	2.80E-02	9.65E-02	9.43E-02
P ₁₀	5.31E-02	1.42E-02	2.27E-02	8.02E-02	8.27E-02
PM _{2.5}	1.98E-02	5.49E-03	1.67E-02	4.55E-02	4.77E-02
Selected Metals					
Aluminum	1.14E-03	2.26E-04	1.86E-04	7.11E-04	1.67E-03
Barium	6.33E-04	1.67E-05	3.85E-06	1.84E-04	5.42E-04
Chromium	8.04E-04	3.35E-04	4.86E-06	3.74E-04	2.04E-04
Copper	2.31E-05	3.71E-05	1.91E-04	2.95E-05	2.24E-05
Lead	4.97E-04	4.36E-05	8.28E-06	1.54E-04	4.77E-03
Magnesium	5.93E-04	2.39E-04	1.04E-04	1.30E-03	1.85E-03
Manganese	6.94E-05	5.34E-05	1.52E-04	6.25E-05	8.40E-04
Selected Energetics					
2,4-dinitrotoluene	1.55E-06	2.13E-07	ND	ND	2.36E-07
1,3,5-trinitrobenzene	9.90E-06	1.42E-06	1.46E-06	ND	4.01E-07
2,4,6-trinitrotoluene	8.08E-05	1.44E-05	5.38E-07	1.55E-06	1.89E-06
RDX	2.41E-06	2.15E-06	1.58E-06	2.31E-06	2.99E-05
Selected Hydrocarbons					
methane	6.14E-05	3.35E-04	1.25E-03	6.80E-04	8.64E-04
ethylene	2.31E-05	9.84E-03	1.04E-04	5.56E-05	6.85E-05
acetylene	3.63E-05	9.84E-03	4.27E-05	1.87E-05	9.58E-05
Selected Carbonyls					
formaldehyde	7.25E-05	3.12E-05	1.21E-04	8.04E-05	6.36E-05
acetaldehyde	2.82E-05	1.07E-05	7.96E-06	ND	1.73E-05
butyraldehyde	1.21E-04	ND	5.91E-05	1.16E-04	3.36E-05

ND = not detected

5.2.2 Mass Balance

A mass balance analysis was performed for the emissions measured under the EOES. The analysis was limited by the fact that experimental data for water, molecular hydrogen, molecular nitrogen, and particulate carbon were not reported. Consequently, for the present analysis empirical carbon mass balance is reported based on the gas phase emissions that were measured and assuming no particulate carbon, assuming that all PM_{2.5} emissions were carbon particulates, and assuming all total suspended particles (TSP) were carbon particulates. An independent hydrogen mass balance was not performed since water vapor and molecular hydrogen emissions were not reported. Instead, a water emission index was calculated assuming all hydrogen from the explosive was converted to water. This emission factor was then adjusted to give a corrected water emission index by taking into account the hydrogen in HCN and the organics for which emission levels were measured. The corrected emission index for water was then used in the oxygen mass balance. The corrected emission index for water is expected to be high since it assumes no gas phase

molecular hydrogen. An independent nitrogen mass balance was not performed because no data was reported for molecular nitrogen.

Table 11. Carbon and Oxygen Mass Balance for the Exploding Ordnance Emission Study, Phase II.

	M030*			M591			M112		
	theor.	empir.	%	theor.	empir.	%	theor.	empir.	%
carbon	7	7.34	104.9 %	2.84	2.4	85.0 %	3.00	3.7	107.7 %
with PM _{2.5}		7.72	110.3 %		2.5	88.2 %		3.5	118.0 %
with TSP		8.65	123.6 %		2.8	98.4 %		3.2	125.0 %
oxygen	6	17.06	284.3 %	4.64	5.8	124.2 %	6.00	9.3	154.9 %

	M72			M67			M107 (24 projectiles)		
	theor.	empir.	%	%	%	%	%	%	%
carbon	5.1	4.1	79.5 %	4.63	2.9	63.8 %	4.67	2.68	62.9 %
with PM _{2.5}		5.2	100.8 %		3.8	82.0 %			
with TSP		6.1	121.5 %		4.7	102.4 %			
oxygen	7.4	10.9	148.2 %	5.89	8.4	143.4 %	5.86	7.04	120.1 %

* Excess carbon may be due to high pre-detonation chamber CO₂ from a large number of observers who inspected the chamber prior to the test as this was one of the first tests in the series.

Table 11 summarizes the results of the mass balance analysis. With the exception of TNT, the carbon mass balance, assuming all carbon from the explosive is emitted in gas phase species, ranges from about 80% to 100% (a little over 100% for the M112). This suggests that depending on the test item up to approximately 20% of the carbon may be in particulates. The block demolition charge of TNT (M030) is the most oxygen deficient of the explosives tested and the carbon mass balance falls well below 100% reaching only about 50% assuming that the TSP are composed of carbon. The oxygen mass balance ranges from 112% to 155%. These numbers partly reflect that over estimate for water as discussed. For the most part, however, they are interpreted to reflect afterburning in the test chamber.

5.2.3 Detonation Product Emissions: Kinetic Results

Post-detonation chemical kinetic calculations were performed to compare predicted emission levels for selected species to those reported as part of the EOES data. To make the comparison the measured emission factors were converted to mixing ratios. To make that conversion, as well as to do the kinetic calculations, nominal industrial background levels for trace species were adopted: CO₂ (400 ppmv), CO (4 ppmv), CH₄ (2 ppmv).

A simple treatment of the expansion and entrainment was developed in which the radius of the expanding puff increases proportionally to the time squared. The explosive gas/air mixing ratio was taken to vary linearly between 1 (all explosive gas) to fully mixed out conditions. Various mixing profiles were tested. These results are for a profile in which the change in the mass fraction of explosive varies from 1 at time t_0 fully mixing at time $t_1 = 0.7$ s linearly. In addition, a few parametric calculations were performed for chamber volumes 25% smaller and larger than reported. All these parametric studies sometimes resulted in improvement for some species, but resulted in a poorer comparison to measurement for others than the baseline case.

However, there was one particular important aspect of the calculation that played an important part in improving the correlation between SCM predictions and measurements for NO_x emissions. Specifically, the SCM predictions for NO_x levels were significantly lower than measurements for each of the five test cases. Analysis of the reported NO_x levels related to the amount of nitrogen in a given explosive and the NO_x levels predicted by non-ideal gas equilibrium at detonation suggested that the measured NO_x emission levels might be indicative of an alternate kinetic mechanism. Specifically, reported emission factors for energetics and energetic material byproducts suggest that some energetic material is not consumed during detonation. Energetic material that is ejected, while not fully reduced to primary detonation products, may still experience pressures and temperatures that induce partial decomposition through pyrolysis mechanisms. The pyrolysis of energetic material for the test explosives of interest here would result in higher NO_x levels than would be predicted assuming all of the explosive mass is consumed in the detonation.

Consequently, a pyrolysis model for enhanced NO_x emission was developed that used measured levels for residual energetic material as an additional NO_x source. It was found that this data-driven pyrolysis model had no impact on the other predictions for species emission factors because the reported levels of energetics were relatively small. However, it did increase the levels of NO_x in the isentropically expanded detonation puff prior to further afterburning chemistry. Afterburning chemistry was treated as described previously with initial conditions derived from the non-ideal gas equilibrium with chemical kinetics frozen for temperatures < 2000 K, except that initial NO_x levels were increased based on the proposed pyrolysis mechanism for NO_x enhancement.

Table 12 summarizes the SCM model predictions for each of the test cases relative to reported emission factors from measurement by listing the ratio of calculated-to-measured emission factors for several key species. The predicted to measured ratios of detonation product mixing ratios for the five disparate munitions listed in Table 12 are very encouraging. Ratios for the primary detonation products (CO, CO₂, CH₂O, and NO_x) fall within an order of magnitude and most within a factor of three. Predicted mixing ratio for small alcohols such as ethanol and butanol, as well as 5-6 carbon alkanes are within a factor of 3 to 10 of the measured values. These results support the non-ideal gas equilibrium freeze-out of carbon containing species presented in Section 3.1 as modified by the limited afterburning effects as discussed in Section 3.7. However, calculated mixing ratios for benzene, toluene, naphthalene, xylenes, and alkenes such as 1-butene and isobutene are up to a factor of 100 times smaller than measured levels.

Table 12. Ratio of SCM Predicted to Measured Mixing Ratios for Selected Detonation Products

Species\Test	M030	M591	M112	M72	M67
CO	3.5	2.0	2.9	0.9	2.8
CO ₂	0.4*	0.9	1.2	1.1	0.8
CH ₂ O	1.3	1.6	0.3	0.5	0.2
CH ₄	6.8	2.6	2.3	5.8	0.3
HCN	3.5	4.3	0.4	1.1	9.5
NO _x	0.8	0.8	0.9	1.2	0.9
C ₂ H ₄	9.4	3.1	2.6	4.2	4.1
C ₂ H ₂	1.5	0.4	0.3	0.7	0.2
CH ₃ HCO	0.2	0.1	NA	NA	2.0
Propene	4.2	2.2	2.4	1.8	2.5
Ethanol	0.4	0.2	0.3	0.2	0.2
Butanol	0.35	0.3	0.3	0.1	0.4
Napthalene	0.08	0.05	0.07	0.05	0.09
Pentane	0.4	0.3	0.5	0.4	0.6
Hexane	0.1	0.1	0.3	0.2	0.3
1 butene	0.08	0.06	0.07	0.08	0.06
Isobutene	0.08	0.08	0.05	0.06	0.08
Benzene	0.08	0.06	0.06	0.07	0.07
Toluene	0.01	0.01	0.02	0.01	0.03
m/p/o-xylene	0.01	0.01	0.03	0.02	0.02

5.3 Dugway Proving Ground Ordnance Emissions Characterization – Phase IV

In June 2001 Phase IV-A testing was performed using the BangBox at DPG under a USAEC program to measure the emissions from weapons firing, pyrotechnic devices, and exploding ordnance used as part of range operations. URS provided air sampling and analytical support in this program and the data given in their report [Carson et al, 2003] were used to specify SCM initial conditions and to compare calculated emission factors.

The Phase IV-A test items included a demolition block charge of ½ lb TNT, a PETN detonating cord, and two flexible, linear demolition charges. These test items and their chemical compositions are listed in Table 13 along with some other general data. For each item, the composition given in Table 13 is from Carson et al. [2003] and was calculated based on data listed in the MIDAS database. The composition includes the test item and energetic portions of the blasting cap. These compositions were used to specify initial conditions for the SCM calculations.

Table 13: Summary Items Tested at DPG

	Test Item NEW and Composition			
	M031	M456	ML09	ML15
Type	Charge, Demolition Block	Cord, Detonating	Charge, Demolition, Linear	Charge, Demolition, Linear
Explosive	TNT	PETN	RDX	RDX
NEW (lbs)	0.49	0.49	0.481	0.482
No. items /length	1 item	70 ft	168 ft	15 ft
No. trails	2	2	2	2
Composition	lb/lb NEW			
C	0.371	0.190	0.180	0.180
RDX	4.32E-03	4.23E-03	0.982	9.84
Pb	9.00E-04	9.00E-04	1.85E-03	1.84E_03
HCl	3.80E-05	3.80E-05	7.75E-05	7.73E-05

Emissions measurements were performed at the DPG BangBox test facility consisting of a 15.2m diameter hemisphere. Test items were suspended by a copper wire a distance of 1.5m above the chamber floor. Tracer gas was released in the chamber after item deployment and the chamber was cleaned between tests. Table 14 lists measured emission factors for selected species. The measured carbon was nearly equal to the initial level of carbon based on the compositions in Table 13 for all items except the detonating cord.

The DPG tests were modeled with the SCM using the same approach used to model the ATC tests described in Section 5.2. Table 15 lists the ratio of calculated mixing ratio to the average value calculated from the reported [Carson, 2003] average corrected emission factor.

Table 14: Representative Emission Factors for DPG Tests from Carson et al., 2003.

Pollutant	Average Corrected Emission Factor (lb/lb NEW)			
	M031	M456	ML09	ML15
Particulates				
TSP	3.43E-01	3.80E-01	1.61E+00	5.12E+00
PM ₁₀	1.15E-01	3.40E-01	3.85E-01	7.56E-01
PM _{2.5}	1.31E-02	1.11E-02	1.36E-02	8.09E-02
Metals				
Aluminum	1.14E-02	1.63E-02	5.06E-03	7.70E-03
Antimony	6.54E-05	7.56E-05	9.37E-02	3.00E-01
Copper	3.20E-03	1.33E-03	1.03E-03	4.40E-03
Lead	2.20E-04	7.26E-05	3.49E-01	8.50E-01
Magnesium	8.81E-03	1.02E-02	3.54E-03	7.83E-03
Zinc	1.73E-03	1.78E-03	1.02E-03	5.34E-03
Energetics				
1,3,5-Trinitrobenzene	1.79E-05	4.89E-07	3.02E-06	2.52E-06
RDX	5.08E-07	1.72E-06	2.33E-02	2.09E-02
SVOCs				
Naphthalene	7.61E-06	2.63E-05	2.21E-05	1.79E-05
Phenol	7.73E-06	5.50E-06	2.47E-05	2.64E-05
VOCs				
Ethylene	1.58E-04	1.58E-03	2.10E-03	2.27E-03
Acetylene	1.03E-04	1.18E-03	7.20E-04	5.58E-04
Benzene	7.53E-05	3.33E-04	4.51E-04	5.90E-04
Toluene	4.68E-05	1.88E-04	1.71E-04	3.00E-04
HCN	ND	ND	2.29E-02	6.34E-03
Formaldehyde	1.11E-04	4.56E-04	6.74E-03	2.40E-03
CEM				
CO ₂	1.47E+00	5.10E+00	2.40E-01	4.35E-01
CO	2.50E-02	4.80E-02	1.71E-01	1.84E-01
NO _x	1.69E-02	6.96E-03	4.10E-02	4.54E-02

Table 15: Ratio of SCM Predicted to Measured Mixing Ratios for Selected Detonation Products

Species	M031	M456	ML09	ML15
CO	2.2	2.3	1.9	2.3
CO ₂	1.2	1.4	0.8	1.3
CH ₂ O	0.5	0.4	0.6	0.4
CH ₄	1.9	2.2	1.8	2.1
HCN	----	----	3.1	2.8
NO _x	0.5	0.8	0.7	0.7
C ₂ H ₄	2.7	3.2	2.8	3.1
C ₂ H ₂	0.2	0.5	0.3	0.3
CH ₃ HCO	0.6	0.4	0.5	0.7
Propene	2.6	2.3	2.1	2.1
Ethanol	0.3	0.2	0.2	0.2
Butanol	0.3	0.2	0.3	0.4
Napthalene	0.02	0.03	0.04	0.03
Pentane	0.2	0.1	0.2	0.3
Hexane	0.2	0.2	0.009	0.1
1 butene	0.04	0.04	0.03	0.03
Isobutene	0.03	0.04	0.04	0.03
Benzene	0.04	0.03	0.02	0.02
Toluene	0.01	0.01	0.009	0.01
m/p/o-xylene	0.01	0.01	0.009	0.02

5.4 Field Program to Identify TRI Chemicals

Under the SERDP project CP-1197 entitled "Field Program to Identify TRI Chemicals and Determine Emission Factors from DoD munitions activities [Spicer - Battelle] an instrument package was developed to measure a target list of Toxic Release Inventory (TRI) chemicals required as part of federal facilities reporting requirements under Section 313 of the Environmental Protection Agency's Emergency Planning and Community Right-to-Know Act. Following testing and optimization in the laboratory, the instrument package was to be deployed in a mobile laboratory for field campaigns. Two field campaigns were planned. The first measured point of discharge emissions. The second field campaign measured emissions point of impact explosions. Both field campaigns were conducted at the Aberdeen Test Center at Aberdeen Proving Ground, MD and managed by USAEC.

The point of discharge emissions is not the focus of the SCM and, consequently, will not be discussed here. However, under an additional task, ARI deployed an innovative aerosol mass spectrometer (AMS) instrument to support those field studies by measuring the non-refractory chemical composition of fine particles from firing point muzzle exhaust plumes. Muzzle exhaust plumes contained in the Aberdeen Test Center's (ATC) point-of-discharge test chamber were sampled for about 20 minutes after the firing of the each munition. The non-refractory chemical composition of the evolving muzzle exhaust plume fine particles size distribution was characterized during these measurements. A summary of these results and a citation for the task report we presented is given in Appendix A.

The second field campaign for point of impact explosions, however, provided additional experimental data which could be used in test and validating the SCM. Unfortunately, unforeseen delays in being able to conduct the field tests meant that data wasn't available until the last few months of effort for the SCM development and validation work. Consequently, the results presented are based on a preliminary analysis by Battelle of the field data and may change with further analysis.

Table 16 lists three point of impact munitions for which field data from CP-1197 was available for comparison with SCM calculations. The designation, detonation medium, and number of tests are also shown.

Table 16: Munitions tested under CP-1197 [C. Spicer, private communication, 2003]

Item	Designation	Medium	No. per test	No. of tests
155 mm howitzer rounds	M107HE	over steel plate	1	2
4.2 in. mortar	M329A2HE	over soil	1	2
4.2 in mortar	M329A2HE	over steel plate	1	2

Table 16 summarizes the comparison between SCM predictions and measured emissions for the test items in Table 16 listing the ratio of calculated-to-measured emission factors for those species for which field data was available. In contrast to the USAEC exploding ordinance and DPG field test data, SCM over predicts CO₂ relative to measured emission factors by a larger amount considering all three munitions together. It is not clear as to whether or not this is due to difficulties in integrating over the plume in the field tests, differences between reported and actual explosive formulations, or an over prediction of CO₂ in detonation plume by the SCM thermochemical model.

Table 17: SCM Predicted to Measured Emission Factors for CP-1197 Field Test Munitions.

	155-mm howitzer over steel plate	5.2 in mortar Over steel plate	5.2 in mortar over soil
CO ₂	1.3	1.3	1.4
CO	2.2	2.3	2.6
NO _x	0.6	0.5	0.5
Propene	0.7	0.5	0.6
Formaldehyde	0.8	0.6	0.7
Benzene	0.05	0.3	0.05
Toluene	0.01	only upper limit reported	0.01

6.0 Summary

This report has documented the Source Characterization (SCM) model for predicting the release, chemical transformations, deposition, and dispersion of emissions from HE detonation of munitions and explosive charges. The SCM incorporates a number of detailed microphysical processes that are important in understanding munition emission factors and the potential environmental impact. Of particular interest relative to previous models are the sub-models for crater dynamics, afterburning chemistry, and the impact of detonation plume vortex structure of particle deposition. Data analysis and model validation studies to-date have indicated that the SCM model holds much promise as a numerical tool for understanding detonation emissions and supporting environmental impact assessments at DoD test and training sites.

7.0 Acknowledgements

ARI acknowledges SERDP for its financial support and wishes to thank Drs. Robert Holst for his support and guidance. ARI also wishes to thanks Drs. Tom Jenkins, Susan Taylor, Judy Pennington, and Chet Spicer for their efforts in providing field data used in model development and testing.

8.0 References

- Alcala-Jornod, C., H. van den Bergh, M.J. Rossi, Reactivity of NO₂ and H₂O on soot generated in a laboratory: a diffusion tube study at ambient temperature, *Phys. Chem. Chem. Phys.* 2, 5584-5593 (2000)
- Atkinson, R., Kinetics and Mechanisms of the Gas-Phase Reactions of the Hydroxyl Radicals with Organic Compounds, *J. Phys. Chem. Ref. Data*, Monograph No. 1, 1989.
- Atkinson, R, Gas-Phase Tropospheric Chemistry of Organic Compounds, *J. Phys. Chem. Ref. Data*, Monograph No. 2, 1994.
- Atkinson, R. et al., Evaluated Kinetic, Photochemical and Heterogeneous Data for Atmospheric Chemistry: Supplement V., *J. Phys. Chem. Ref. Data* 26, 521 –1011, 1997.
- Baulch, D.L. et al., Evaluated Kinetic Data for Combustion Modeling: Supplement I, *J. Phys. Chem. Ref. Data* 23, 847-1033, 1994.
- Black R.J., Characterization of Open Burning/Open Detonation Emissions, SERDP CP-247, 1998.
- Blais et al. *J. Phys. Chem. A*, 101, 8285-8295, 1997.
- Boughton and DeLaurentis, An Integral Model of Plume Rise from High Explosive Detonations, ASME/AICHE National Heat Transfer Conference, Pittsburg, 1987.
- Carlos-Cuellar, S., P. Li., A.P. Christensen, B.J. Krueger, C. Burrichter, V.H. Grassian, Heterogeneous Uptake Kinetics of Volatile Organic Compounds on Oxide Surfaces Using a Knudsen Cell Reactor: Adsorption of Acetic Acid, Formaldehyde, and Methanol on α -Fe₂O₃, α -Al₂O₃, and SiO₂, *J. Phys. Chem. A* 107, 4250-4261, 2003.
- Carson, John, Chandramouli Sastry, George Lemire, "Sampling Results for AEC Phase IV-A Exploding Ordnance Emission Characterization, Volumes I-IV," Radian International Document No. D0203151MW97, April 2003.
- Choi, W. and M.-T. Leu, Nitric Acid Uptake and Decomposition on Black Carbon (Soot) Surfaces: Its Implications for the Upper Troposphere and Lower Stratosphere, *J. Phys. Chem. A* 102, 7618-1639, 1998.
- Cowperthwaite, M. and W.H. Zwisler, "TIGER Computer Program Documentation", Stanford Research Institute, Publication No. Z106, 1973.
- DeMore, W.B. et al., Chemical Kinetics and Photochemical Data for use in Stratospheric Modeling: Evaluation No. 12, JPL Publication 97-4, NASA Jet Propulsion Laboratory, January 1997.
- Ebersole, J.F., R. Vaglio-Laurin, and D.S. Dvore, "Optical and Fluid Dynamic Properties of Explosion-Produced Dust Clouds", Aerodyne Research, Inc., Billerica, MA, Final Technical Report, Rept. No. ARI-RR-181.1, Sept 1979.
- Ebersole, J.F., R. Vaglio-Laurin, D.S. Dvore, and T. Spaulding, "Scaling Relationships for Dust Obscuration of Electro-optical Systems", Aerodyne Research, Inc., Rept. No. ARI-RR-199, submitted to the Proceedings of the Smoke/Obscurants Symposium IV, April 1980.
- Engelke et al., *J. Phys. Chem. A* 105, 6955-6964, 2001.
- Fried, L.E., CHEETAH 1.39 User's Manual, Lawrence Livermore National Laboratory, UCRL-MA-117541 Rev. 3, 1996.

- Goodman, A.L., P. Li, C.R. Usher, V.H. Grassian, Heterogeneous Uptake of Sulfur Dioxide On Aluminum and Magnesium Oxide Particles, *J. Phys. Chem. A* 105, 6109-6120 (2002)
- Hanisch, F., J.N. Crowley, Heterogeneous Reactivity of Gaseous Nitric Acid on Al_2O_3 , CaCO_3 , and Atmospheric Dust Samples: A Knudsen Cell Study, *J. Phys. Chem. A* 105, 3096-3106 (2001a)
- Hanisch, F., J.N. Crowley, The heterogeneous reactivity of gaseous nitric acid on authentic mineral dust samples, and on mineral and clay mineral components, *Phys. Chem. Chem. Phys.* 3, 2474-2482 (2001b)
- Hanisch, F., J.N. Crowley, Ozone decomposition on Saharan dust: an experimental investigation, *Atmos. Chem. Phys.* 3, 119-130 (2003b)
- Hanisch, F., J.N. Crowley, Heterogeneous reactivity of NO and HNO_3 on mineral dust in the presence of ozone, *Phys. Chem. Chem. Phys.* 5, 883-887 (2003a)
- Hewitt, A.D., T.F. Jenkins, T.A. Ranney, J.A. Stark, M.E. Walsh, S. Taylor, M.R. Walsh, D.J. Lambert, N.M. Perron, N.H. Collins, and R. Karn, "Estimates for Explosives Residue from the Detonation of Army Munitions," US Army Corps of Engineers, Cold Regions Research and Engineering Laboratory, Technical Report ERDC/CRREL TR-03-16, September 2003.
- Jenkins, T.F., T.A. Ranney, P.H. Miyares, N.H. Collins, and A.D. Hewitt, "Use of surface snow sampling to estimate the quantity of explosive residues resulting from land mine detonations," US Army Engineer Research and Development Center, Cold Regions Research and Engineering Laboratory, Hanover NH, TR-00-12, 2000a
- Jenkins, T.F., T.A. Ranney, M.E. Walsh, P.H. Miyares, A.D. Hewitt, and N.H. Collins, "Evaluating the use of snow-covered ranges to estimate explosives residues that result from detonation of Army munitions," US Army Engineer Research and Development Center, Cold Regions Research and Engineering Laboratory, Hanover NH, TR-00-15, 2000b
- Jenkins, T.F., J.C. Pennington, T.A. Ranney, T.E. Berry, P.H. Miyares, M.E. Walsh, A.D. Hewitt, N.M. Perron, L.V. Parker, C.A. Hayes, and E. Wahlgren, "Characterization of explosives contamination at military firing ranges, US Army Engineer Research and Development Center, Cold Regions Research and Engineering Laboratory, Hanover NH, TR-01-5, 2001.
- Jenkins, T.F., M.E. Walsh, P.H. Miyares, A.D. Hewitt, N.H. Collins, and T.A. Ranney, "Use of snow-covered ranges to estimate explosive residues from high-order detonations of Army munitions, *Thermochimica Acta*, Vol 384, 173-185, 2002.
- Johnson M., Development of methodology and techniques for identifying and quantifying products from OB/OD thermal treatment methods – Bang Box Test Series, U.S. Army, AMMCOM, Rock Island, IL 61299-6000, 1992.
- Judeikis, H., A.G. Wren, Laboratory Measurements of NO and NO_2 Depositions onto Soil and Cement Surfaces, *Atmos. Environ.* 12, 2315-2319 (1978)
- Kee, R.J., F.M. Rupley, J.A. Miller, Chemkin-II. A Fortran Chemical Kinetics Package for the Analysis of Gas Phase Chemical Kinetics, Sandia Report, SAND89-8009B, 1992.
- Knowles, C.P. and H.L. Brode, "The theory of cratering phenomena, an overview," pp. 869-895, in Impact and Explosion Cratering, D.J. Roddy, R.O. Pepin, and R.B. Merrill, eds, Pergamon, New York, 1977.
- Li. P., K.A. Perreau, E. Covington, C.H. Song, G.R. Carmichael, V.H. Grassian, Heterogeneous reactions of volatile organic compounds on oxide particles of the most abundant crustal elements: Surface reactions of acetaldehyde, acetone, and propionaldehyde on SiO_2 , Al_2O_3 , Fe_2O_3 , TiO_2 , and CaO , *J. Geophys. Res.* 106, 517-5529 (2001)

Longfellow, C.A., A.R. Ravishankara, D.R. Hanson, Reactive and nonreactive uptake on hydrocarbon soot: HNO_3 , O_3 , and N_2O_5 , J. Geophys. Res. 105, 24,345-24,350 (2000)

Lutz, A.E., R.J. Kee, J.A. Miller, SENKIN: (1991) A Fortran Program for Predicting Homogeneous Gas Phase Chemical Kinetics with Sensitivity Analysis, Sandia Report, SAND87-8248, 1991.

Lakkis I.A., Lagrangian computations of radiating fire plumes, Ph.D. Thesis, Massachusetts Institute of Technology, 2000.

Lamb H. Hydrodynamics, 6th editions, Dover Publications, New York, 1945.

McBride, B.J. and Gordon, S., Computer Program for Calculation of Complex Chemical Equilibrium Compositions with Applications, NASA 1311, June 1996.

Michel, A.E., Usher, C.R., V.H. Grassian, Reactive uptake of ozone on mineral oxides and mineral dusts, Atmos. Environ. 37, 3201-3211 (2003)

Military Environmental Technology Demonstration Center, Detailed Test Plan No. 1 for the Exploding Ordinance Emission Study, Series I, DTC Project No. 1-CO-160-000-246, December 2000.

Military Environmental Technology Demonstration Center, Draft Data Report for Munitions Tested in Detailed Test Plan No. 1, 2001.

Mitchell, W.J. and J. C. Suggs (1998) Emission Factors for the Disposal of Energetic Materials by Open Burning and Open Detonation (OB/OD), USEPA, MD-46, Research Triangle Park, NC 27711, August, 1998.

Mullard, W.G., F. Westley, J.T. Herron, and R.F. Hampson, NIST Chemical Kinetic Database – Version 6.01, NIST Standard Reference Data, Copyright 1994, Gaithersburg, MD 20899, 1994.

Muenter, A., B. G. Koehler, Adsorption of Ammonia on Soot at Low Temperatures, J. Phys. Chem. A 104, 8527-8534 (2000)

Ornellas, D.L., Calorimetric Determinations of the Heat and Products of Detonation for Explosives: October 1961 to April 1982, Lawrence Livermore National Laboratory Report UCRL-52821, 1982.

Pennington, J.C., T.F. Jenkins, J.M. Brannon, J. Lynch, T.A. Ranney, C.H. Hayes, P.H. Miyares, M.E. Walsh, A.D. Hewitt, N.M. Perron, and J.J. Delfino, "Distribution and fate of energetics on DoD test and training ranges: Interim Report 1. U.S. Army Engineer Research and Development Center, Vicksburg, MS, Technical Report ERDC TR-01-13.

Pennington, J.C., T.F. Jenkins, G. Ampleman, S. Thiboutot, J.M. Brannon, J. Lynch, T.A. Ranney, J.A. Stark, M.E. Walsh, J. Lewis, C.H. Hayes, J.E. Mirecki, A.D. Hewitt, N.M. Perron, D.J. Lambert, J. Clausen, and J.J. Delfino, "Distribution and fate of energetics on DoD test and training ranges: Interim Report 2. U.S. Army Engineer Research and Development Center, Vicksburg, MS, Technical Report ERDC TR-02-8.

R.G. Pinnick, G. Fernandez, and B.D. Hinds, "Explosion dust particle size measurements," Appl. Opt. 22 (1), 95-102, 1983.

Roddy, D.J., R.O. Pepin, and R.B. Merrill, eds., Impact and Explosion Cratering, Pergamon, New York, 1977.

Rogaski, C.A., D.M. Golden, L.R. Williams, Reactive uptake and hydration experiments on amorphous carbon treated with NO_2 , SO_2 , O_3 , HNO_3 and H_2SO_4 , Geophys. Res. Lett. 24, 381-384 (1997)

Sander, S.P., R.R. Friedl, D.M. Golden, M.J. Kurylo, R.E. Huie, V.L. Orkin, G.K. Moortgat, A.R. Ravishankara, C.E. Kolb, M.J. Molina, B.J. Finlayson-Pitts, Chemical Kinetics and Photochemical Data for Use In Atmospheric Studies, Evaluation No. 14, Jet Propulsion Laboratory, Report No. JPL Publication No. 02-25 (January 2003)

Scire, J.S., Strimaitis, D.G., Yamartino, R.J., A User's Guide for the CALPUFF Dispersion Model, Earth Tech, Inc., 2000.

Sehmel G.A., Deposition and resuspension, Chapter 12 in Atmospheric Science and Power Production, DOE/TIC-27601, DE84005177, NTIC, USDOC, Springfield, VA 22161, pp. 533-583, 1984.

Seinfeld, J.H. and S.N. Pandis, Atmospheric Chemistry and Physics, From Air Pollution to Climate Change, John Wiley & Sons, Inc., New York, NY, 1998.

Slinn W.G.N., Precipitation Scavenging, Chapter 11 in Atmospheric Science and Power Production, DOE/TIC-27601, DE84005177, NTIC, USDOC, Springfield, VA 22161, pp. 466-532, 1984.

Stadler, D. and M.J. Rossi, The reactivity of NO₂ and HONO on flame soot at ambient temperature: The influence of combustion conditions, Phys. Chem, Chem, Phys. 2, 5420-5429 (2000)

Stephens, S., M.J. Rossi, D.M. Golden, The heterogeneous reaction of ozone on carbonaceous surfaces, Int. J. Chem. Kinet. 18, 1133-1149 (1986).

Taylor, S., A.D. Hewitt, C. Hayes, L. Perovich, J. Level, P.G. Thorne, and C. Daghljan, "TNT particles from detonated 155-mm howitzer rounds," to be submitted to Chemosphere, 2004.

Thiboutot, S., G. Ampleman, A. Gagnon, A. Marois, T.F. Jenkins, M.E. Walsh, P.G. Torne, and T.A. Ranney, "Characterization of antitank firing ranges at CFB Valartier, WATC Wainwright and CFAD Dundurn, DERV-R-9809, Defence Research Establishment, Valcartier, Quebec, October, 1998.

Tsang, W. and J.T. Herron, Chemical Kinetic Data Base for Propellant Combustion, J. Phys. Chem. Ref. Data 20, 609-663, 1991.

Ullerstam, M, R. Vogt, S. Langer, E.J. Ljungström, The kinetics and mechanism of SO₂ oxidation by O₃ on mineral dust, Phys. Chem, Chem, Phys. 4, 4694-4669 (2002)

Ullerstam, M., M.S. Johnson, R. Vogt, E.J. Ljungström, DRIFTS and Knudsen cell study of the heterogeneous activity of SO₂ and NO₂ on mineral dust, Atmos. Chem. Phys. 3, 2043-2051 (2003)

Underwood, G.M., C.H. Song, M. Phadnis, G.R. Carmichael, V.H. Grassian. Heterogeneous reactions of NO₂ and HNO₃ on oxides and mineral dust: A combined laboratory and modeling study, J. Geophys. Res. 106, 18,055-15,066 (2001a)

Underwood, G.M., P. Li, H. Al-Abadleh, V.H. Grassian, A Knudsen Cell Study of the Heterogeneous Reactivity of Nitric Acid on Oxide and Mineral Dust Particles, J. Phys. Chem. A. 105, 6609-6620 (2001b)

USACHPPM, "Training range site characterization and risk screening, Camp Shelby, MS, Geohydrologic Study No. 38-EH-8879-99, Aberdeen Proving Ground, MD, 2000.

U.S. Army Engineering , "Cratering from High Explosive Charges: Analysis of crater Data," Tech. Report, No. 2-547, Report 2, U.S. Army Engineer Waterways Experimental Station, Vicksburg, MS, June 1961.

Usher, C.R., H. Al-Hosney, S. Carlos-Cuellar, V.H., Grassian, A laboratory study of the heterogeneous uptake and oxidation of sulfur dioxide on mineral dust particles, J. Geophys. Res. 107, D23, 4713, doi:10.1029/2002JD002051 (2002)

Usher, C.R., A.E. Michel, V.H. Grassian, Reactions on Mineral Dust, Chem. Rev. 103, 4883-4939 (2003a)

Usher, C.R., A.E. Michel, D. Dtec, V.H. Grassian, Laboratory studies of ozone uptake on processed mineral dust, Atmos. Environ. 37, 5337-5347 (2003b).

Velsko, C.A., B.E. Watkins, C.O. Pruneda, J.R. Stephens, and J. Lipkin, Emissions Characterization in the Contained Underground Demilitarization Laboratory at the Nevada Test Site, UCRL-JC-126887, 1999.

Wisbith, A.S. and D.W. Joseph, Battelle Memorial Institute, Munitions Modeling Review, Final Report, Contract No. SP0700-00-D-3180, for Commander, U.S. Army Environmental Center, September 2001.

Yinon, J. and S. Zitrin, *Modern Methods and Applications in Analysis of Explosives*, West Sussex, England, John Wiley and Sons, LTD.

Zhang, X., Moussa, N. A., Groszmann, D. E., Beach, A. B., and Noland R.B. A simple analytical buoyant puff rise model, CPIA Publication 634, JANNAF Propulsion and Subcommittee Joint Meeting, 4-8 December, Tampa, FL, 1995.

Zhang X. J. and Ghoniem, A.F., A computational model for the rise and dispersion of wind-blown, buoyancy-driven plumes-I. Neutrally stratified atmosphere. Atmos. Environ., Vol. 27A, 2295-2311, 1993.

Zhang, X., Moussa, N. A., Groszmann, D.E., and Masonjones, M. C., Application of ADORA to dispersion modeling of instantaneously released reacting chemicals. Presented in the Sixth Topical Meeting on Emergency Preparedness and Response, American Nuclear Society, San Francisco, April 22-25, 1997.

9.0 Appendix A - Aerosol Mass Spectrometric Point-of-Fire Measurements

Aerosol Mass Spectrometer Characterization of Point-of-Discharge Fine Particle Emissions

Added Task Summary for Project CP-1159

T. B. Onasch, H. Boudries, D. R. Worsnop and C. E. Kolb
Center for Aerosol and Cloud Chemistry
Aerodyne Research, Inc
45 Manning Road
Billerica, MA 01821

August 2003

An Aerodyne Aerosol Mass Spectrometer (AMS) was used to measure the fine particulate mass (PM_{1.0}) emitted from point-of-discharge emission plumes in the Aberdeen Test Center (ATC) enclosed gun discharge test facility from September 25 to October 2, 2002. The AMS provided real-time measurements of the size-resolved mass distributions for fine particles between 40 and 1000 nm in diameter and the total mass loadings of organic and non-refractory inorganic species (PM_{1.0}). These tests were carried out as part of the SERDP project CP-1197, led by Battelle Columbus (C. Spicer, PI), in coordination with the Army Environmental Center and the Aberdeen Test Center.

Fine particulate emissions from the muzzle of weapons firing five different munitions were measured. After the firing of each shell, the emissions were isolated in a steel test chamber for approximately 20 minutes for sampling. For each munitions type beyond the first, an initial background was established within the chamber and then two shots were fired, one in the morning and one in the afternoon. Three replicates of the first munitions type were fired. The initial particulate mass loadings for each shot were very high, ranging from 1000 to 18000 $\mu\text{g m}^{-3}$. Figure 1 shows the total fine particulate mass loadings for each test. According to the Munitions Items Disposition Action System (MIDAS) database the chemical compositions of the munitions vary; however, the majority of the propellant mass is nitrocellulose and other nitrogen-rich organic compounds. The munitions' casings and projectiles are composed mainly of aluminum, zinc, steel, nickel, and copper alloys. As expected, the discharge particulate emissions measured during this study were dominated by the propellant materials, although for several munitions there was apparently measurable particulate mass from ablated metal alloy.

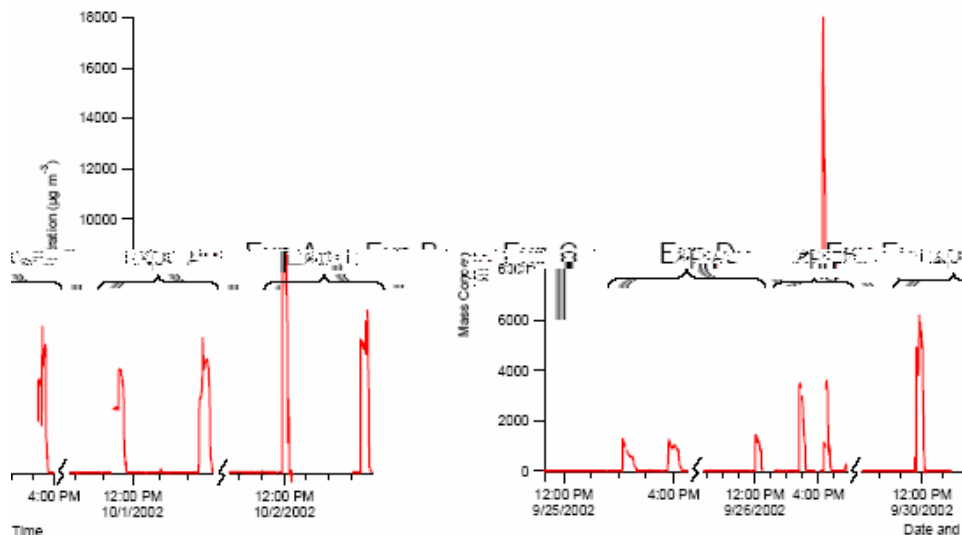


Figure 1. The total fine particulate mass loadings as measured by the AMS for each individual point-of-discharge test.

The main volatile and semi-volatile particulate components quantified by the AMS included inorganic sulfates, nitrates, carbonates, chlorides and the total organic particulate mass. Specific air toxic compounds identified and quantified by the AMS include particle-bound cyanides, polycyclic aromatic hydrocarbons, and several heavy metals. The AMS oven temperature was varied to help identify and distinguish between non-refractory and refractory compounds. The AMS flash vaporizes particulate matter from a heated oven during detection. Nominal oven temperature for non-refractory inorganic and organic compounds is 600°C. At oven temperatures up to 1000°C, more refractory compounds, such as the sulfates and chlorides of zinc, lead, and antimony, vaporize more readily and are thus easier to detect and identify.

The fine particle emissions were consistently internally mixed particles that coagulated and dry deposited with time. Particulate mass and chemical composition results show a strong dependence on the extent of propellant combustion. Ample evidence exists indicating that several different exhaust plumes underwent further oxidation, during an afterburning event. This conclusion is supported by gas phase CO and CO₂ data. Fine particulate emission factors (µg PM/g propellant) are reported in Table 1. A full report presenting the data and detailed analysis has been prepared and distributed [Onasch *et al.*, 2003].

	Munitions				
	M793 (Exp A)	M910 (Exp B)	M931 (Exp C)	M934 (Exp D)	M931 (Z4) (Exp E)
Ammonium	4	5	39	16	
Nitrate	195	62	237	127	27
Sulfate	68	225	278	2471	115
Chloride	4	4	298	11	7
Organics	225	145	2160	811	978
Carbonates	293	87	905	322	629
Cyanide	45	8	144	80	126
PAH	0	0	3	1	1
Zinc	90	1234	1131	0	1
Lead	15	60	12	6	3
Antimony	5	23	0	1	0
Total PM	976	2032	5554	4202	2899

Table 1 – Fine particulate emission factors for each munitions type (µg PM/g propellant).

Onasch, T.B., H. Boudries, D.R. Worsnop, and C.E. Kolb, *Aerosol Mass Spectrometer Characterization of Point-of-Discharge Fine Particulate Emissions*, ARI-RR-1382, Aerodyne Research, Inc., Billerica, 2003.

10.0 Appendix B: Chemical Kinetic Mechanism

			ELEMENTS CONSIDERED	ATOMIC WEIGHT					

			1. H	1.00797					
			2. C	12.0112					
			3. O	15.9994					
			4. N	14.0067					

			C						
			P H						
			H A						
			A R						
SPECIES	S	G	MOLECULAR	TEMPERATURE		ELEMENT COUNT			
CONSIDERED	E	E	WEIGHT	LOW	HIGH	H	C	O	N

1. C(S)	S	0	12.01115	300.0	5000.0	0	1	0	0
2. H2	G	0	2.01594	300.0	5000.0	2	0	0	0
3. O2	G	0	31.99880	300.0	5000.0	0	0	2	0
4. H2O	G	0	18.01534	300.0	5000.0	2	0	1	0
5. O	G	0	15.99940	300.0	5000.0	0	0	1	0
6. H	G	0	1.00797	300.0	5000.0	1	0	0	0
7. OH	G	0	17.00737	300.0	5000.0	1	0	1	0
8. HO2	G	0	33.00677	200.0	3500.0	1	0	2	0
9. H2O2	G	0	34.01474	300.0	5000.0	2	0	2	0
10. CH2O	G	0	30.02649	300.0	5000.0	2	1	1	0
11. HCO	G	0	29.01852	300.0	5000.0	1	1	1	0
12. CO	G	0	28.01055	300.0	5000.0	0	1	1	0
13. CO2	G	0	44.00995	300.0	5000.0	0	1	2	0
14. N	G	0	14.00670	200.0	6000.0	0	0	0	1
15. N2	G	0	28.01340	300.0	5000.0	0	0	0	2
16. NO	G	0	30.00610	200.0	6000.0	0	0	1	1
17. NO2	G	0	46.00550	200.0	6000.0	0	0	2	1
18. HNO	G	0	31.01407	200.0	6000.0	1	0	1	1
19. HONO	G	0	47.01347	300.0	5000.0	1	0	2	1
20. N2O	G	0	44.01280	200.0	6000.0	0	0	1	2
21. NO3	G	0	62.00490	300.0	5000.0	0	0	3	1
22. HNO3	G	0	63.01287	300.0	5000.0	1	0	3	1
23. CH4	G	0	16.04303	300.0	5000.0	4	1	0	0
24. CH3	G	0	15.03506	300.0	5000.0	3	1	0	0
25. CH3O	G	0	31.03446	300.0	3000.0	3	1	1	0
26. CH2	G	0	14.02709	300.0	5000.0	2	1	0	0
27. CH	G	0	13.01912	300.0	5000.0	1	1	0	0
28. CH2OH	G	0	31.03446	250.0	4000.0	3	1	1	0
29. CH3OH	G	0	32.04243	300.0	5000.0	4	1	1	0
30. C2H6	G	0	30.07012	300.0	1500.0	6	2	0	0
31. C2H5	G	0	29.06215	300.0	5000.0	5	2	0	0
32. C2H4	G	0	28.05418	300.0	5000.0	4	2	0	0
33. C2H3	G	0	27.04621	300.0	5000.0	3	2	0	0

34.	C2H2	G	0	26.03824	300.0	5000.0	2	2	0	0
35.	C2H	G	0	25.03027	300.0	5000.0	1	2	0	0
36.	CH2CO	G	0	42.03764	200.0	3500.0	2	2	1	0
37.	CH3CO	G	0	43.04561	300.0	5000.0	3	2	1	0
38.	CH3HCO	G	0	44.05358	300.0	5000.0	4	2	1	0
39.	CN	G	0	26.01785	300.0	5000.0	0	1	0	1
40.	HCN	G	0	27.02582	300.0	5000.0	1	1	0	1
41.	HNCO	G	0	43.02522	300.0	5000.0	1	1	1	1
42.	NH	G	0	15.01467	300.0	5000.0	1	0	0	1
43.	NH2	G	0	16.02264	300.0	5000.0	2	0	0	1
44.	NH3	G	0	17.03061	300.0	5000.0	3	0	0	1

REACTIONS CONSIDERED				(k = A T**b exp(-E/RT))		
				A	b	E
1.	H2+M=H+H+M			4.57E+19	-1.4	104000.0
	H2	Enhanced by	2.500E+00			
	H2O	Enhanced by	1.200E+01			
	CO	Enhanced by	1.900E+00			
	CO2	Enhanced by	3.800E+00			
2.	O+H2O=OH+OH			2.97E+06	2.0	13400.0
3.	O+H2=H+OH			5.06E+04	2.7	6290.0
4.	O+O+M=O2+M			6.17E+15	-1.5	.0
	H2	Enhanced by	2.500E+00			
	H2O	Enhanced by	1.200E+01			
	CO	Enhanced by	1.900E+00			
	CO2	Enhanced by	3.800E+00			
5.	H+O2=O+OH			1.94E+14	.0	16440.0
6.	H+O2 (+M)=HO2 (+M)			4.52E+13	.0	.0
	Low pressure limit:	.67000E+20	-.14200E+01	.00000E+00		
	TROE centering:	.10000E+01	.10000E-89	.10000E+91		
	H2	Enhanced by	2.500E+00			
	H2O	Enhanced by	1.200E+01			
	CO	Enhanced by	1.900E+00			
	CO2	Enhanced by	3.800E+00			
7.	H+O+M=OH+M			4.72E+18	-1.0	.0
	H2	Enhanced by	2.500E+00			
	H2O	Enhanced by	1.200E+01			
	CO	Enhanced by	1.900E+00			
	CO2	Enhanced by	3.800E+00			
8.	OH+H2=H2O+H			2.16E+08	1.5	3430.0
9.	OH+H+M=H2O+M			2.21E+22	-2.0	.0
	H2	Enhanced by	2.500E+00			
	H2O	Enhanced by	1.200E+01			
	CO	Enhanced by	1.900E+00			
	CO2	Enhanced by	3.800E+00			
10.	HO2+O=O2+OH			1.75E+13	.0	-397.0
11.	HO2+H=H2+O2			6.62E+13	.0	2130.0
12.	HO2+H=OH+OH			1.69E+14	.0	874.0
13.	HO2+OH=H2O+O2			1.90E+16	-1.0	.0
14.	HO2+HO2=H2O2+O2			4.20E+14	.0	11980.0
	Declared duplicate reaction...					
15.	HO2+HO2=H2O2+O2			1.30E+11	.0	-1629.0
	Declared duplicate reaction...					

16.	H2O2 (+M)=OH+OH (+M)		2.95E+14	.0	48460.0
	Low pressure limit:	.12000E+18	.00000E+00	.45500E+05	
	TROE centering:	.50000E+00	.10000E-89	.10000E+91	
17.	H2O2+O=OH+HO2		9.64E+06	2.0	3970.0
18.	H2O2+H=H2O+OH		1.00E+13	.0	3590.0
19.	H2O2+H=HO2+H2		4.82E+13	.0	7950.0
20.	H2O2+OH=H2O+HO2		1.00E+12	.0	.0
	Declared duplicate reaction...				
21.	H2O2+OH=H2O+HO2		5.80E+14	.0	9557.0
	Declared duplicate reaction...				
22.	CH2O+M=HCO+H+M		1.63E+33	-4.1	92550.0
23.	CH2O+M=H2+CO+M		8.25E+15	.0	69540.0
24.	CH2O+O2=HCO+HO2		2.05E+13	.0	38920.0
25.	CH2O+O=HCO+OH		1.81E+13	.0	3078.0
26.	CH2O+H=HCO+H2		1.26E+08	1.6	2163.0
27.	CH2O+OH=HCO+H2O		3.43E+09	1.2	-447.0
28.	CH2O+HO2=HCO+H2O2		1.99E+12	.0	11660.0
29.	HCO+M=H+CO+M		1.85E+17	-1.0	17000.0
	H2	Enhanced by	1.890E+00		
	H2O	Enhanced by	1.200E+01		
	CO	Enhanced by	1.900E+00		
	CO2	Enhanced by	3.800E+00		
30.	HCO+O2=CO+HO2		7.58E+12	.0	406.0
31.	HCO+O=CO+OH		3.00E+13	.0	.0
32.	HCO+O=CO2+H		3.00E+13	.0	.0
33.	HCO+H=CO+H2		7.23E+13	.0	.0
34.	HCO+OH=CO+H2O		3.00E+13	.0	.0
35.	HCO+HO2=CO2+OH+H		3.00E+13	.0	.0
36.	CO+O (+M)=CO2 (+M)		1.80E+10	.0	2380.0
	Low pressure limit:	.13500E+25	-.27880E+01	.41910E+04	
	TROE centering:	.10000E+01	.10000E-89	.10000E+91	
	N2	Enhanced by	1.330E+00		
	H2	Enhanced by	2.500E+00		
	H2O	Enhanced by	1.200E+01		
	CO	Enhanced by	1.900E+00		
	CO2	Enhanced by	3.800E+00		
37.	CO+O2=CO2+O		2.53E+12	.0	47700.0
38.	CO+OH=CO2+H		1.50E+07	1.3	-765.0
39.	CO+HO2=CO2+OH		5.80E+13	.0	22930.0
40.	N+O2=NO+O		6.40E+09	1.0	6280.0
41.	N+OH=NO+H		3.80E+13	.0	.0
42.	N+HO2=NO+OH		1.00E+13	.0	2000.0
43.	N+CO2=NO+CO		1.90E+11	.0	3400.0
44.	N+NO=N2+O		3.27E+12	.3	.0
45.	N+NO2=NO+NO		4.00E+12	.0	.0
46.	N+NO2=N2O+O		5.00E+12	.0	.0
47.	N+NO2=N2+O2		1.00E+12	.0	.0
48.	N+HNO=N2O+H		5.00E+10	.5	3000.0
49.	N+N2O=N2+NO		1.00E+13	.0	19870.0
50.	NO+M=N+O+M		9.64E+14	.0	148400.0
	N2	Enhanced by	1.500E+00		
	CO2	Enhanced by	2.500E+00		
51.	NO+O (+M)=NO2 (+M)		1.30E+15	-.8	.0
	Low pressure limit:	.47200E+25	-.28700E+01	.15510E+04	
	TROE centering:	.95700E+00	.10000E-89	.83320E+04	
52.	NO+H (+M)=HNO (+M)		1.52E+15	-.4	.0
	Low pressure limit:	.89600E+20	-.13200E+01	.73520E+03	

	TROE centering:	.82000E+00	.10000E-89	.10000E+91	
53.	NO+OH (+M)=HONO (+M)		1.99E+12	-.1	-721.0
	Low pressure limit:	.50800E+24	-.25100E+01	-.67560E+02	
	TROE centering:	.62000E+00	.10000E-89	.10000E+91	
	H2O	Enhanced by	5.000E+00		
54.	NO+HO2=NO2+OH		2.11E+12	.0	-479.0
55.	NO+HCO=HNO+CO		7.23E+12	.0	.0
56.	NO2+O=O2+NO		3.91E+12	.0	-238.0
57.	NO2+O (+M)=NO3 (+M)		1.33E+13	.0	.0
	Low pressure limit:	.14900E+29	-.40800E+01	.24670E+04	
	TROE centering:	.82600E+00	.10000E-89	.31910E+04	
58.	NO2+H=NO+OH		1.32E+14	.0	361.6
59.	NO2+OH (+M)=HNO3 (+M)		2.41E+13	.0	.0
	Low pressure limit:	.64200E+33	-.54900E+01	.23500E+04	
	TROE centering:	.83700E+00	.10000E-89	.16570E+04	
60.	NO2+CH2O=HONO+HCO		8.02E+02	2.8	13730.0
61.	NO2+HCO=CO+HONO		1.24E+23	-3.3	2354.0
62.	NO2+HCO=H+CO2+NO		8.39E+15	-.8	1927.0
63.	NO2+CO=CO2+NO		9.03E+13	.0	33780.0
64.	NO2+NO2=NO3+NO		9.64E+09	.7	20920.0
65.	NO2+NO2=2NO+O2		1.63E+12	.0	26120.0
66.	HNO+O2=NO+HO2		1.00E+13	.0	25000.0
67.	HNO+O=OH+NO		1.81E+13	.0	.0
68.	HNO+H=H2+NO		1.81E+13	.0	993.5
69.	HNO+OH=H2O+NO		1.00E+13	.0	993.5
70.	HNO+HCO=CH2O+NO		6.02E+11	.0	1987.0
71.	HNO+NO=N2O+OH		2.00E+12	.0	26000.0
72.	HNO+NO2=HONO+NO		6.02E+11	.0	1987.0
73.	HNO+HNO=H2O+N2O		8.51E+08	.0	3080.0
74.	HONO+O=OH+NO2		1.20E+13	.0	5961.0
75.	HONO+H=H2+NO2		1.20E+13	.0	7352.0
76.	HONO+OH=H2O+NO2		1.26E+10	1.0	135.1
77.	N2O (+M)=N2+O (+M)		7.91E+10	.0	56020.0
	Low pressure limit:	.91300E+15	.00000E+00	.57690E+05	
	H2O	Enhanced by	7.500E+00		
	NO	Enhanced by	2.000E+00		
	CO	Enhanced by	2.000E+00		
	CO2	Enhanced by	3.000E+00		
78.	N2O+O=O2+N2		1.00E+14	.0	28000.0
79.	N2O+O=2NO		1.00E+14	.0	28000.0
80.	N2O+H=N2+OH		2.53E+10	.0	4550.0
	Declared duplicate reaction...				
81.	N2O+H=N2+OH		2.23E+14	.0	16750.0
	Declared duplicate reaction...				
82.	N2O+OH=HO2+N2		2.00E+12	.0	40000.0
83.	N2O+CO=N2+CO2		5.01E+13	.0	44000.0
84.	CH4+O2=CH3+HO2		3.97E+13	.0	56687.4
85.	CH4+H=CH3+H2		1.32E+04	3.0	8009.1
86.	CH4+O=CH3+OH		7.22E+08	1.6	8454.6
87.	CH4+OH=CH3+H2O		1.57E+07	1.8	2772.0
88.	CH4+HO2=CH3+H2O2		9.03E+12	.0	24631.2
89.	CH3+M=CH2+H+M		1.02E+16	.0	90288.0
90.	CH3+O2=CH3O+O		1.32E+14	.0	31284.0
91.	CH4 (+M)=CH3+H (+M)		2.40E+16	.0	104544.0
	Low pressure limit:	.47000E+48	-.82000E+01	.11722E+06	
	TROE centering:	.69000E+00	.90000E+02	.22100E+04	
92.	CH3+H=CH2+H2		6.02E+13	.0	15048.0

93.	CH3+O=CH2O+H	8.43E+13	.0	.0
94.	CH3+OH=CH2+H2O	7.22E+12	.0	2772.0
95.	CH3+HO2=CH3O+OH	1.81E+13	.0	.0
96.	CH3O+H=CH2O+H2	1.81E+13	.0	.0
97.	CH2+O2=CO2+H+H	1.60E+12	.0	1000.0
98.	CH2+O2=CH2O+O	5.00E+13	.0	9000.0
99.	CH2+O2=CO2+H2	6.90E+11	.0	500.0
100.	CH2+O2=CO+H2O	1.90E+10	.0	-1000.0
101.	CH2+O2=CO+OH+H	8.60E+10	.0	-500.0
102.	CH2+O2=HCO+OH	4.30E+10	.0	-500.0
103.	CH2+H=CH+H2	3.01E+13	.0	.0
104.	CH2+O=CO+H+H	1.51E+13	.0	.0
105.	CH2+O=CO+H2	1.51E+13	.0	.0
106.	CH2+OH=CH2O+H	3.01E+13	.0	.0
107.	CH2+HCO=CH3+CO	1.81E+13	.0	.0
108.	CH+O=CO+H	3.97E+13	.0	.0
109.	CH3+CH3 (+M)=C2H6 (+M)	3.61E+13	.0	.0
	Low pressure limit:	.12700E+42	-.70000E+01	.27522E+04
	TROE centering:	.62000E+00	.73000E+02	.11800E+04
110.	C2H6+O2=C2H5+HO2	6.02E+13	.0	51678.0
111.	C2H6+O=C2H5+OH	9.99E+08	1.5	5781.6
112.	C2H6+OH=C2H5+H2O	7.22E+06	2.0	861.3
113.	C2H6+HO2=C2H5+H2O2	1.32E+13	.0	20395.0
114.	C2H6+CH3=C2H5+CH4	1.51E-07	6.0	6025.1
115.	C2H5+H2=C2H6+H	3.07E+00	3.6	8415.0
116.	C2H5+O2=C2H4+HO2	1.02E+10	.0	-2178.0
117.	C2H5+O=CH2O+CH3	1.13E+13	.0	.0
118.	C2H5+H=CH3+CH3	3.61E+13	.0	.0
119.	C2H5+CH3=CH4+C2H4	1.14E+12	.0	.0
120.	C2H5+C2H5=C2H4+C2H6	1.44E+12	.0	.0
121.	C2H4+M=C2H3+H+M	2.59E+17	.0	96228.0
122.	C2H4+M=C2H2+H2+M	3.49E+16	.0	71280.0
123.	C2H4+O=CH3+HCO	4.74E+06	1.9	178.2
124.	C2H4+O=CH2+CH2O	8.13E+06	1.9	178.2
125.	C2H4+O=CH2CO+H2	6.77E+05	1.9	178.2
126.	C2H4+H=C2H3+H2	5.42E+14	.0	14850.0
127.	C2H4+OH=C2H3+H2O	2.05E+13	.0	5920.2
128.	C2H4+CH3=C2H3+CH4	4.15E+12	.0	11088.0
129.	C2H3+O=C2H2+OH	1.00E+13	.0	.0
130.	C2H3+O=CH3+CO	1.00E+13	.0	.0
131.	C2H3+O=CH2+HCO	1.00E+13	.0	.0
132.	C2H3+H=C2H2+H2	1.20E+13	.0	.0
133.	C2H2+OH=C2H+H2O	3.01E+13	.0	12870.0
134.	C2H2+OH=CH2CO+H	3.01E+13	.0	12870.0
135.	C2H+O=CH+CO	1.02E+13	.0	.0
136.	C2H+H2=C2H2+H	1.08E+13	.0	2158.2
137.	CH2CO+H=CH3+CO	1.81E+13	.0	3366.0
138.	CH2CO+OH=CH2O+HCO	1.02E+13	.0	.0
139.	NH2+O2=HNO+OH	1.78E+12	.0	14900.0
140.	NH2+O=HNO+H	6.63E+14	-.5	.0
141.	NH2+O=NH+OH	6.75E+12	.0	.0
142.	NH2+H=NH+H2	6.92E+13	.0	3650.0
143.	NH2+OH=NH+H2O	4.00E+06	2.0	1000.0
144.	NH2+N=N2+2H	7.20E+13	.0	.0
145.	NH2+NO=N2+H2O	1.30E+16	-1.3	.0
	Declared duplicate reaction...			
146.	NH2+NO=N2+H2O	*****	-.6	.0

```

Declared duplicate reaction...
147. NH2+NO=N2O+H2          5.00E+13      .0      24640.0
148. NH2+NO=HNO+NH          1.00E+13      .0      40000.0
149. NH2+NO2=N2O+H2O        3.28E+18     -2.2        .0
150. NH3+M=NH2+H+M          2.20E+16      .0     93470.0
151. NH3+O=NH2+OH           9.40E+06      1.9      6460.0
152. NH3+H=NH2+H2           6.40E+05      2.4     10170.0
153. NH3+OH=NH2+H2O         2.04E+06      2.0       566.0
154. NH3+HO2=NH2+H2O2       3.00E+11      .0     22000.0
155. NH2+HO2=NH3+O2         1.00E+13      .0        .0
156. NH2+NH2=NH3+NH         5.00E+13      .0     10000.0
157. HCN(+M)=H+CN(+M)       8.30E+17     -0.9    123800.0
      Low pressure limit:    .35700E+27  -.26000E+01  .12490E+06
      TROE centering:       .95700E+00  .10000E-89  .83320E+04
158. HCN+O=CN+OH            2.70E+09      1.6     29200.0
159. HCN+H=H2+CN            3.73E+14      .0     24850.0
160. HCN+OH=H2O+CN          3.90E+06      1.8     10290.0
161. HCN+OH=NH2+CO           7.83E-04      4.0      4000.0
162. HCN+HCO=CH2O+CN        2.41E+12      .0     34180.0
NOTE:  A units mole-cm-sec-K, E units cal/mole

```